

DESIGN AND DEVELOPMENT OF CHALCOGENIDE BASED SUPERSTRATE THIN FILM SOLAR CELLS

Thesis

Submitted in partial fulfillment of the requirements for the degree of
DOCTOR OF PHILOSOPHY

by

S. Varadharajaperumal

Under the Guidance of

Dr. M.N. Satynarayan
Professor

Dept. of Physics
NITK Surathkal- 575025

Dr. GopalKrishna Hegde
Professor

Dept. of BioSystems Science and Engineering
IISc, Bengaluru- 560012



DEPARTMENT OF PHYSICS,
NATIONAL INSTITUTE OF TECHNOLOGY KARNATAKA,
SURATHKAL, MANGALORE - 575025

August, 2020

DECLARATION

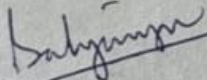
I hereby *declare* that the Research Thesis entitled **DESIGN AND DEVELOPMENT OF CHALCOGENIDE BASED SUPERSTRATE THIN FILM SOLAR CELLS** which is being submitted to the *National Institute of Technology Karnataka, Surathkal* in partial fulfillment of the requirement for the award of the Degree of *Doctor of Philosophy in Physics* is a *bonafide report of the research work carried out by me*. The material contained in this Research Thesis has not been submitted to any University or Institution for the award of any degree.

S. Varadharaajaperumal
08/08/2020


S. VARADHARAJAPERUMAL
Reg. No. 14501SPH14P02.
Department of Physics.

Place: NITK, Surathkal.

Date: 08-08-2020



Dr. M.N. Satyanarayan
Research Supervisor, NITK



Dr. Gopalakrishna Hegde,
Co-Supervisor
Dept of BSSE, IISc Bangalore



Dr. Ajith K.M.
HOD, Physics Dept NITK
Chairman, DRPC

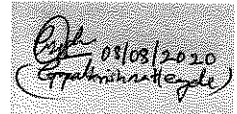
ASSOCIATE PROFESSOR & HEAD
Physics Department
NITK Surathkal, Mangalore-575025
KARNATAKA

CERTIFICATE

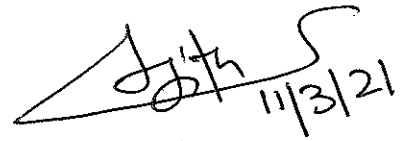
This is to certify that the Research Thesis entitled **DESIGN AND DEVELOPMENT OF CHALCOGENIDE BASED SUPERSTRATE THIN FILM SOLAR CELLS** submitted by **S. Varadharajaperumal** (Register Number: 145015PH14P02) as the record of the research work carried out by him, is accepted as the *Research Thesis submission* in partial fulfillment of the requirements for the award of degree of **Doctor of Philosophy**.


8/3/21

Prof. M.N. Satyanarayan
Research Supervisor
Professor
Dept. of Physics.
NITK, Surathkal


08/08/2020
(Gopalkrishna Hegde)

Prof. Gopalkrishna Hegde
Research Supervisor
Professor
Dept. of BioSystems Science and Engineering
IISc, Bengaluru


11/3/21

Chairman-DRPC
(Signature with Date and Seal)

ASSOCIATE PROFESSOR & HEAD
Physics Department
NITK Surathkal, Mangalore-575025
KARNATAKA

Dedicated to my Parents

ஈன்ற பொழுதின் பெரிதுவக்கும் தன்மகனைச்
சான்றோன் எனக்கேட்ட தாய்.

The mother who hears her son called "a wise man" will rejoice more than she did at his birth.

மகன் தந்தைக்கு ஆற்றும் உதவி இவன்தந்தை
என்றோற்றான் கொள்ளும் சொல்.

(So to act) that it may be said "by what great penance did his father beget him," is the benefit which a son should render to his father.

Acknowledgements

This thesis would not have been possible without the support, time, encouragement and dedication of many distinctive people who were the supremacy behind me.

I would first like to thank my research supervisors Professor Dr. M.N. Satyanarayan and Professor Dr. Gopalkrishna Hegde for their boundless support, exemplary guidance and encouragement. I remember with gratitude of their valuable suggestions and criticisms during my research.

I would like to thank my doctoral committee members Professor Dr. Shashikala and Professor Dr. Aswini Chaturvedi for accommodating me irrespective of their busy schedules and providing the scholastic remarks on my research work.

I also express my sincere gratitude to Dr. R. Ganesan, Principle Research Scientist, Department of Physics, IISc., who provided the lab and instruments facilities to carry out my research work. The thesis could not complete without his genuine support and assistance.

I am grateful to thank Professor Dr. Srinivasa Raghavan, CeNSE, IISc., and Dr. Girish Gunte who encouraged me to register PhD at NITK.

I would also like to thank my research colleagues Mr. Nimith, Mr. Achyutha, Mr. Karthik Hegde at NITK and my CeNSE Colleagues Dr. Vijay Mishra, Mr. Pradeep Kumar, Mr. Prahlada, Ms. Suma, Ms. Martina, Mr. Ramshankar, Mr. Venu and Dr. Arun Babu for their kindness and support to fulfil my doctorate study.

I extend my sincere thanks to Dr. Sripan and Dr. Alagarasan for their endless support helps me a lot to carry out my research work at IISc.

Finally, but by no means least, I express my deep sense of love to God Almighty (my father late B. Selvaraj) and my family members.

I am greatly indebted to my mother S. Ramani, my wife V. Chithra, my kids V. Esswanth and V. Mohitha for their patience and immense help at all levels with moral support during my Ph.D. I also thank my sisters M. Vijayalakshmi, V. Vaijeyanthi, brothers in law G. Mohanasundaram, T. Vishwanathan and nephews V. Palanisamy, V. Sasirekha who have prayed for me and supported me spiritually and mentally without which this research would not have been possible.

Abstract

Thin film solar cells (substrate and superstrate) are promising approaches for various photovoltaic applications, which offer a wide variety of choices in terms of device design and fabrication. At the same time, for modern research development a novel, exotic, innovative and modest materials with simple manufacturing processes need to be pursued in a focussed manner. Present thesis work explores the design and development of superstrate type binary (CdTe) and quaternary (CZTS) thin film solar cells and their photovoltaic performance. Also, this thesis mainly focuses on the effect of combining two-hole transport layers in superstrate CdS/CdTe solar cells and the nanostructured (1D & 3D) metal oxides (ZnO and TiO₂) as window or electron transporting layers (along with or without CdS (buffer) layer) in stoichiometry adjusted superstrate CZTS thin film solar cells. Before the fabrication of photovoltaic devices, the structural, morphological, optical and electrical properties of deposited photoanodes, absorbing layers and transporting (electron and hole) layers, using different techniques were respectively characterized.

Keywords: Thin film, superstrate, CdTe, CZTS, solar cell, nanostructure.

Contents

Dedication	i
Acknowledgements	ii
Abstract	iv
List of figures.....	x
List of tables	xv
Abbreviations	xvi
1 Introduction	1
1.1 Solar Energy.....	1
1.2 Solar Cell.....	2
1.2.1 Air mass.....	3
1.3 History of Solar Cell.....	4
1.4 Generation of Solar Cells	5
1.5 Solar Cell Terminologies.....	7
1.5.1 Short-circuit Current.....	7
1.5.2 Open-circuit Voltage.....	8
1.5.3 Fill Factor.....	8
1.5.4 Efficiency.....	8
1.6 P-N Junction Solar Cells	9
1.7 Thin Film Solar Cells	9
1.7.1 Thin Film Solar Cells Device Structure	10
1.8 Chalcogenide Thin Film Solar Cells.....	11
1.8.1 CdTe Thin Film Solar Cells	12
1.8.2 Cu ₂ ZnSnS ₄ Thin Film Solar Cells	13
1.8.2.1 Nanostructured Window Layer Based CZTS Thin Film Solar Cells	14

1.8.3	Scope and Objectives of the Present Thesis.....	15
1.9	Outline of this Thesis	16
2	Experimental and Characterization Techniques	18
2.1	Introduction.....	18
2.2	Thermal Evaporation Method.....	20
2.3	Sputtering.....	21
2.4	Spin Coating	22
2.5	Preparation of Alloys.....	23
2.5.1	Thermal Molten Technique.....	23
2.6	Solvothermal/Hydrothermal Method.....	24
2.7	Hot Plate Method.....	25
2.8	Chemical Bath Deposition (CBD)	26
2.9	X-ray Diffraction (XRD).....	27
2.10	Field Emission Scanning Electron Microscopy (FESEM).....	28
2.11	Raman Spectroscopy	29
2.12	Energy Dispersive Spectroscopy (EDS).....	31
2.13	Cathodoluminescence (CL).....	32
2.14	Ultraviolet-Visible (UV-Vis) Spectroscopy.....	33
2.15	X-ray Photoelectron Spectroscopy (XPS)	35
2.16	Transmission Electron Microscopy (TEM).....	37
2.17	Atomic Force Microscopy (AFM).....	38
2.18	Solar Simulator	39
3	Effect of CuPc and PEDOT:PSS as Hole Transport Layers in Planar Heterojunction CdS/CdTe Solar Cell	41
3.1	Introduction.....	42
3.1.1	Objectives of the Work.....	43
3.2	Experimental Details	44
3.2.1	Fabrication of Planar Heterojunction CdS/CdTe Solar Cells.....	44
3.2.2	Characterization of the Deposited Films	46
3.3	Results and Discussion	46
3.3.1	X-ray Diffraction Studies of the Deposited Thin Films.....	46
3.3.2	Raman Spectroscopy Analysis of TiO ₂ , CdS, and CdTe Thin Films.....	48

3.3.3	X-ray Photoelectron Spectroscopy Analysis of TiO ₂ , CdS, and CdTe Thin Films.....	49
3.3.4	Ultra-Violet Photoelectron Spectroscopy Analysis of the Fabricated Thin Films	51
3.3.5	Topographical Studies of the Fabricated Thin Films.....	52
3.3.6	Current-Voltage (I-V) Characteristics of the Fabricated Planar Heterojunction CdS/CdTe Devices	54
3.4	Conclusions	56
4	Controlled Growth of 1D-ZnO Nanotubes Using One-step Hot Plate Technique for CZTS Heterojunction Solar Cells	57
4.1	Introduction	58
4.1.1	Objectives of the Work	59
4.2	Experimental Details	60
4.2.1	The Preparation of ZnO Nanostructures	60
4.2.2	Preparation of CZTS Alloy and ZNRs/CZTS, ZNTs/CZTS Heterojunction Solar Cell.....	61
4.2.3	Characterization Techniques	62
4.3	Results and Discussions	62
4.3.1	Surface Morphology of ZnO Nanostructures.....	62
4.3.2	Systematic Growth Process of ZnO Nanostructures	63
4.3.3	X-ray Diffraction of ZnO Nanostructures.....	64
4.3.4	Raman Spectroscopy Analysis of ZnO Nanostructures	66
4.3.5	X-ray Photoelectron Spectroscopy Analysis of ZnO Nanostructures	66
4.3.6	Optical Properties of ZnO Nanostructures	66
4.3.7	Materials and Optical Properties of CZTS Absorber	67
4.3.8	X-ray Photoelectron Spectroscopy Analysis of CZTS Absorber ..	68
4.3.9	Ultra-Violet Photoelectron Spectroscopy Analysis of ZnO Nanostructures and CZTS Absorber.....	69
4.3.10	Current-Voltage (I-V) Characteristics of Superstrate (ZnO nanostructures/CZTS) Heterojunction Devices.....	70
4.4	Conclusions	71

5	Morphology Controlled n-type TiO₂ and Stoichiometry Adjusted p- type Cu₂ZnSnS₄ Thin Films for Photovoltaic Applications	72
5.1	Introduction.....	73
5.1.1	Objectives of the Work.....	74
5.2	Experimental Details	75
5.2.1	The FTO/TiO ₂ (1D and 3D)/CdS/CZTS/Au Device Fabrication.....	75
5.2.2	Characterization Techniques.....	77
5.3	Results and Discussion	78
5.3.1	The Surface Morphology Studies of TiO ₂ Nanostructured Films, CZTS Thin Film and the Fabricated Hetero- Interface Devices.....	78
5.3.2	X-ray Photoelectron Spectroscopy Analysis of TiO ₂ Nanostructured Films	81
5.3.3	Raman Spectroscopy of TiO ₂ Nanostructured and CZTS Thin Films	82
5.3.4	X-ray Diffraction of TiO ₂ Nanostructured and CZTS Thin Films.....	83
5.3.5	Transmission Electron Microscopy Analysis of TiO ₂ Nanostructured Films	84
5.3.6	Optical Properties of TiO ₂ Nanostructured Films.....	85
5.3.7	Current-Voltage (I-V) Characteristics of the Fabricated (Au/CZTS/CdS/TiO ₂ Nanostructured films/FTO) Devices	87
5.4	Conclusions.....	88
6	Toxic-free Surface Level Sulphur Doped 1D Ti-O_x-S_y Nanorods for Superstrate Heterojunction CZTS Thin Film Solar Cells	89
6.1	Introduction.....	90
6.1.1	Objectives of the Work.....	91
6.2	Experimental Details	92
6.2.1	Preparation of 1D TNRs and 1D S-TNRs Films	92
6.2.1.1	Preparation of Non-Stoichiometric CZTS Absorbing Layer and Device Fabrication	93
6.2.2	Characterization Techniques.....	94

6.3	Results and Discussion.....	94
6.3.1	The Surface Morphology and Compositional Analysis of Pristine TNRs and S-TNRs Thin Films	94
6.3.2	The Crystal Structure and Phase Identification of Pristine TNRs and S-TNRs Thin Films	96
6.3.3	The Chemical State Analysis of Pristine TNRs and S-TNRs Thin Films.....	97
6.3.4	The Optical Properties of Pristine TNRs and S-TNRs Thin Films	98
6.3.5	The Lateral Doping Concentration Studies of 350 °C Annealed S-TNRs Film.....	98
6.3.6	The Current-Voltage Characteristics of Fabricated Heterojunction Devices.....	100
6.4	Conclusions	102
7	Conclusions and Future Scope	103
7.1	Conclusions	103
7.2	Future Scope	104
	Bibliography	106
	Publications based on the thesis	130

List of Figures

1.1	The schematic of solar energy.....	2
1.2	Example of a solar cell.	3
1.3	The solar irradiance spectrum (Altamura (2014))	4
1.4	The schematic diagram of AM.....	4
1.5	The generations of solar cells.....	6
1.6	The equivalent circuit of a solar cell.....	7
1.7	(a) Schematic of P-N junction solar cells, (b) Charge separation in P-N junction.....	9
1.8	The configuration of PV devices (a) Substrate type and (b) Superstrate type.....	10
1.9	Schematic of compound semiconductors.....	11
1.10	The CdTe crystal structure.....	12
1.11	Crystal structure of CZTS (a) Kesterite, (b) Stannite (Minlin Jiang et al. 2014).	13
2.1	The classification of thin film deposition techniques.....	19
2.2	Schematic diagram of thermal evaporation system.....	20
2.3	The schematic diagram of DC and RF magnetron sputtering systems.	22
2.4	The schematic process of the spin coating method.....	23
2.5	(a) Evacuation unit. (b) Quartz ampoule (Inset shows the image of the ingot).	24
2.6	The schematic of Hydrothermal set up.....	25
2.7	The schematic representation of hot plate technique.....	25
2.8	Schematic of the experimental set up of CBD technique.	26
2.9	Schematic of (a) XRD setup, (b) Reflection of X-rays by two adjacent atomic planes.	27
2.10	XRD equipment used in this work.....	28

2.11	The schematic diagram of SEM analysis.....	29
2.12	Carl Zeiss Ultra 55 FESEM used in this work.....	29
2.13	The schematic representation of Raman effect and instrumentation.....	30
2.14	Raman Spectrometer employed in this work.....	30
2.15	The schematic diagram of the EDS analysis.....	31
2.16	The schematic diagram of CL measurement.....	32
2.17	FESEM with CL detector.....	33
2.18	The schematic diagram of UV-Vis instrumentation set up.....	34
2.19	Shimadzu MPC3600 UV-Vis spectrometer.....	34
2.20	The schematic diagram of (a) XPS and (b) UPS analysis.....	36
2.21	Kratos Axis Ultra DLD XPS and UPS equipment.....	36
2.22	The schematic diagram of TEM.....	37
2.23	Titan THEMIS 300 kV from Thermofisher TEM equipment.....	38
2.24	The schematic setup of AFM.....	38
2.25	Bruker Dimension ICON ScanAsyst AFM.....	39
2.26	The schematic set up of Solar simulator.....	40
2.27	Newport Sol3A class AAA solar simulator.....	40
3.1	The schematic diagram of the novel CdS/CdTe planar heterojunction solar cell.....	44
3.2	Cleaned FTO substrate.....	44
3.3	TiO ₂ window layer (100 nm) coated FTO substrate.....	45
3.4	CdS buffer layer (50 nm) coated on the TiO ₂ /FTO substrate.....	45
3.5	CZTS layer (1 μ m) deposited over the CdS/TiO ₂ /FTO substrate.....	45
3.6	PEDOT:PSS (100 nm) spin-coated over CdTe/CdS/TiO ₂ /FTO substrate.....	45
3.7	Au (100 nm) and CuPc (50 nm) deposited on top of PEDOT:PSS/CdTe/CdS/TiO ₂ /FTO substrate.....	46
3.8	XRD patterns of annealed thin films (a) TiO ₂ at 450 °C, (b) CdS at 350 °C, (c) as-prepared CdTe, (d) CdTe at 450 °C.....	47
3.9	Raman spectra of (a) TiO ₂ at 450 °C, (b) CdS at 350 °C, (c) CdTe at 450 °C.....	48
3.10	XPS spectra of annealed (a) TiO ₂ , (b) CdS, (c) CdTe thin films.....	49
3.11	XPS spectra of (a-c) PEDOT:PSS, (d-f) CuPc.....	50
3.12	UPS spectra of annealed TiO ₂ , CdS, and CdTe thin films.....	51

3.13	Optical band gap of deposited (a) TiO ₂ , (b) CdS, (c) CdTe thin films, UPS Spectra of (d) PEDOT:PSS (e) CuPC thin films and (f) schematic band diagram of fabricated devices.	52
3.14	Surface morphology and cross section FESEM images (200 nm scale) of (a) FTO coated on glass, (b) TiO ₂ , (c) CdS, (d) CdTe, (e) PEDOT:PSS, (f) CuPc thin films.	53
3.15	Typical high resolution 3D and 2D AFM topographic images of (a) FTO, (b) TiO ₂ , (c) CdS, (d) CdTe, (e) PEDOT:PSS, (f) CuPc.....	54
3.16	I-V characteristics of solar devices C and D.	55
4.1	Schematic of the hot plate technique used.	59
4.2	ZnO seed layer (50nm) coated FTO substrate.....	60
4.3	ZnO nanostructures (nanorods and nanotubes) deposited on top of FTO substrates.	60
4.4	CZTS layer deposited over ZnO nanostructures/FTO substrates.	61
4.5	Top electrode Au deposited on CZTS/ZnO nanostructures/FTO substrates.....	61
4.6	50,000X magnification FESEM images (inset: cross-sectional view) of ZnO nanostructures grown with concentrations of (a) 25mM:25mM (randomly oriented ZNRs), (b) 50mM:50mM (oriented ZNRs), (c) 75mM:75mM (ZNRs formation), (d) 100mM:100mM (ZNTs transformation), (e) 125mM:125mM (ZNTs formation), (f) 150mM:150mM (ZNTs opening up), (g) 175mM:175mM (ZNTs completely opened up), (h) 200mM:200mM (ZNTs completely distorted).	63
4.7	Schematic of ZnO nanostructures formation v/s variation of precursor concentrations. Bottom: SEM images of ZnO nanostructures. Top: Cross-sectional view of ZnO single nanorod and nanotube.	64
4.8	(a) Photograph (center) and FESEM images depicting the uniform large area (~ 2 cm ²) growth of ZNTs, (b) XRD and (c) Raman spectra of grown 1D-ZnO nanostructures grown using different precursor concentrations.....	65
4.9	(a) and (b) XPS, (c) CL and (d) UV-Visible spectroscopy of 1D-ZnO nanostructures.	67

4.10	(a) XRD, (b) EDS (inset: cross-sectional FESEM images of CZTS/glass substrate), (c) UV-Visible spectrum of CZTS (450 °C annealed) thin films.....	68
4.11	XPS core-level spectra of CZTS (450 °C annealed) thin films (a) Cu 2p, (b) Zn 2p, (c) Sn 3d and (d) S 2p.	69
4.12	(a) and (b) UPS spectra of ZnO nanostructures and CZTS thin film, (c) and (d) schematic band diagram of the ZNRs/CZTS and ZNTs/CZTS heterojunction devices.	70
4.13	I-V spectra of (a) The ZNRs/CZTS, (b) ZNTs/CZTS heterojunction devices.....	71
5.1	The schematic diagram of TiO ₂ nanorods and TiO ₂ combined structures (TiO ₂ nanostructured films) PV device architectures.	74
5.2	Cleaned FTO substrate	75
5.3	TiO ₂ seed layer (50nm) coated FTO substrate	75
5.4	TiO ₂ nanostructured (1D & 3D) films deposited on FTO substrates	76
5.5	CdS coated on TiO ₂ nanostructured (1D & 3D) films/FTO substrates .	76
5.6	CZTS layer deposited on top of CdS/TiO ₂ nanostructured (1D & 3D) films/FTO substrates.....	77
5.7	Top electrode Au deposited on top of CZTS/CdS/TiO ₂ nanostructured (1D & 3D) films/FTO substrates.....	77
5.8	FESEM images of (a & b and c & d) top and (e & f) cross-sectional view of TiO ₂ nanostructured films.....	79
5.9	Cross-sectional FE-SEM image of the devices (a) annealed Cu ₂ Zn _{1.5} Sn _{1.2} S _{4.4} /CdS/TiO ₂ nanorods/FTO and (b) annealed Cu ₂ Zn _{1.5} Sn _{1.2} S _{4.4} /CdS/TiO ₂ combined structures.	79
5.10	FESEM images of (a & b) as-deposited and (c & d) 450 °C annealed CZTS over CdS/TiO ₂ nanostructured films.	80
5.11	XPS spectra of TiO ₂ nanostructured films (a) wide (b) Ti 2p (c) O 1s.	81
5.12	Raman spectra of (a) TiO ₂ nanostructured films, (b) Cu ₂ Zn _{1.5} Sn _{1.2} S _{4.4} thin films.....	83
5.13	XRD patterns of (a) TiO ₂ nanostructured films (b) Cu ₂ Zn _{1.5} Sn _{1.2} S _{4.4} thin films.....	84
5.14	HRTEM and FFT (inset) images of (a) TiO ₂ nanorods (b) TiO ₂ combined structures.....	85

5.15	Spectral behaviour of $(kh\nu)^2$ versus photon energy for TiO ₂ (a) nanorods, (b) combined structures, (C) $(\alpha h\nu)^2$ as a function of photon energy ($h\nu$) for CZTS thin films, (d) schematic band diagram of FTO/TiO ₂ nanostructured films/CdS/CZTS/Au devices.	86
5.16	CL spectra of (a) TiO ₂ nanorods, (b) TiO ₂ combined structures and UPS spectra of (c) TiO ₂ nanorods, (d) TiO ₂ combined structures.....	86
5.17	I-V curve of CZTS/CdS/TiO ₂ nanostructured thin film solar cells (a) TiO ₂ nanorods (b) TiO ₂ combined structures.	87
6.1	Schematic of the S-TNRs film synthesis process.	92
6.2	Sulphur layer (50 nm) coated on TiO ₂ nanorods/FTO substratee.	92
6.3	Post annealed S-TNRs/TNRs/FTO substrate.....	93
6.4	Schematic of Au/CZTS/S-TNRs/TNRs/FTO substrate hetero-interface device.	93
6.5	FESEM images of (a) Pristine TNRs, (b) 350 °C, (c) 450 °C and (d) 550 °C annealed S-TNRs thin films.....	95
6.6	EDS analysis of (a) Pristine TNRs, (b) 350 °C, (c) 450 °C and (d) 550 °C annealed S-TNRs thin films.....	95
6.7	Pristine TNRs and post annealed S-TNRs thin films (a) Raman spectra, (b and c) XRD spectra	96
6.8	XPS high-resolution spectra of (a) Ti 2p, (b) O 1s and (c) S 2p orbitals...	97
6.9	UV-Vis DRS spectra of as-deposited and post annealed films.....	98
6.10	Cross-sectional FESEM image of elemental compositions of 350 °C annealed S-TNRs film.....	99
6.11	(a) Schematic of destructive XPS depth profiling, evaluation in etching cycles XPS spectra of (b) Ti 2p, (c) O 1s and (d) S 2p orbitals.....	100
6.12	Photo I-V characteristics of (a) Pristine TNRs/CZTS, (b) 350 °C, (c) 450 °C and (d) 550 °C annealed S-TNRs/CZTS thin films heterojunction devices.....	101

List of Tables

3.1	The power conversion efficiency of fabricated devices	56
6.1	The efficiency of fabricated PV devices	101

ABBREVIATIONS

a-Si	Amorphous Silicon
AFM	Atomic Force Microscopy
AM	Air Mass
ARCO	Atlantic Richfield Complany
BE	Binding Energy
E_b & CB	Conduction Band
CdS	Cadmium Sulphide
CdTe	Cadmium Telluride
CdSO ₄	Cadmium Sulphate
CH ₄ N ₂ S	Thiourea
CIS	Cadmium Indium Selenide
CIGS	Copper Indium Gallium di-Sulphide
CIGSe	Copper Indium Gallium Selenide
CL	Cathodoluminescence
CuInSe ₂	Copper Indium Selenide
CuPc	Copper(II) Phthalocyanine
CVD	Chemical Vapor Deposition
CZTS	Copper Zinc Tin di-Sulphide
CZTSe	Copper Zinc Tin di-Selenide
DC	Direct Current
DRS	Diffused Reflectance Spectroscopy
DSSC	Dye Sensitized Solar Cell
E_f	Fermi level
E_g	Band Gap
DRS	Diffused Reflectance Spectroscopy
EDS	Energy Dispersive Spectroscopy
ETLs	Electron Transport Layers
FESEM	Field Emission Scanning Electron Microscopy

FF	Fill Factor
FTO	Fluorine Doped Tin Oxide
FWHM	Full Width Half Maximum
GaAs	Gallium Arsenide
GI-XRD	Grazing Incidence X-ray Diffractometer
HCl	Hydro Chloric
He	Helium
HMTA	Hexamethylenetetramine
HTLs	Hole Transport Layers
InGaP	Indium Gallium Phosphide
I	Current
I_{sc}	Short circuit current
J_{sc}	Current density
J_{max}	Maximum Current density
kB	Boltzmann Constant
KE	Kinetic Energy
LHE	Light Harvesting Efficiency
MoO ₃	Molybdenum Oxide
NH ₄	Ammonium Hydroxide
PCE	Power Conversion Efficiency
P_{in}	Power Input
PV	Photovoltaic
PVD	Physical Vapor Deposition
QDs	Quantum Dots
RF	Radio Frequency
R_s	Series Resistance
R_{sh}	Shunt Resistance
SBD	Solution Based Deposition
Se	Selenium
STEM	Scanning Transmission Electron Microscope
Si	Silicon
S-TNRs	Sulphur doped TiO ₂ nanorods
T	Temperature

TCO	Transparent Conducting Oxide
TiO ₂	Titanium Dioxide
UPS	Ultraviolet Photoelectron Spectroscopy
V	Voltage
E _v & VB	Valence Band
V _{bm}	Valence Band Maximum
V _{max}	Maximum Voltage
V _{oc}	Open Circuit Voltage
Φ & WF	Work Function
Xe	Xenon
XRD	X-ray Diffraction
XPS	X-ray Photoelectron Spectroscopy
ZnCl ₂	Zinc Chloride
ZnO	Zinc Oxide
ZNRs	ZnO nanorods
ZNRs	ZnO nanotubes
ZnS	Zinc Sulphide
ZnSe	Zinc Selenide
1D	One Dimensional
3D	Three Dimensional
ν	Efficiency
α	Absorption Coefficient
θ	Angle of Reflection
λ	Wavelength

Chapter 1

Introduction

CHAPTER 1 contains the detailed background and motivations of the present research work. This chapter includes a brief introduction about the need for chalcogenide (binary and quaternary) based thin film solar cells and finding a way of enhancing their device efficiencies by designing novel hetero-interface based architecture. Also, it summarizes the current literature reviews on hole transport layers that were used in CdTe thin film solar cells and also nanostructured electron transport layers employed CZTS thin film solar cells. An insight into the scope and objectives of the present work has been given at the end of the chapter.

1.1 Solar Energy

In the 21st century, the growing world population and their modern lifestyle require more and more electricity. To fulfill those energy demands, recently an increased research interest has been witnessed on harvesting energy from novel renewable and non-renewable resources (Wong and Ho, Wang and Wu (2012), Stolarczyk *et al.* (2018)). In the past several decades, fossil fuels (natural gas and coal) were the most commonly utilized non-renewable energy resources by humans (Gielen *et al.* (2019), Staffell *et al.* (2019)). But they have a major limitation of future availability and disturbance in the ecological balance due to the decomposition reaction of buried living organisms, which majorly causes lung cancer. To overcome such issues, developing technologies with an inexpensive and eco-friendly based renewable energy sources are much needed today. Solar energy is one of the most promising supplements and abundant sustainable energy. For example, three trillion oil barrels (non-renewable

source) can create 1.7×10^{22} Joules of energy, which Sun can supply in 1.5 days. In other words, the energy radiation from the Sun striking the earth's surface is more than enough to power the entire planet (1,20,000 terawatts per day) (Li *et al.* (2014b), Li *et al.* (2016), Gür (2018)). The schematic diagram of solar energy has shown in **Fig. 1.1**.

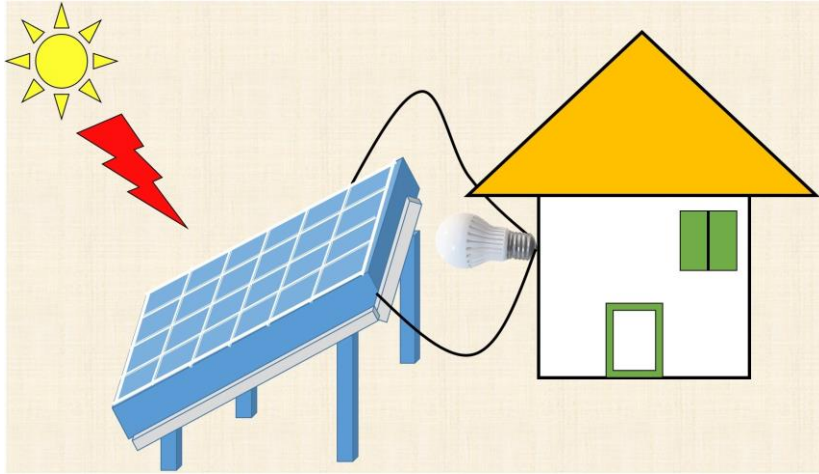


Figure 1.1: The schematic of solar energy.

1.2 Solar Cell

A solar cell or photovoltaic (PV) cell is an optoelectronic device that converts light energy directly into electricity. The name “photovoltaic” came from the Italian physicist Alessandro Volta and mainly refers to the “photovoltaic effect” (Copeland *et al.* (1942)). Generally, the physics of PV is based on the optical and electrical properties of semiconductors. When an energetic photon ($h\nu$) interacts with semiconductor, either it will be absorbed or transmitted or reflected from the surface. That is, if the energy of the incident radiation is less than the semiconductor bandgap (E_g), it will be transmitted. An energy of the incident radiation equal to or higher than E_g will be absorbed and will generate an electron-hole pair. This electron-hole pair is often called an exciton. The performance of a solar cell relies on efficient dissociation of the generated exciton and the collection of separated charge carriers at the respective electrode (**Fig. 1.2**). (Beard (2011)).

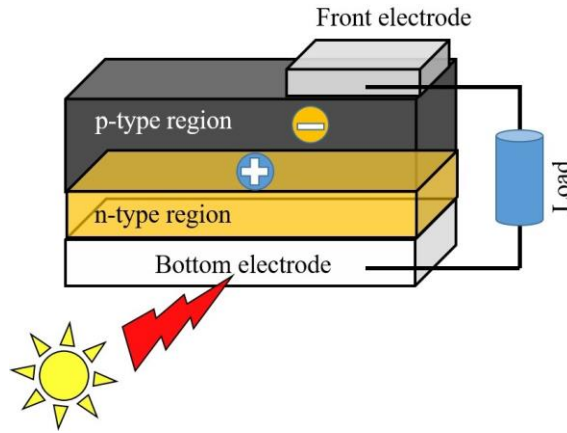


Figure 1.2: Example of a solar cell.

1.2.1 Air mass

Unlike the broad solar energy spectrum striking the earth atmosphere, approximately 5 % in ultra-violet, 43 % in visible and 52 % in infrared region wavelengths are only entering through the earth surface. When it passes, the energy of solar radiation partially undergoes attenuation due to the scattering and absorption effect, which results in the spectral distribution of different wavelengths. **Fig. 1.3** show the solar irradiance spectrum (wavelengths) above the atmosphere and at the earth surface. The quantification of reduction in the power of light energy when it passes through the atmosphere (path length) is called Air Mass (AM) (**Fig. 1.4**) (Riordan and Hulstron (1990)).

The AM is defined as shown in below equation:

$$AM = \frac{1}{\cos\theta} \quad (1.1)$$

where θ is the angle of vertical direction (zenith angle). When the Sun is at the zenith ($\theta = 90^\circ$), the standard spectrum corresponds to AM 1 while the standard spectrum outside the earth's atmosphere is AM 0. With the direction of Sun at $\theta=48.2^\circ$, the spectrum at the earth's surface is called AM 1.5G (G stands for global). The standard spectrum AM 1.5G has been normalized to give 1 kW/m^2 , which is used to measure the device performance at any laboratory condition (Minnaert and Veelaert (2014)). In general, the Xenon (Xe) arc lamp with a variety of filters with different air mass densities contained in solar simulators are often used to mimic the solar spectrum to characterize the PV devices (Riordan and Hulstron (1990)).

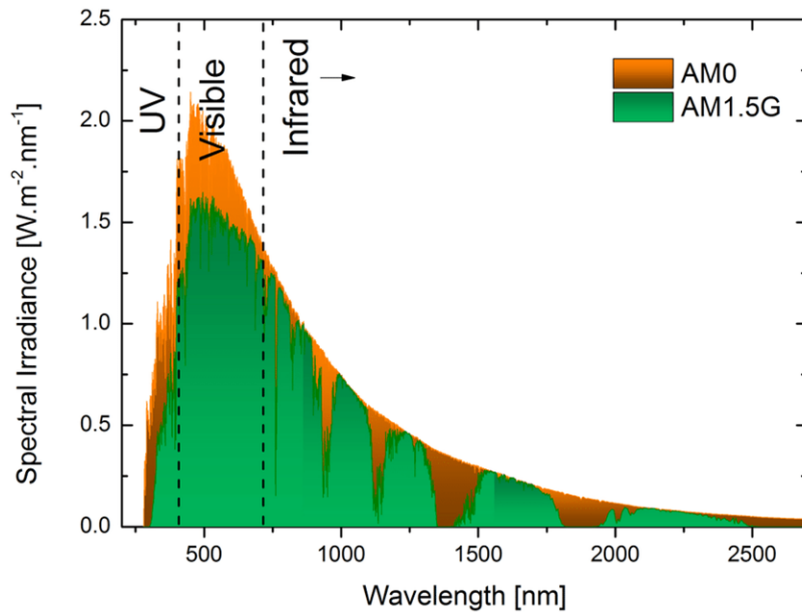


Figure 1.3: The solar irradiance spectrum (Altamura (2014))

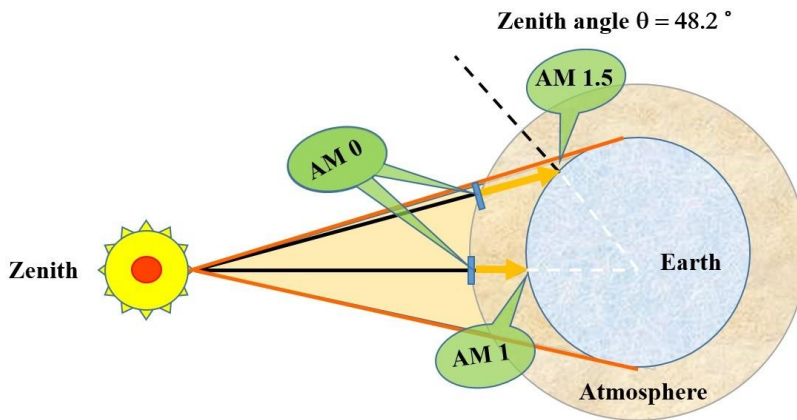


Figure 1.4: The schematic diagram of AM.

1.3 History of Solar Cell

The first photovoltaic effect was discovered by French physicist Edmond Becquerel in **1839** (Heering and Höttecke (2014)). When the solution immersed copper plates were exposed to light, he observed a continuous flow of electrons. Later in **1883**, selenium (Se) based solar cells with 1 % efficiency was reported by American engineer Charles Fritts (Zhu *et al.* (2019)). Se is not a promising solar material for energy conversion because of its toxicity, high cost and low power conversion efficiency (PCE). The

photovoltaic effect in cadmium sulphide (CdS) was discovered by Audobert and Stora in **1932** (Abbe and Smith (2016)). Later, Gordon Teal and John little (in **1948**) constructed a single-crystalline germanium based PV device with the recorded cell efficiency of 8 % (Fraas (2014)). The first p-n junction based silicon (Si) photovoltaic device was demonstrated by the Bell laboratories in **1954** (Yun *et al.* (2018)).

Years later, in the **1960**'s and **1970**'s, Si technology has emerged with an increased efficiency of up to 15 % (Ellis and Moss (1970)). The first commercial thin film PV module was introduced by Atlantic Richfield Company (ARCO) solar (G-4000) in 1986 (Zweibel *et al.* (1990)). A photoelectrochemical cell which is also called a dye-sensitized solar cell (DSSC) (a sandwich-type solar cell) was invented by Michael Gratzel in **1991** (Grätzel and O'Regan (1991)). A year later, in **1993** the thin film PV device with the highest efficiency of 15 % was recorded by the University of South Florida researchers (Britt and Ferekides (1993)). In **2009**, Kojima and Teshima were developed an organometal halide perovskites based solar cells with the conversion efficiency of 3.8 % (Kojima *et al.* (2009)). After a decade in **2019**, the multi-layered perovskite tandem cell was reported with a maximum efficiency of 29.1 % (Köhnen *et al.* (2019)).

1.4 Generation of Solar Cells

Typically, the solar cells are classified into first, second and third-generation type PV cells (**Fig. 1.5**). The first-generation solar cells are based on single-crystalline Si, multi-crystalline Si, gallium arsenide (GaAs), and indium gallium phosphide (InGaP) (Goetzberger *et al.* (2003), Bauhuis *et al.* (2009), Bhattacharya and John (2019)). Among them, the oldest and most commonly used Si (wafer type) solar cell has the potential advantage of high-performance stability, which helps to produce relatively increased PCE based devices in the commercial market. Besides, Si solar cell is one of the most efficient PV technologies available for residential use and account for around 80 % of all the solar panels sold around the world (Tobias *et al.* (2011)). In 2017, Yoshikawa *et al.* were reported 26.7 % as the highest efficiency of Si (crystalline) solar cell (Yoshikawa *et al.* (2017)). On the other hand, a direct bandgap group III/IV semiconductor material GaAs is also utilized as a solar absorber, where efficiency is a prime objective than cost, such as the space industry. The maximum efficiency of 38.1 % was reported for single crystal GaAs solar cell (Milanova and Khvostikov (2000)).

Due to its direct bandgap, the excitation of an electron does not require the aid of a phonon for momentum transfer, resulted in producing higher efficiency than Si solar cells (Bauhuis *et al.* (2009)). However, owing to indirect bandgap of Si, expensive material processing and high production cost, the first-generation PV devices were replaced with the second-generation or thin film solar cells.

First Generation	Second Generation	Third Generation
Si GaAs	Amorphous Si CdTe CIGS CZTS	Dye sensitized solar cell (DSSC) Quantum dots solar cell Organic solar cell Polymer solar cell Perovskite solar cell Nanocrystalline solar cell

Figure 1.5: The generations of solar cells.

The second-generation solar cells are based on amorphous silicon (a-Si), cadmium telluride (CdTe), cadmium indium selenide (CIS), copper indium gallium di-sulphoselenide (CIGS/Se) and copper-zinc tin di-sulphoselenide (CZTS/Se) (Deng and Schiff, 2003, Gorji and Houshmand (2013), Jun-Feng *et al.* (2015), Hussein and Yazdani (2019), Khrypunov *et al.* (2019)). Usually, thin film PV cells are fabricated by a cost-effective thin absorber layer (few nm to $\sim 10 \mu\text{m}$) deposited over the conducting substrate. Besides, the above mentioned thin film semiconductors have the advantages of being direct bandgap and possessing a higher absorption coefficient, which helps to absorb the solar energy spectrum by less than $1 \mu\text{m}$ thick layer (which is 1000 times lower than Si) (Bai *et al.* (2011)). So far, these type thin film PV devices were reported with lesser PCE (maximum 18 %) as compared to first-generation solar cells. A continuous research is being carried out to increase the device PCE and reduce the production cost (Singh *et al.* (2017), Jhuma *et al.* (2019)). Moreover, the first and second generations solar cells are limited (for single p-n junction) by the Shockley-Queisser theoretical limit (maximum $\sim 30 \%$) (Polman *et al.* (2016)). To overcome such issues, a third-generation solar cells were introduced.

The third-generation cells are based on DSSCs, perovskite solar cells, organic solar

cells, quantum dots (QD) solar cells, polymer solar cells, and nanocrystalline solar cells, (Murakoshi *et al.* (1998), Kumar *et al.* (2011), Taya *et al.* (2013), Liu (2014), Periyat and Ullattil (2015), Baig *et al.* (2020)). Importantly, these type cells are different from the previous generation in the sense that it does not rely on the p-n junction to separate the excited charge carriers. Besides, the third-generation solar cells have the potential advantages of facile, quick, eco-friendly and low-cost device fabrication (Smestad *et al.* (2003), Baig *et al.* (2020)). However, as compared to other two-generation cells these materials have poor stability, which makes it difficult to commercialize (Kim *et al.* (2012)).

1.5 Solar Cell Terminologies

The equivalent circuit of solar cells is expressed by a parallelly connected current source and forward biased diodes along with series (R_s) and parallel shunt (R_{sh}) resistances (the reason for various carrier loss mechanisms) shown in **Fig. 1.6**. An ideal cell works with zero R_s and infinitely large R_{sh} , but in practice this condition is not applicable (Cibira (2018)).

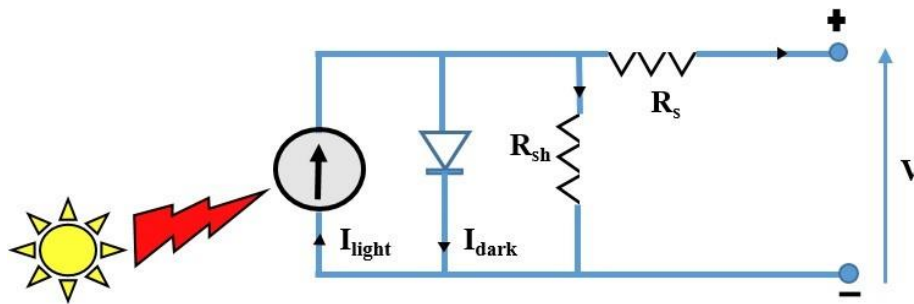


Figure 1.6: The equivalent circuit of a solar cell.

1.5.1 Short-circuit Current

The short circuit current (I_{sc}) is the maximum current drawn from the solar cell when the voltage or load resistance across the device is zero. The I_{sc} increases with the concentration of incident photons which in turn enhances the electron-hole pair generation (Baig *et al.* (2020)). I_{sc} is mainly dependent on the cell area, therefore it normally represents as current density J_{sc} .

$$J_{sc} = \frac{I_{sc}}{A} \text{ (mA/cm}^2\text{)} \quad (1.2)$$

where A is the effective area of the PV cell.

1.5.2 Open-circuit Voltage

The open-circuit voltage (V_{oc}) is the maximum voltage drawn from the solar cell when the current across the device is zero or load with infinite resistance. The V_{oc} is a function of charge carrier recombination in the device and semiconducting material's bandgap (Elumalai and Uddin (2016)). Besides, V_{oc} mainly depends on the photo-generated current density, which described by equation(1.3).

$$V_{oc} = \frac{qV}{kBT} * \ln \frac{J_{sc}}{J_o + 1} \quad (1.3)$$

where J_o is reverse saturation current, kB is Boltzmann constant, T is temperature, q is the electron charge and V is the voltage.

1.5.3 Fill Factor

The fill factor (FF) is the maximum power output drawn from the solar cell when the device is illuminated with concentrated photon flux (Baig *et al.* (2020)). It is defined as the ratio of maximum power to the product of J_{sc} and V_{oc} of the solar cell.

$$FF = \frac{V_{max} \times J_{max}}{V_{oc} \times J_{sc}} \quad (1.4)$$

where J_{max} is the maximum current density and V_{max} is the maximum voltage of the cell.

1.5.4 Efficiency

The efficiency of the PV cell is defined as the ratio of power output from the solar cell and the power input of the solar radiation. The solar cell PCE majorly depends on the incident photons intensity radiation, air mass, and operating temperature (Baig *et al.* (2020)). The mathematical definition of efficiency (η) is

$$\eta = \frac{V_{oc} \times J_{sc} \times FF}{P_{in}} \quad (1.5)$$

where P_{in} power input of solar radiation.

1.6 P-N Junction Solar Cells

The first and second-generation photovoltaic cells consist of p-type (majority carriers are hole) and n-type (majority carriers are electrons) semiconductors which are placed in contact to form a p-n junction (shown in **Fig. 1.7** (a)) (Kayes *et al.* (2005)). A junction formed by the same semiconductor is called homojunction, while that formed with dissimilar type is called heterojunction. Moreover, due to the diffusion of charge carriers at the depletion region, there is a formation of built-in electric field (without any external bias). The photon absorption from sunlight generates the electron-hole pair at the interface. The built-in electric field help to separate the photoexcited charge carriers and transport them towards respective (positive and negative) electrodes (**Fig. 1.7**(b)).

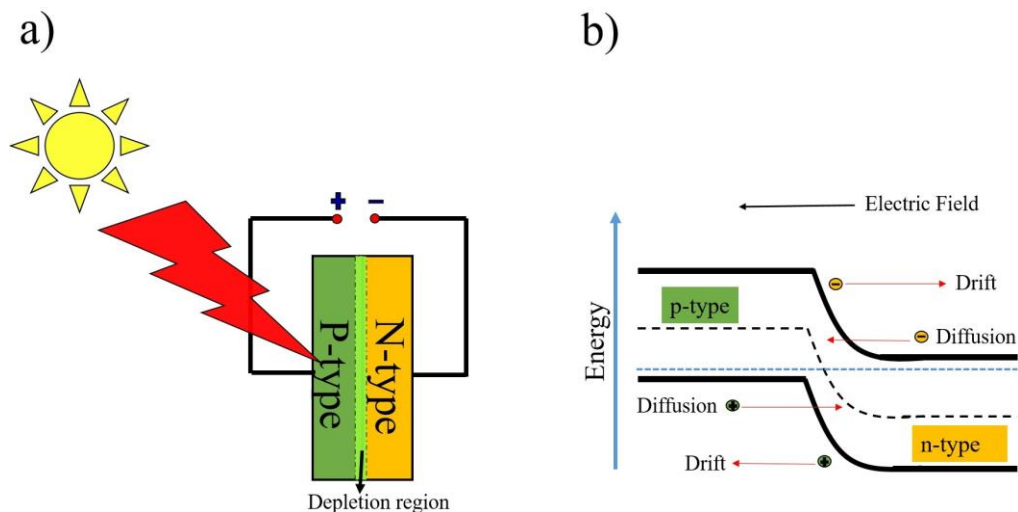


Figure 1.7: (a) Schematic of P-N junction solar cells, (b) Charge separation in P-N junction.

1.7 Thin Film Solar Cells

Thin film solar cells are developed to overcome the higher material consumptions, production volume and cost of first-generation PV devices. In contrast with Si (wafer

type) solar cells, thin film semiconductors have a higher absorption coefficient which results in less material consumption. Also, thin film solar absorbers have some important advantages such as tuneable optical bandgap and facile deposition over any flexible substrate, which allows one to completely make an efficient next generation solar module (Stark *et al.* (2015), Singh *et al.* (2017), Jhuma *et al.* (2019)).

1.7.1 Thin Film Solar Cells Device Structure

In thin film solar cell technology, typically two types of configuration are followed to fabricate PV device such as “substrate” and “superstrate”. The former configuration has the advantage of using any type of substrate (flexible polymers, stainless steel, etc.), opaque or transparent where the light passes through the cell before striking the substrate (Fig. 1.8(a) (Deng and Schiff (2003), Kumar *et al.* (2015), Tumbul *et al.* (2019)). On the other hand, in the superstrate configuration the light strikes the substrate (must be transparent) before being absorbed by the solar cell (Fig. 1.8(b)). The choice of configuration depends on the type of technology utilized to construct the PV device (McCandless and Sites (2011)).

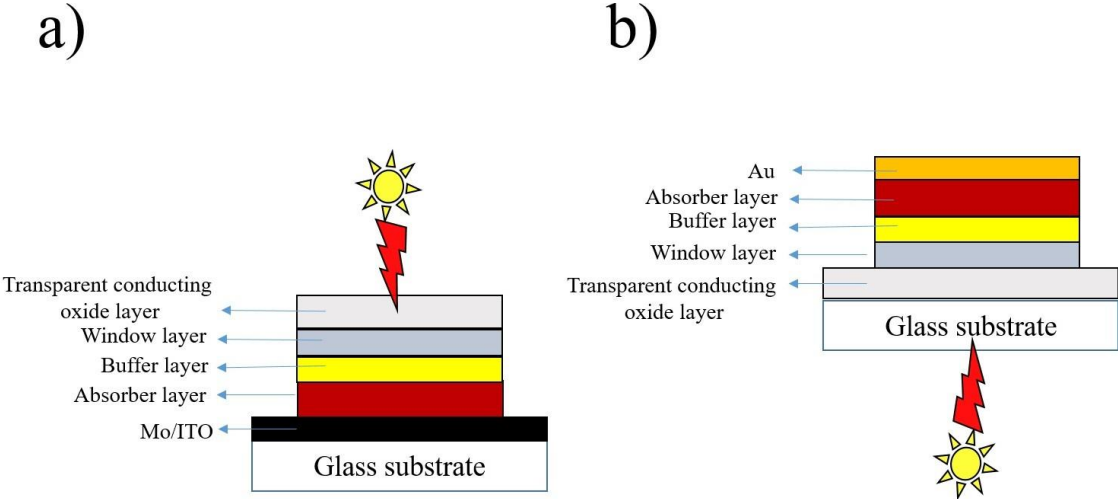


Figure 1.8: The configuration of PV devices (a) Substrate type and (b) Superstrate type.

1.8 Chalcogenide Thin Film Solar Cells

To find a better alternative absorber for Si, the binary compounds such as GaAs and CdTe were formed, by the implementation of isoelectronic substitution of equal number of cations and anions in group III, V and II, VI (Bauhuis *et al.* (2009), Romeo *et al.* (2014)). Similarly, to form the ternary chalcogenides, the group II element are partially substituted by group I and group III elements, for example, copper indium selenide (CuInSe_2) (Shafarman *et al.* (2011)). Other replacements are also possible by substituting half of group III element with group II element and a half with group IV element, for example copper zinc tin sulphide ($\text{Cu}_2\text{ZnSnS}_4$ or CZTS) (shown in **Fig. 1.9**) (Sripan *et al.* (2016)). Moreover, these chalcogenide semiconductors have an optimal direct bandgap of ~ 1.5 eV at 300 K and a higher optical absorbance coefficient ($\alpha > 10^4 \text{ cm}^{-1}$), which makes them an ideal candidate for fabricating highly efficient solar cells. However, it is proven that all the combinational substitution will not work or PV applications (Aldakov *et al.* (2013), Lee *et al.* (2015)).

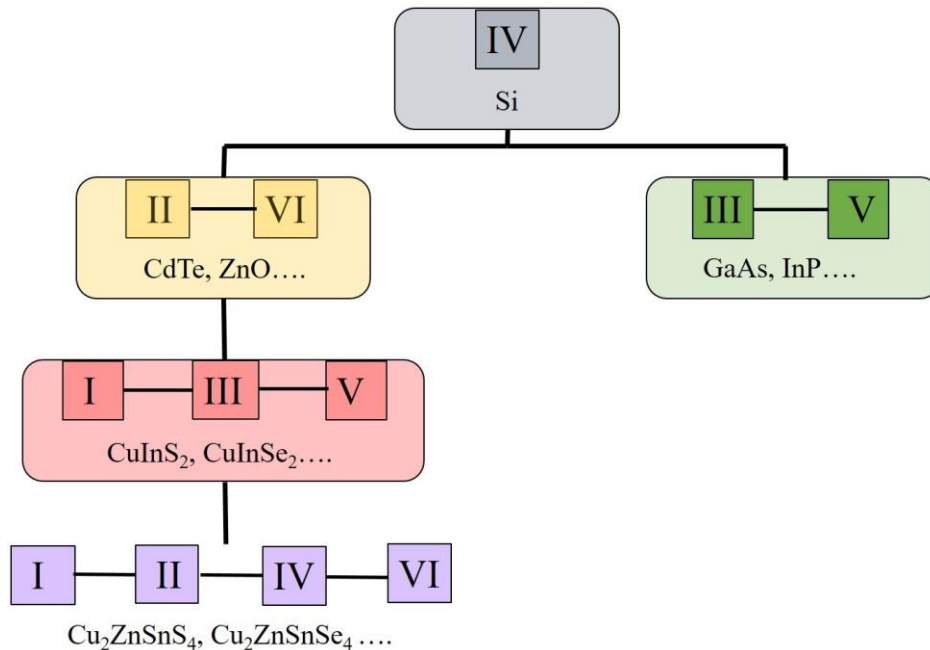


Figure 1.9: Schematic of compound semiconductors.

1.8.1 CdTe Thin Film Solar Cells

Cadmium based binary (II-VI) chalcogenide such as CdTe has long been recognized as an optimal light harvesting absorbing candidate for making thin film PV devices (Mitchell *et al.* (1977), Razykov *et al.* (2012)). Besides, CdTe has many advantages of chemical stability, direct bandgap ($E_g \sim 1.45$ eV) and ambipolar doping behaviour (it can be doped either as n-type or p-type). However, in PV applications CdTe is widely used as a p-type absorber (Romeo *et al.* (2014)). CdTe forms a zincblende crystal structure, in that each Cd atom is tetrahedrally surrounded by four Te atoms (**Fig. 1.10**). Generally, the CdTe solar cells are fabricated in superstrate configuration, such as combining p-CdTe absorber with its common heterojunction n-type partner CdS (Romeo *et al.* (2014)). Green, M. A et al. had reported the highest PCE of 22.1 % for CdS/CdTe heterojunction based thin film solar cells (Green (2017)).

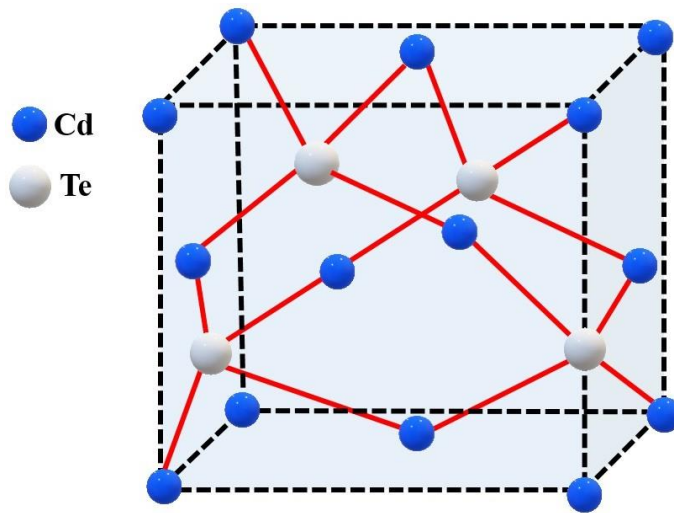


Figure 1.10: The CdTe crystal structure.

Usually, CdS/CdTe solar cell requires $> 2 \mu\text{m}$ thick absorbing layer to absorb the entire solar energy spectrum. At the same time, when the CdTe layer thickness exceeds $> 1 \mu\text{m}$, the performance of the PV device decreases due to carrier recombination (Bai *et al.* (2011)). To date, the CdTe photovoltaic technology has been already commercialized and recognised as one of the best selling products among thin film solar cells. But still research lies in reducing the CdTe layer thickness (to lower the production cost), finding a suitable back contact and designing a novel device architecture to enhance the device PCE.

1.8.2 $\text{Cu}_2\text{ZnSnS}_4$ Thin Film Solar Cells

In the past few decades, inorganic quaternary semiconductors have paid huge attention in the context of developing clean sustainable energy technologies. The I-II-IV-VI semiconductor CZTS has similar properties with CIGS, which makes it possible to develop cost-effective and risk-free high-performance solar modules (Dhawale *et al.* (2019)). Further, CZTS has the potential advantages of being less toxic compared to CIGS and CdTe. The $\text{Cu}_2\text{ZnSnS}_4$ belongs to quaternary compounds of adamantine family $A^{II}-B^{II}-C^{IV}-X^V$ can be represented by the general formula of $(N=2) A^{2N-1}B^{2N-2}C^{N+2}X_4^{8-N}$ ($A = \text{Cu, Ag, Au}$, $B = \text{Zn, Cd, Hg}$, $C = \text{Sn, Ge, Si}$, $X = \text{S, Se, Te}$). Typically, it has two different crystal structures: kesterite (space group I) and stannite (space group $I 2m$). Both are tetragonal expansion of zinc blende and the only difference is the occupation of Cu and Zn atoms in the sublattices (**Fig. 1.11**). Also, the CZTS compound appears in the kesterite crystal phase (Cu poor Zn rich) is more stable than stannite phase (Cu rich Zn poor) (Todorov *et al.* (2010)).

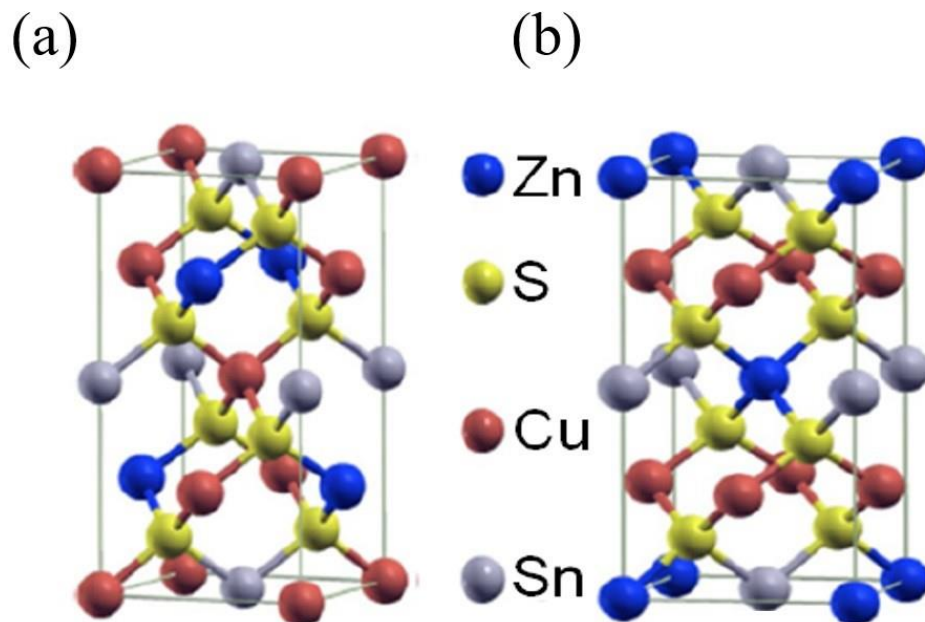


Figure 1.11: Crystal structure of CZTS (a) Kesterite, (b) Stannite (Minlin Jiang *et al.* 2014).

According to the Shockley-Quiesier limit, theoretically calculated PCE of CZTS

thin film solar cell is 32.2 %. But, while adjusting the stoichiometry ratio of its constituent elements $\text{Cu}/(\text{Zn}+\text{Sn}) = 0.80$ and $\text{Zn}/\text{Sn} = 1.2$ or higher than 1 (Zn-rich), Son *et al.* experimentally reported PCE of $\leq 12.6\%$ (Son *et al.* (2019)). Importantly, when the composition of Cu and Sn are high, the performance of the solar cells is extremely poor (because of increased resistance). Moreover, Zn-rich condition helps reduce the secondary phases such as Cu-Sn-S, Cu-S, and Sn-S in the crystal. Therefore for enhancing the PCE of the future devices, it is important to synthesise the compound with low defect density and as well as control the stoichiometry ratio of Cu, Zn, Sn and S without any secondary phases. Recently, further to augment the light harvesting efficiency (LHE) and charge carrier transport in CZTS thin film solar cells, many researchers have attempted choosing an effective photoanode or window layer along with the buffer layer in their hetero-interface geometry (Kaur *et al.* (2017), Kurokawa *et al.* (2012), Yan *et al.*, 2018a).

1.8.2.1 Nanostructured Window Layer Based CZTS Thin Film Solar Cells

In heterojunction solar cells, in order to transport the excited charge carrier effectively, wide bandgap oxide semiconductors such as titanium dioxide (TiO_2) and zinc oxide (ZnO) are most extensively used as photoanode or window layer. These materials show high transparency in the visible region, are low cost, non-toxic, and possess large refractive index, making them an ideal n-type material in thin film solar cells. Also it is proved that, compared to the planar CZTS thin film devices, one dimensional (1D) nanostructured photoanodes have the potential advantage of transporting the photogenerated electrons in an uninterrupted electrical pathway towards the bottom electrode (Liu and Aydil (2009), Roy *et al.* (2010)). In recent years, there is an increased research interest in fabricating the nanostructure incorporated superstrate structured CZTS thin film solar cells. Moreover, as compared to the conventional substrate type solar cells, it is proven that these type of devices help avoid the encapsulation complexity and the charge carrier recombination loss. Besides, this superstrate configuration is considered as one of the most suitable approaches to study the advantages of 1D nanostructures in heterojunction PV devices (Berruet *et al.* (2017), Tumbul *et al.* (2019), Yan *et al.* (2018a)). To date, there are only few research reports available in the literature on nanostructures (TiO_2 and ZnO) employed superstrate CZTS thin film solar cells.

1.8.3 Scope and Objectives of the Present Thesis

Present thesis describes the design and development of superstrate configuration of binary p-CdTe and quaternary p-CZTS chalcogenides based thin film solar cells. The main aim of the thesis work is to address the selection of thin absorber layer and back contact issues in CdTe solar cells and to study the properties of nanostructured (1D and 3D) window layer in CZTS thin film solar cells. To enhance the efficiency of CdTe thin film solar cells, various strategies have been employed by choosing a suitable back contact, electron transporting layers (ETLs) and hole transporting layers (HTLs) in the device architecture. CdTe solar cells are being extensively studied with various ETLs such as CdS, zinc sulfide (ZnS), zinc selenide (ZnSe), TiO₂ (Britt and Ferekides (1993), Karaagac *et al.* (2013), Liu *et al.* (2015)). Also, to avoid the Schottky or to form ohmic contact in CdTe solar cells, inorganic molybdenum oxide (MoO₃), organic SPIRO OMeTAD (N2,N2,N2⁰,N2⁰,N7,N7,N7⁰,N7⁰-octakis(4-methoxyphenyl)-9,9⁰-spirobi[9H-fluorene]-2,2⁰,7,7⁰-tetramine), PEDOT:PSS (poly(3,4-ethylene dioxythiophene) polystyrene sulfonate) and poly(3-hexythiophene-2,5-diyl) (P3HT) were comprehensively studied as HTLs (Khrypunov *et al.* (2010), Jarkov *et al.* (2011), Ye *et al.* (2011), Du *et al.* (2016), Major *et al.* (2017)).

In this thesis, the fabrication of a novel chalcogenide based (superstrate) heterojunction PV cell along with two HTLs (back contacts) is presented. Also, the thesis discusses the fabrication and characterization of superstrate heterojunction based CZTS PV devices that are employed with the photoanodes of 1D-ZnO nanorods & nanotubes, 1D-TiO₂ nanorods & 3D-TiO₂ hierarchical nanostructure, and sulphur diffused 1D-TiO₂ nanorods. With these research scopes, the following objectives have been addressed in the present thesis.

1. To fabricate and characterize the photovoltaic performance of new architecture based planar heterojunction CdS/CdTe thin film solar cells were employed with two HTLs (PEDOT:PSS as HTL1 and copper(II) phthalocyanine (CuPc) as HTL2).
2. To develop a simple and rapid one-step hot plate technique for systematic growth transformation of highly oriented ZnO nanorods (ZNRs) into ZnO nanotubes (ZNTs) over fluorine doped tin oxide (FTO) substrate for hetero-interface stoichiometry adjusted Cu₂Zn_{1.5}Sn_{1.2}S_{4.4} thin film solar cells.
3. To combine n-type TiO₂ 1D & 3D nanostructures and stoichiometry adjusted

p-type CZTS materials for superstrate CZTS solar cells (FTO/TiO₂ 1D/3D nanostructures/CdS/CZTS/Au).

4. To develop a novel and facile non-toxic way to dope (surface level) sulphur atom into 1D TiO₂ nanorods for heterojunction stoichiometry adjusted superstrate CZTS solar cells.

1.9 Outline of this Thesis

The research work presented in this thesis is divided into 7 chapters.

- With the current chapter laying the background for the thesis with literature survey, research gaps and motivation, scope of the thesis and research objectives, **CHAPTER 2** provides a detailed introduction to the experimental and characterization techniques used in the present work. The first section contains the experimental part, which includes a description of the physical vapor deposition (PVD) techniques such as thermal evaporation, radio frequency (RF) sputtering and solution based deposition (SBD) techniques such as chemical bath deposition, spin coating which were used to deposit the thin films. It also presents a brief discussion of the hydrothermal and the hot plate methods, which were used to grow the nanostructures throughout this research work. The second section describes the characterization techniques employed to study the fabricated devices. This includes a detailed description of field emission scanning electron microscopy (FESEM), Raman spectroscopy, X-ray diffraction (XRD), Cathodoluminescence (CL), X-ray photoelectron spectroscopy (XPS), ultraviolet photoelectron spectroscopy (UPS), energy dispersive spectroscopy (EDS), UV-Vis spectroscopy, transmission electron microscopy (TEM) and evaluation of the fabricated solar cells employing an AM 1.5G Solar simulator.
- **CHAPTER 3** investigates the effect of CuPc (HTL2) along with PEDOT:PSS (HTL1) employed as hole transport layers in CdS/CdTe thin film planar heterojunction solar cells. Due to the incorporation of CuPc in the device architecture, the enhancement of PCE is discussed. Moreover, the band engineering between the absorbing layer, electron, and hole transporting layers was investigated.
- **CHAPTER 4** deals with the formation of high aspect ratio and highly oriented ZNRs over the seeded FTO substrate using a single hot plate technique without offering any templates or catalysts. Besides, by varying the precursor concent-

ration and keeping the same reaction time, the ZNRs were transformed into vertical ZNTs. As-grown ZnO nanostructures (ZNRs and ZNTs) were characterized to confirm their crystal structure, surface morphology, phase, optical energy gap. Further, grown ZNRs and ZNTs were employed in the fabrication of CZTS heterojunction (ZNRs/CZTS and ZNTs/CZTS) photovoltaic devices.

- **CHAPTER 5** describes a single-step hydrothermal method to grow highly oriented TiO₂ 1D nanorods over FTO substrates. Besides, an attempt to construct and study the inverted (superstrate) type CZTS solar cells combined with n-type TiO₂ 1D/3D nanostructures as a window layer is presented.
- **CHAPTER 6** is devoted to developing a non-toxic (H₂S free) way to dope (surface level) sulphur atoms into a 1D-TiO₂ matrix via thermal evaporation followed by post-annealing (350°C, 450 °C and 550 °C). Also, it discusses an attempt made to develop and study the Cadmium (Cd) free superstrate structured thin film solar cells by combining sulphur doped TiO₂ nanorods (S-TNRs) and stoichiometry adjusted CZTS thin film.
- **CHAPTER 7** provides the general conclusion of the present investigation and future scope of the work.

Chapter 2

Experimental and Characterization Techniques

2.1 Introduction

In the past several decades, thin film synthesis of new (electronic and magnetic) materials has invited a huge attention in the era of microelectronics, optoelectronics and nanotechnology (Sequeda (1986), Bergman *et al.*, 1999, Pechkova and Nicolini (2002)). Thin film deposition is the process of depositing the materials over the surface of the substrate with film thickness ranging from $<100 \text{ \AA}$ (ultra-thin), $<1000 \text{ \AA}$ (thin) and $>1000 \text{ \AA}$ (thick films). In general, thin film deposition involves three major sequential steps such as absorption, nucleation, and diffusion of atoms and molecules. In brief, initially atoms and molecules of the material to be deposited absorb on the surface of substrate. This process is followed by the diffusion of atoms and molecules to the already absorbed species to form the bonds (aggregation) of the film. This process is called nucleation. Finally, the diffusion occurs within the bulk of the film over the substrate to form thin films (Okuyama *et al.* (1991), Feng *et al.* (1993), Mattox (2010), Rosnagel (2003)). Through thin film processing, it becomes possible for any desired material to attain geometrical, topographical, physical, crystallographic and metallurgical structures in two or lesser dimensions (Mehla *et al* 2019).

So far, the methods employed for thin film deposition are broadly classified into three major categories such as chemical vapor deposition (CVD), PVD and the SBD. In CVD, the films are formed on the substrate through chemical reactions of the precursors while in PVD, the films are deposited (under vacuum) directly onto the substrate. In SBD, the films are deposited via the solution process (**Fig. 2.1**) wherein the material to be deposited is dissolved in a suitable solvent to make a uniform and homogeneous solution. This solution is then either spin coated or dip-coated on a suitable substrate. Among the three, PVD is the most favored processing technique to deposit compound semiconductors. PVD can be further divided into three categories such as vacuum or thermal evaporation, ion plating and sputtering (Feng *et al.* (1993), Rossnagel (2003)). During the thermal evaporation process, thermal effect causes the ejection of atoms from the source material by evaporation. The vaporized material then condenses on the substrate's surface forming a thin film. In the ion plating process, the substrate is exposed to concurrent ion bombardment. On the other hand, in the sputtering process, atoms or molecules are ejected from the surface of the solid target by the impact of gaseous ions and then deposited on the surface of the substrate. To attain high purity thin films, the deposition processes should be carried out under high vacuum conditions (10^{-5} torr or more) (Ramasamy *et al.* (2012)). A typical PVD instrument consists of rotary vacuum pump, vacuum chamber, vacuum gauge, diffusion or a turbomolecular pump, thickness monitor, rotary drive, substrate heater and other controlling electronics.

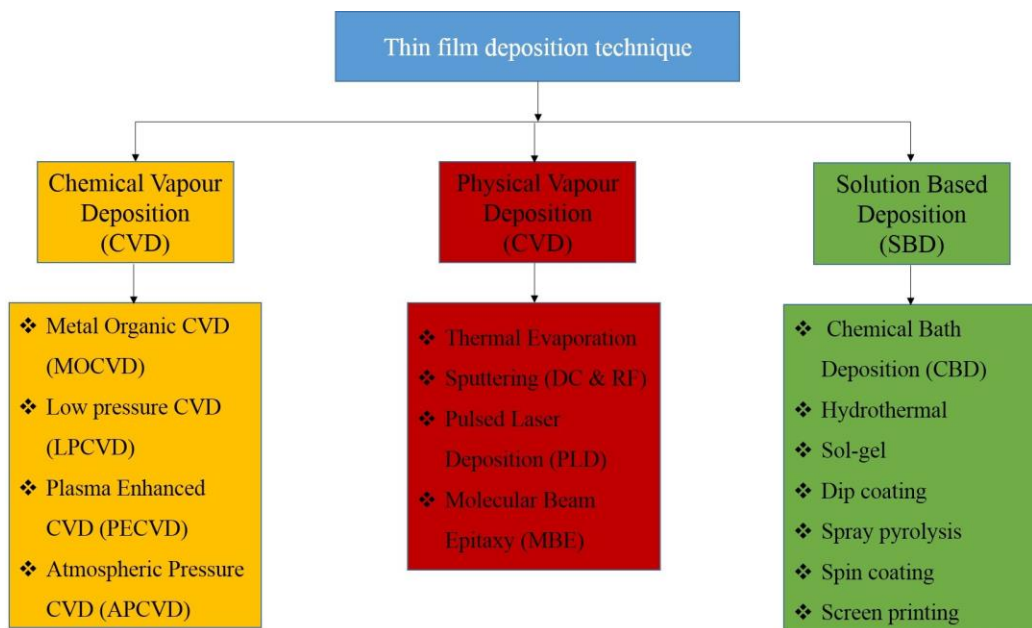


Figure 2.1: The classification of thin film deposition techniques.

This chapter discusses various vacuum based PVD processes like thermal evaporation and sputtering, as well as solution processed surface coating techniques such as hydrothermal or solvothermal, direct hot plate, CBD and spin coating. Furthermore, it explains the characterization techniques used in this research work such as XRD, FESEM, Raman spectroscopy, UV-Vis spectroscopy, EDS, CL, TEM, XPS, UPS, and Solar simulator.

2.2 Thermal Evaporation Method

One of the most commonly used PVD technique is thermal evaporation. The basic process of this technique involves sublimation of the source material at high temperature in a closed vacuum chamber to form desired thin films (Sripan *et al.* (2017b)). The material to be deposited is loaded into a container called the crucible. The material contained in the crucible is resistively heated by applying a large current. Consequently, material in the crucible evaporates, during which the atoms/molecules of the evaporated material travel undeflected until they strike the surface of the substrates, where they accumulate as a film. **Fig. 2.2.** represents the schematic diagram of the thermal evaporation set-up.

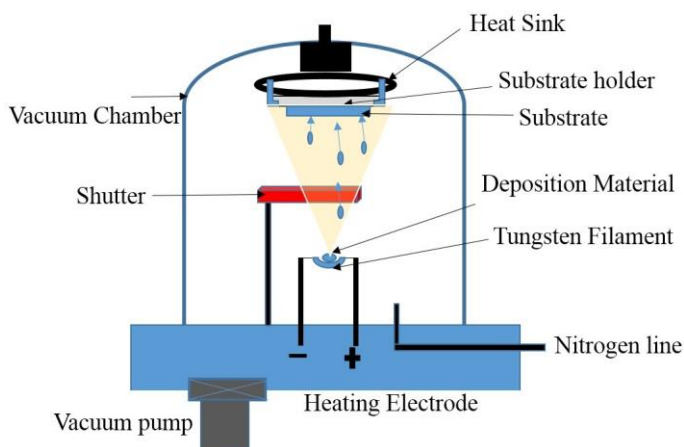


Figure 2.2: Schematic diagram of thermal evaporation system.

Usually, the substrate and the source of material are positioned suitably to attain uniform deposition inside an evacuated glass/metal chamber. The selection of heating source (crucible) mostly depends on the melting point of the evaporated source material, so that it does not react chemically while deposition. Before further use, initially,

the source holder (tungsten, molybdenum or tantalum) is thoroughly cleaned by applying high current between heating terminals (electrodes) for removing the surface impurities using flash evaporation process. The deposition rate and film thickness can be controlled by controlling the heating current which directly controls the rate of evaporated material.

2.3 Sputtering

Among the PVD processes, sputtering is considered one of the most vital non-thermal vaporization processes (Ramasamy *et al.* (2012)). The main concept of the sputtering process is the ejection of surface atoms of the target material (negatively charged) by momentum transfer due to the bombardment of gaseous (usually Argon) ions (positively charged). The ejected material deposits on the substrate to produce a thin layer coating over the substrate. In other words, under vacuum, due to a high potential difference across electrodes, a low pressure gas gets ionized to produce plasma or glow discharge. Subsequently, energetic ions in the plasma are attracted to the positively charged target material (cathode) which causes the ejection of cathode material. The sputtering process commonly uses Argon (Ar) gas which offers the provision for sputtering of large ions in an inert atmosphere to avoid the chemical reaction with the target materials. Sputtering can be of two types, direct current (DC) sputtering and RF sputtering (**Fig 2.3**).

DC sputtering is a process in which the target material acts as a cathode (negative potential) while the substrate is held at a positive potential. While DC sputtering is routinely used to deposit metals on substrate, the accumulation of positive charge at the source material can initiate the discharge of sputtering atoms arcing towards the anode if the target material is an insulator. To avoid this, insulators are usually deposited by RF sputtering process. In RF sputtering, radio-frequency voltage is applied between the target and substrate reduce the charge built up on the target materials. Also, it is one of the most employed method to sputter off the non-metal atoms without overheating the target materials (Promros and Paosawatyanong (2010)). However, during RF sputtering, due to the generated trap of secondary electrons, the deposition rate is considerably reduced as compared to DC sputtering (Youssef *et al.* (2009), Nomoto *et al.* (2019)). Then, both the sputtering processes will not occur when the kinetic energy of the accelerated electrons is not enough to bombard the target material.

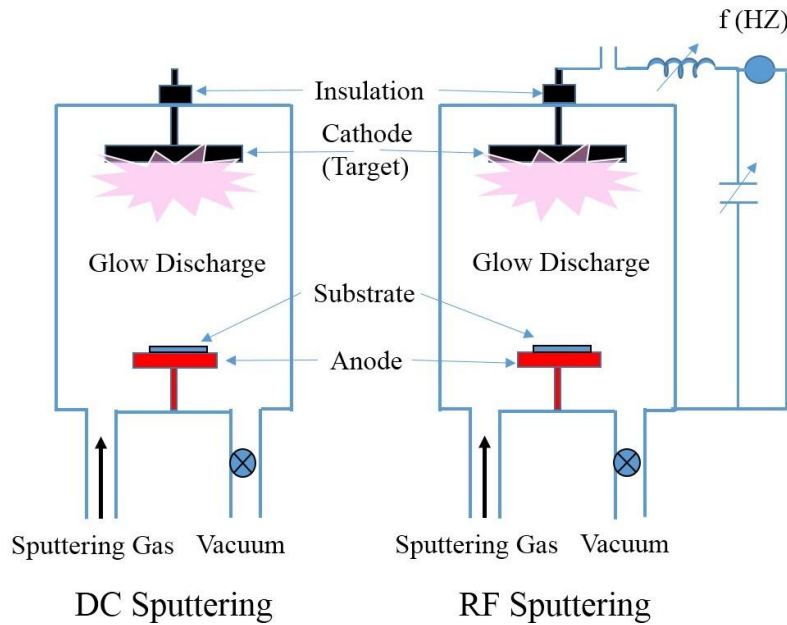


Figure 2.3: The schematic diagram of DC and RF magnetron sputtering systems.

2.4 Spin Coating

Spin coating is one of the most commonly used facile technique to prepare the organic and inorganic thin films with the desired thickness (nm to μm) over any suitable substrates (Hussein and Yazdani (2019)). In this process, a small drop of a solution containing the material to be deposited dissolved in a suitable solvent, is dispensed over a substrate held in place by a vacuum chuck. The substrate with the dispensed solution over it is allowed to spin at a high speed. The centripetal acceleration causes the liquid puddle to spread into a uniform thin film over the substrate. The thickness of the deposited film can be controlled by adjusting the rotation time and speed. After the deposition, the coated substrates are allowed to dry or heat (bake) to solidify the film as well as to remove the residual solvent. However, the coated film quality mainly depends on the chosen deposition parameters such as the nature of the liquid (drying rate, viscosity, and surface tension, etc.), deposition time, rotational speed and acceleration (Sadegh-cheri (2019)). The digital image and graphical representation of the spin coating unit were shown in **Fig. 2.4**.

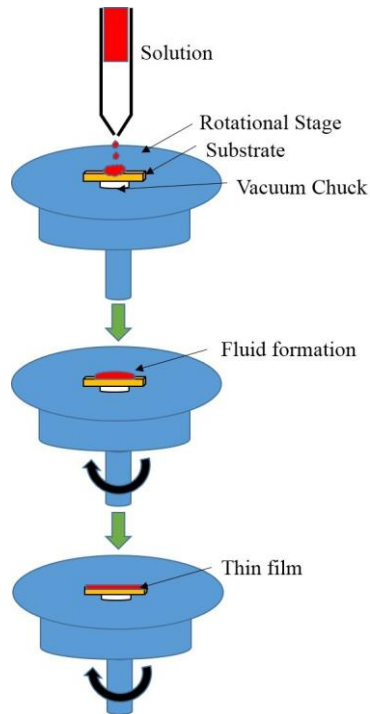


Figure 2.4: The schematic process of the spin coating method.

2.5 Preparation of Alloys

2.5.1 Thermal Molten Technique

In this work, the CZTS alloy was prepared from pure elements (99.999 %) of Cu, Zn, Sn and S. These were weighed in an atomic stoichiometry ratio of 2:1.5:1.2:4.4. The materials were then transferred and sealed under a vacuum on 1×10^{-5} Torr in cleaned quartz ampoules (10 mm diameter). Initially, the ampoule was heated up to 500 °C (5 °C/min) and maintained at that temperature for 1 hr in a furnace. The temperature of the furnace was then further increased to 950 °C. To ensure the homogeneity of the molten material, the ampoule was continuously rotated for 24 hrs, then it was gradually cooled down to room temperature (Sripan *et al.* (2017a)). After that, the sealed ampoule was broken and the target material was transferred to use as source material for evaporation.



Figure 2.5: (a) Evacuation unit. (b) Quartz ampoule (Inset shows the image of the ingot).

2.6 Solvothermal/Hydrothermal Method

In materials science and solid-state chemistry, a solvothermal or hydrothermal method is one of the most widely used technique in which, the synthesis process is carried out in autoclaves at elevated temperatures and pressure (Yang and Park (2019)). The process uses water as solvent (or catalyst) to synthesise a novel material with useful properties. Also, the high pressure provides an additional parameter to study the fundamental material property and crystal structure. In other words, this process involves a chemical reaction in a closed system which contains the reactants in solution form maintained at a temperature above the boiling point of water ($>100\text{ }^{\circ}\text{C}$) and a pressure of 1 atmosphere (atm) (Darr *et al.* (2017)). Moreover, this technique helps dissolution and effective recrystallization of those materials, which are relatively insoluble under normal conditions. It must be mentioned that yet there is no definite lower limit for temperature and pressure required for this process (Burungale *et al.* (2016)). Since the process may involve containing highly corrosive solvent at high temperature and pressure kept for longer durations, steel autoclaves along with inside inert liner material such as Teflon vessels ($100\text{ }^{\circ}\text{C}$ - $250\text{ }^{\circ}\text{C}$) are usually used to prevent the reaction with starting materials. A typical hydrothermal set up is shown in **Fig. 2.6**.

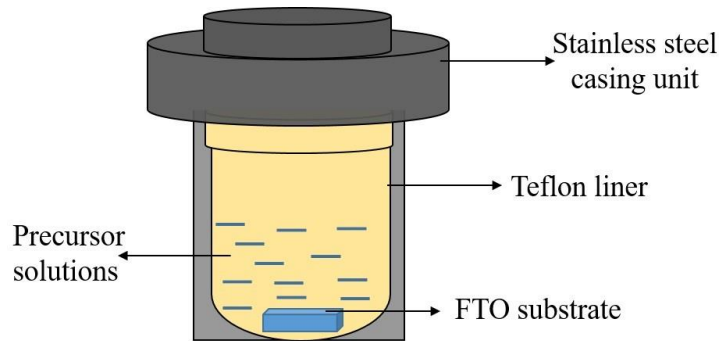


Figure 2.6: The schematic of Hydrothermal set up.

2.7 Hot Plate Method

In recent years, various research efforts have been devoted to grow 1D nanostructured (nanorod or nanotube) metal oxide semiconductors, owing to their unique properties such as large surface area, high porosity, light trapping property and high carrier mobility which attract their applications in photocatalysts, gas sensor, biosensor, biophotonics and solar cells (Tong *et al.* (2006), Li *et al.* (2007), Luo *et al.* (2010), İpeksaç *et al.* (2013), Manthina and Agrios (2016)).

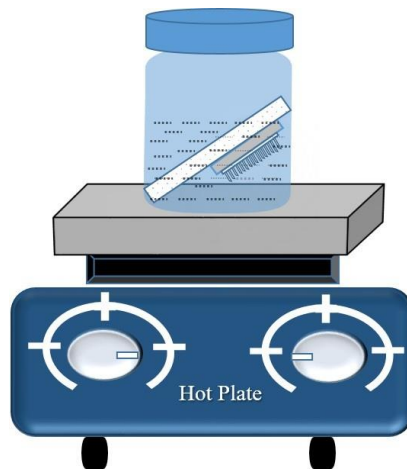


Figure 2.7: The schematic representation of hot plate technique.

Considering the broad range applications of nanotubes, so far they were successfully synthesized from template assisted, hot plate assisted electrodeposition, hydrothermal or solution processed techniques (Xu *et al.* (2007), Soomro *et al.* (2012), İpeksaç *et al.* (2013)). In general, hydrothermally grown nanotubes are synthesized by the two-step process (excluding seed layer deposition). To date, only a few reports are

available on the direct growth process of tubular structures via conventional hot air oven method by keeping either long reaction time or subsequently cooling down the reaction temperature from high to low or post-deposition aging route. In the present thesis, the formation of high aspect ratio and highly oriented ZNRs and ZNTs over seeded on FTO substrate using a single-step hot plate technique (**Fig. 2.7**) were demonstrated without employing any templates or catalysts.

2.8 Chemical Bath Deposition (CBD)

CBD is a facile solution processed technique to grow the chalcogenides and metal oxides thin films over the surface of an insoluble substrate, without the requirement of highly sophisticated equipment (Strano *et al.* (2014)). In the CBD technique, an anionic and cationic containing solution mixture helps to form the nuclei, when the ionic content exceeds or equal to the solubility product. Moreover, the CBD process relies on ionic concentration in the solution, which assists in producing the precipitated layer on top of the substrates. At the same time, the material loss should be avoided by controlling the unwanted bulk precipitate formation on the desired substrate. **Fig. 2.8.** shows the schematic of the experimental set up of CBD technique.

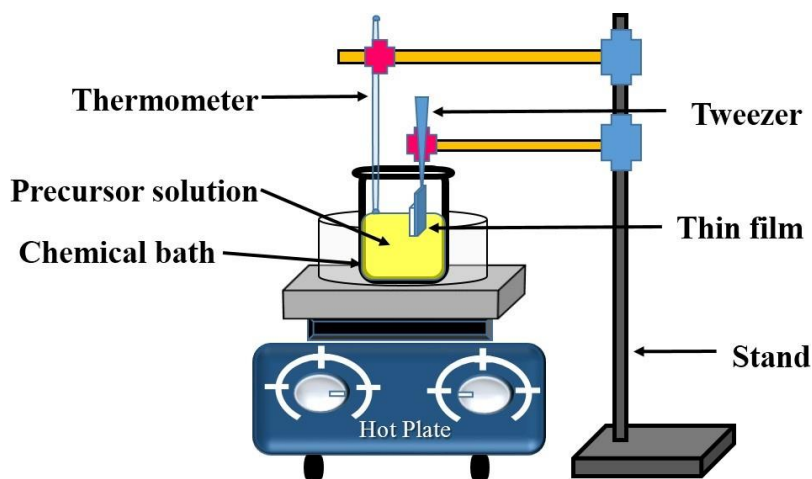


Figure 2.8: Schematic of the experimental set up of CBD technique.

2.9 X-ray Diffraction (XRD)

XRD is a powerful non-destructive characterization technique to study the crystal structure and interplanar spacing of crystalline samples. A highly energetic electrons are ejected from the heated filament and are accelerated towards the target materials by applying sufficient voltage (> 30 kV), the bombardment resultant produces the characteristic X-rays. The generated X-rays are filtered to produce monochromatic radiation, followed by it is collimated to direct and concentrate towards the sample to identify the crystallographic information. X-rays typically have wavelengths $\sim 1 \text{ \AA}$ which is on the order of atomic spacing in crystals and hence, diffract the same way as light from a diffraction grating. This makes it possible to characterize the crystal structure and hence crystalline phases, preferred crystalline orientations (texture), average crystallite size, strain, crystal defects and dislocations in detail (Bunaciu *et al.* (2015)). The diffraction pattern consists of a series of sharp peaks positioned at specific “Bragg” angles. The individual intensities of the diffraction peaks depend on the atomic distribution within the lattice while their position is determined by the Bragg angle in Bragg’s equation,

$$n\lambda = 2d_{(hkl)}\sin\theta \quad (2.1)$$

where, θ is the permitted angles of reflection (called as Bragg angle), λ is the wavelength of the X-ray radiation, d is interplanar spacing between the atomic planes and n is an integer. **Fig. 2.9.** and **Fig. 2.10** respectively show the schematic diagram and an images of XRD equipment used in this work.

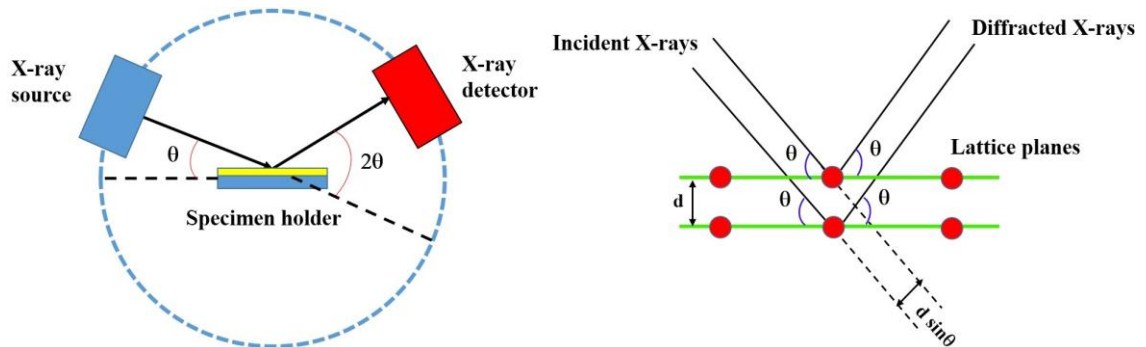


Figure 2.9: Schematic of (a) XRD setup, (b) Reflection of X-rays by two adjacent atomic planes.



Figure 2.10: XRD equipment used in this work.

2.10 Field Emission Scanning Electron Microscopy (FESEM)

FESEM is one of the several electron microscopy techniques. In this technique, a beam of electrons is emitted from the electron gun located at the top of the microscope. The entire setup is maintained under high vacuum. The electron beam then enters into the electron column where it travels in a vertical but helical path. While travelling, it passes two major electromagnetic lenses such as condenser to form the beam, and the objective lens to focus the beam. The focussed electron beam is rastered across the specimen surface to produce elastically and inelastically scattered electrons along with photons (shown in **Fig. 2.11**) (Akhtar *et al.* (2018)). These secondary electrons reach the detectors which generate signals produce surface sensitive, atomic contrast images as well as contain information about the elemental composition. This thesis FESEM images was performed using Carl Zeiss Ultra 55 FESEM equipment (image shown in **Fig. 2.12**).

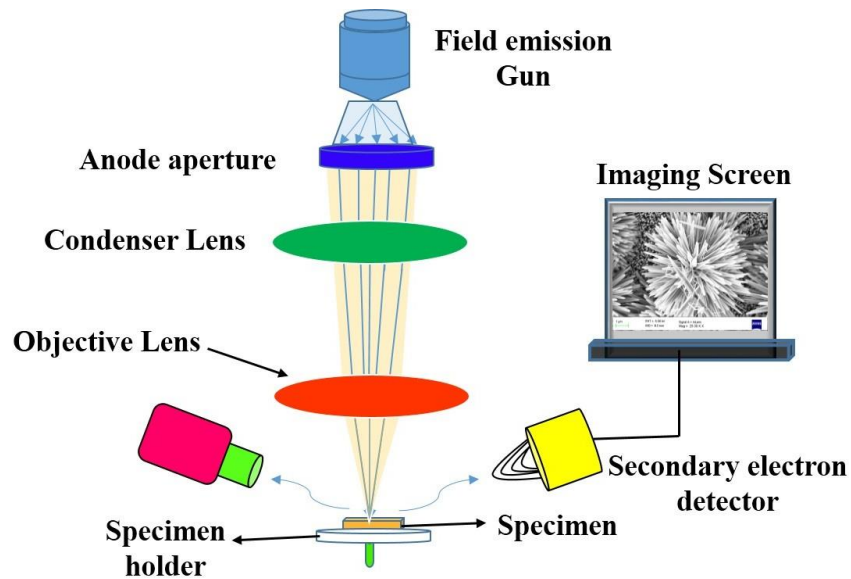


Figure 2.11: The schematic diagram of SEM analysis.



Figure 2.12: Carl Zeiss Ultra 55 FESEM used in this work.

2.11 Raman Spectroscopy

Raman spectroscopy is a characterization technique that identifies the vibrational and rotational modes of molecules in a given specimen by inelastic light scattering. The specimen is irradiated with a monochromatic laser beam with a wavelength ranging from UV-Vis to near IR (285 nm, 532 nm, 765 nm, and 825 nm). Photons from the

laser incident on the molecule allow it to excite from the ground state (vibrational state) to a virtual state. After some time, the excited molecule drops back to the different vibrational states with change in their frequencies (Bumbrah and Sharma (2016)). If the frequency of the scattered light is same as incident, the phenomena is called Raleigh scattering and if not, it is called Raman scattering.

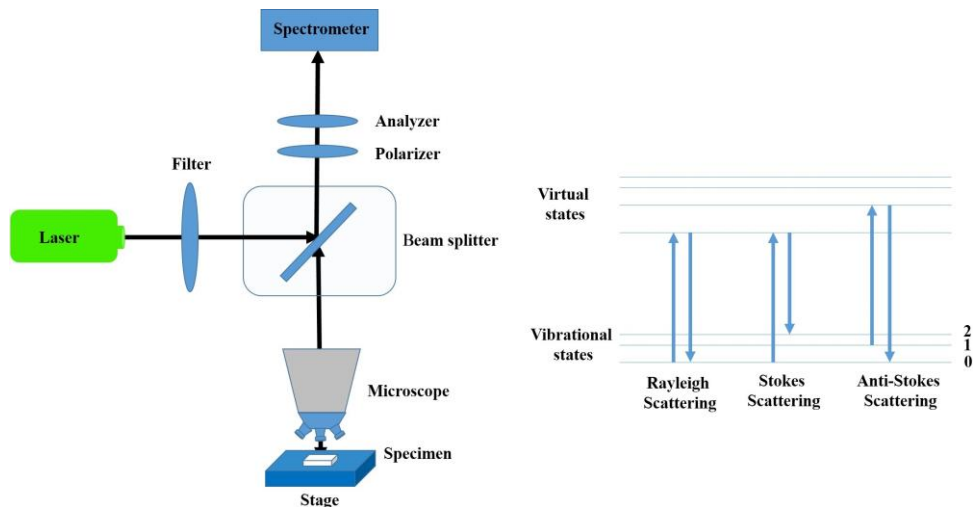


Figure 2.13: The schematic representation of Raman effect and instrumentation.

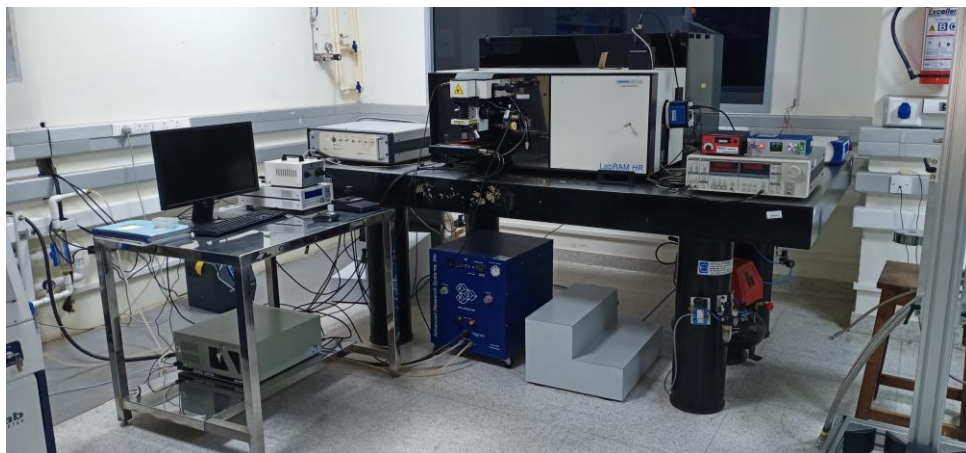


Figure 2.14: Raman Spectrometer employed in this work.

Raman spectrum of a given specimen involves a set of frequencies that lie above and below the excitation frequency. The range of frequencies lying below the excitation frequency are called as Stokes lines, and the ones lying above the excitation frequency as anti-Stokes lines (see **Fig. 2.13**). Most importantly, the change in the frequency

due to the coupling of incident light with vibrational-rotational states of the molecules carries information about the chemical bonds in the molecules. However, the intensity of the Stokes scattering is always higher than anti-Stokes. Also, the possible Raman modes generally depend on the symmetry of the specimen under investigation. In this thesis, Raman scattering experiments were recorded using Horiba LabRamHR equipment (**Fig. 2.14**).

2.12 Energy Dispersive Spectroscopy (EDS)

EDS is an analytical technique used to analyse the chemical composition of a given specimen. A beam of high energy electrons interacts with matter (specimen) to produce various inelastic scattered signals. In the specimen, an ejected inner shell electron creates a vacancy which is eventually filled by a higher energy electron from the outer shell and their energy difference releases an X-ray signal as shown in (**Fig. 2.15**). The energy of characteristic X-rays mainly depends on the difference in the energy levels of the emitted electron and that of the electron that jumps from an outer shell.

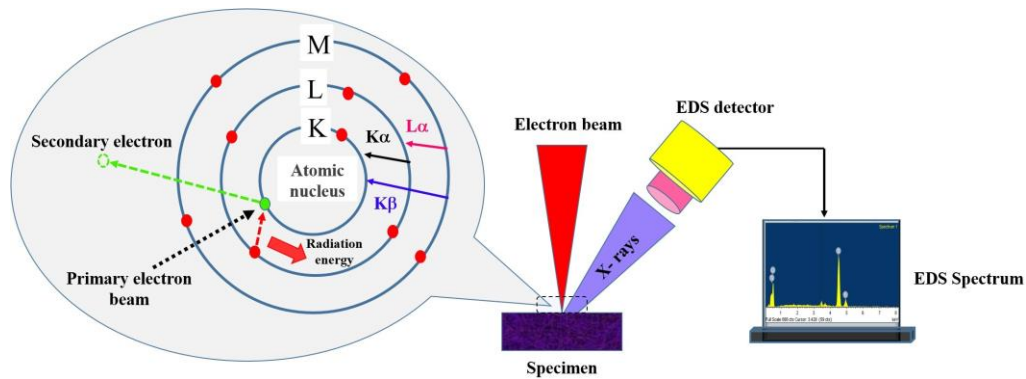


Figure 2.15: The schematic diagram of the EDS analysis.

The interaction volume and the energy of the emitted X-ray mainly depends on

- applied accelerating voltage (maximum 30 kV)
- atomic number of the atoms in the samples. The stimulated emission of these X-rays can be measured by an energy dispersive X-ray spectrometer. The intensity ratios of emitted X-ray energies of different atomic numbered elements give the elemental composition of the specimen. The detection li-

imits of this technique starts from Boron (B) to Uranium (U) and up to 1 atomic percentage can be quantified.

The EDS measurements of the fabricated thin films were performed using Oxford instruments 50 mm² detector and was an attachment with the Ultra 55 FESEM equipment (digital image shown in **Fig. 2.12**).

2.13 Cathodoluminescence (CL)

As mentioned in the earlier sections, interaction of highly energetic electron beam with the specimen results in generation of secondary electrons, backscattered electrons, characteristics X-rays and cathodoluminescence (CL). The term CL is used to describe the emission of low energy photons (~ 0.5 eV to 6 eV) in different materials such as semiconductors, ceramics, phosphors, geological minerals, organic compounds and few metals (plasmonic emission). The CL is one of the powerful characterization techniques which in general is coupled with SEM or scanning transmission electron microscope (STEM). Typically, the CL emission is governed by the electron beam spot size, interaction volume and lateral signal generations (Gustafsson and Kapon (1998)). In other words, the CL signal generations are dependent upon on the sample thickness, the applied accelerating voltage, beam current and spot size. The CL measurements (300 nm to 1000 nm) were recorded using the Gatan MonoCL4 detector attached with Ultra 55 FESEM equipment (schematic and digital images shown in **Fig. 2.16** and **Fig. 2.17**).

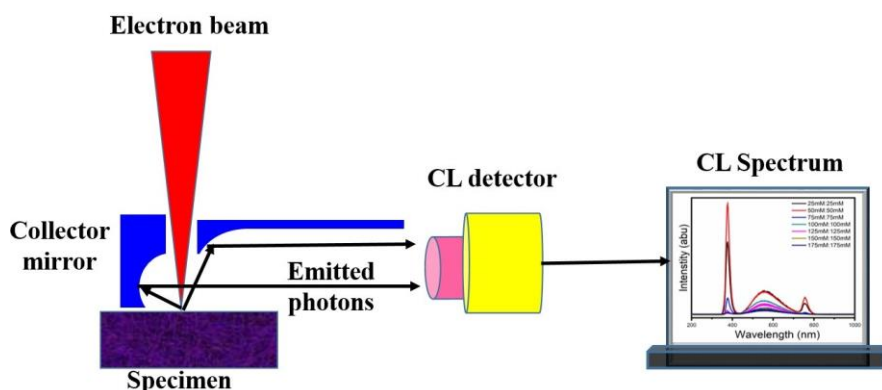


Figure 2.16: The schematic diagram of CL measurement.



Figure 2.17: FESEM with CL detector.

2.14 Ultraviolet-Visible (UV-Vis) Spectroscopy

This technique measures the reflection, transmission and absorption properties of the specimens (liquids, gases, bulk, and thin films). When monochromatic light is passed through a sample, it absorbs the required energy from the incident electromagnetic radiation (UV-300 nm to 400 nm, Visible-400 nm to 765 nm and NIR-765 nm to 3200 nm) to promote the electrons into the excited (or next energy) state. After a certain time, the excited state electrons relax down to ground state (Howell and Sutton (1998)). The intensity of the absorbed or emitted electromagnetic radiation at a given wavelength is recorded. UV-Vis spectroscopy obeys Beer-Lambert law given by,

$$A = \epsilon bc \quad (2.2)$$

where A is the absorbance, c is the concentration, b is the optical path length travelled in the given medium and ϵ is the molar absorption coefficient of the medium under study.

The optical band gap of the deposited films were calculated from the measured reflectance spectrum using Kubelka-Munk relationship (according to eq. 2.3).

$$F(R) = K/S = (1-R)^2/2R \quad (2.3)$$

$$(K \cdot h\nu)^{1/2} = F(R)(h \cdot \nu) \quad (2.4)$$

where K is reflectance transformed according to Kubelka Munk, S is scattering, R is reflectancy (%), h is Planck's constant, ν is frequency of the light and F is Kubelka Munk function.

In general, UV-Vis spectrometer contains deuterium arc lamp (for the UV region) and Xenon arc lamp (for the visible region). Light of a specific wavelength from a monochromator is split into two beams of equal intensity. One of the beam passes through the transparent sample (film coated substrate or solution in a cuvette) and other beam directed towards the transparent reference (bare substrate or solvent) cuvette. The transmitted light from the sample and the reference arms are processed by the direction

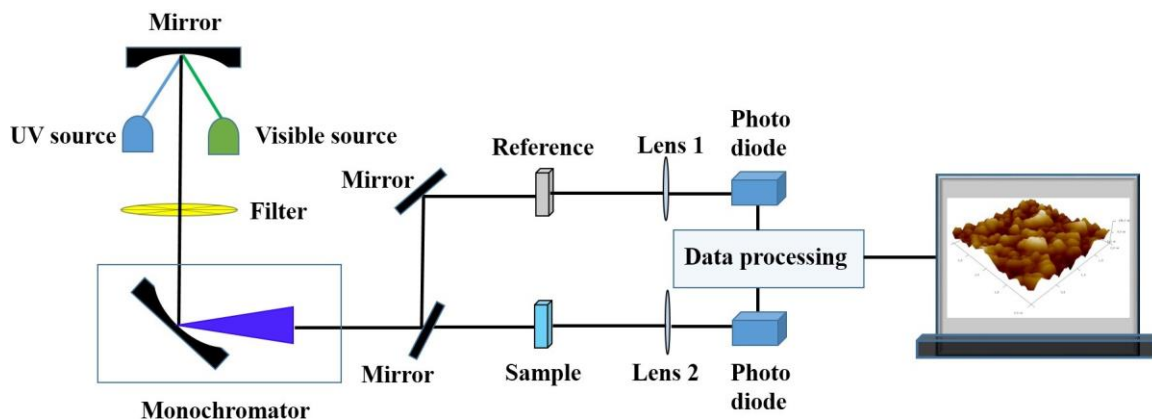


Figure 2.18: The schematic diagram of UV-Vis instrumentation set up.

system. Moreover, this method enables one to determine the optical (direct or indirect) bandgap and energy states of the semiconducting materials. The schematic of the UV-Vis spectrometer is depicted in **Fig. 2.18**. In this thesis, the UV-Vis spectrometer DRS measurements were performed on Shimadzu MPC3600 with integrating sphere and is shown in **Fig. 2.19**.



Figure 2.19: Shimadzu MPC3600 UV-Vis spectrometer.

2.15 X-ray Photoelectron Spectroscopy (XPS)

XPS is one of the most promising materials characterization technique based on the photoemission process and is extensively used to analyse the surface chemistry (~ 10 nm) such as composition (quantitative) and oxidation or chemical state (qualitative) of the specimen. In this technique, a monochromatic X-ray photon is absorbed by the core (inner) level electron of the surface atoms of the specimen, resulting in ionization of the atom. The energy of the emitted photoelectron carries information about the chemical state and composition of the surface layers (Korin *et al.* (2017)). However, due to the inelastic mean free path (escaping depth without losing its energy) of the emitted photoelectrons, this technique is restricted to collect the information only from the surface levels. Generally, a twin or dual anode non-monochromatic source (0.9 eV FWHM) such as Mg $K\alpha$ (energy ($h\nu$) = 1253.3 eV) and Al $K\alpha$ ($h\nu$ = 1486.6 eV) and single anode Al $K\alpha$ ($h\nu$ = 1486.6 eV) monochromatic sources (0.4 eV FWHM) are used in XPS with a maximum 15 mA as emission current and 15 kV as the accelerating voltage. The number of ejected electrons can be measured using an appropriate electron energy analyzer to record the photoelectron spectrum under the 10^{-9} Torr vacuum. Moreover, the photo-ejected inelastically scattered electrons kinetic energy (KE) is calculated in terms of binding energy (BE),

$$BE = h\nu - KE - \Phi \quad (2.3)$$

where h is the Planck's constant, ν is the frequency and Φ is the equipment work function. The calculated BE helps to identify constituent elements in the sample, their valance state, the functional groups or chemical bond information in the sample (except Hydrogen and Helium). The detection limits of this technique starts from Lithium (Li) to Uranium (U) and up to 0.1 atomic percentage can be quantified.

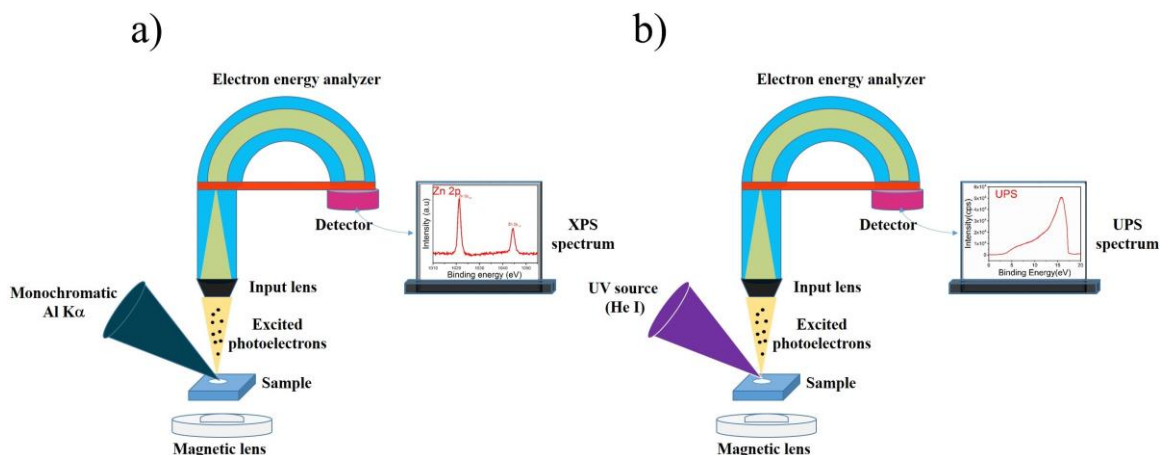


Figure 2.20: The schematic diagram of (a) XPS and (b) UPS analysis.

In contrast with XPS, in UPS a relatively low energy (ultra-violet) photon (He source 21.22 eV) interacts with the given sample and ejects the valence level electrons of the molecule or solid. This technique is extremely useful to study the work function (Φ) and valence band maxima (V_{bm}) of the specimen. Typically, XPS and UPS techniques together give the information about the chemical and electronic states of the sample (shown in **Fig. 2.20**). In this work, the XPS core level and valence band spectra such as wide or survey scans and high resolution or narrow scans were swept with the constant analyser pass energies of 160 eV and 20 eV respectively. Also, UPS with a pass energy of 10 eV was applied to record the spectra. The XPS and UPS measurements were performed on the fabricated specimens using Kratos Axis Ultra DLD equipment (shown in **Fig. 2.21**).



Figure 2.21: Kratos Axis Ultra DLD XPS and UPS equipment.

2.16 Transmission Electron Microscopy (TEM)

TEM is one of the most commonly used resourceful equipment to characterize the materials in terms of crystal structure, defects, elemental composition and morphology below nanometre scale (Guzzinati *et al.* (2018)). In this method, a beam of electrons accelerated with high energy (300 kV) pass through the electronically conducting ultra-thin specimen. The transmitted signals carry the information about the internal atomic structure and chemistry of the materials. TEM offers two primary image modes: the image formation with the direct beam called “bright field” (BF) and the image formation due to the diffracted beam called “dark filed” (DF). In other words, in bright field mode, image forms without any diffraction (aperture blocks the diffracted electrons) beam while in the dark field mode the image formation happens only with the diffracted beam (aperture blocks the direct beam) as shown in **Fig. 2.22**. The TEM measurements were performed using Titan THEMIS 300 kV from Thermofisher (**Fig. 2.23**).

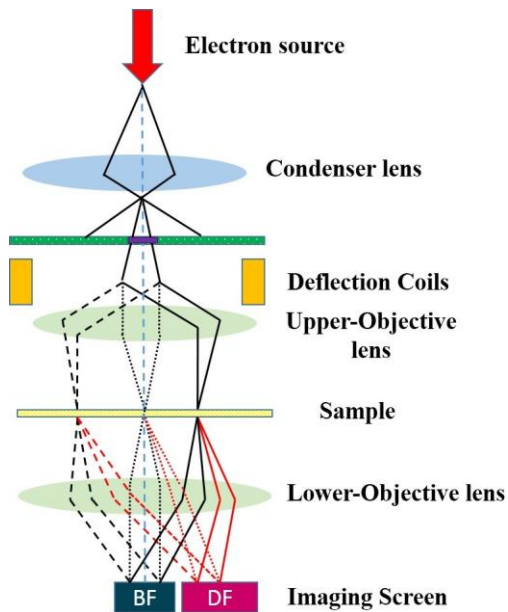


Figure 2.22: The schematic diagram of TEM.

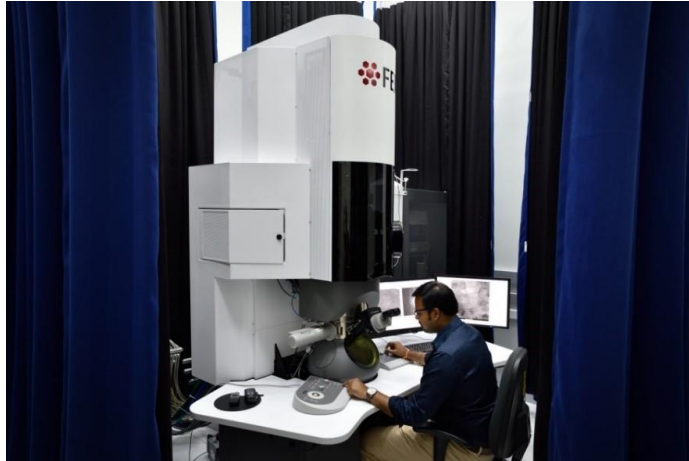


Figure 2.23: Titan THEMIS 300 kV from Thermofisher TEM equipment.

2.17 Atomic Force Microscopy (AFM)

A non-destructive mechanical microscope called AFM, is considered as one of the alternative techniques to investigate the topographical information of the materials on atomic scale resolution (Baykara and Schwarz (2017)). This technique uses a small sharp tip (nm range) which is mounted on top of a cantilever (with specific spring constants) to interact with the sample for imaging (**Fig. 2.24**). Initially, the cantilever is permitted to oscillate with its resonant frequency, before it approaches the specimen surface. In the meantime, beam from a laser diode is focused on the neck of the cantilever and its reflection simultaneously received by the position sensitive photodetector.

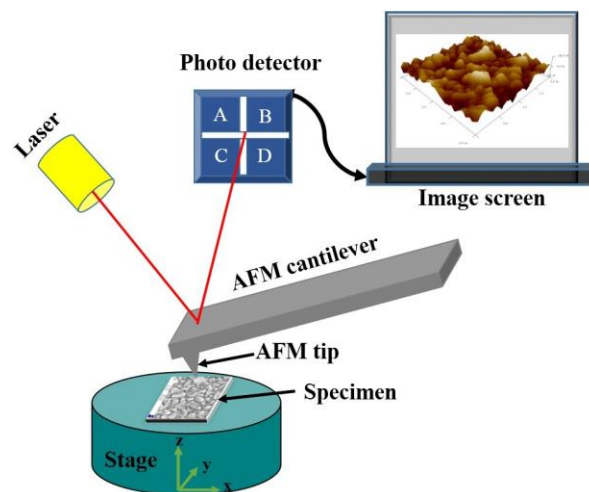


Figure 2.24: The schematic setup of AFM.

The AFM tip is allowed to undergo a raster scan over the surface of the sample by piezoelectric scanning unit. Once the tip comes closer to the sample surface, an attractive force deflects the cantilever towards the sample and when the tip is brought into contact with the specimen, repulsive force deflects the cantilever away from the sample. The displacement position of the cantilever (vertical and lateral) with respect to the sample surface is recorded by a closed loop photodetector system whose output is processed to generate the topographical AFM image. The AFM images with the scanning ranges of $5\ \mu\text{m} \times 5\ \mu\text{m}$ were recorded from BrukerDimension ICON ScanAsyst AFM in this thesis (shown in **Fig. 2.25**).



Figure 2.25: Bruker Dimension ICON ScanAsyst AFM.

2.18 Solar Simulator

The solar simulator is a source of artificial solar spectrum which closely approximates, natural sunlight in terms of its intensity and spectral composition and is used to test the solar PV cells (Wang *et al.* (2005)). This technique is widely accepted as an alternative facility to characterize the fabricated solar devices in indoor laboratory conditions. It consists of three major components such as light sources (Xenon arc lamp, metal halide arc lamp, quartz tungsten halogen lamp and LEDs) with power supply, optics and filters to achieve the required intensity of the output beam and essential controls to operate the simulator (spectral selection, spatial uniformity, and temporal stability (**Fig. 2.26**)). In this thesis, the fabricated PV devices were studied using Newport Sol3A class AAA equipment (see **Fig. 2.27**).

Solar simulator

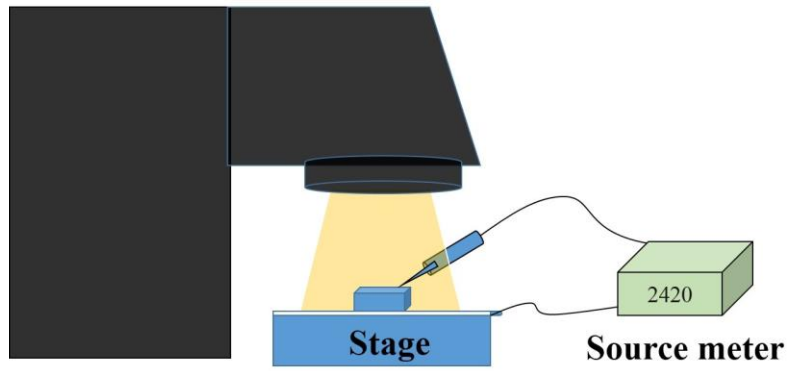


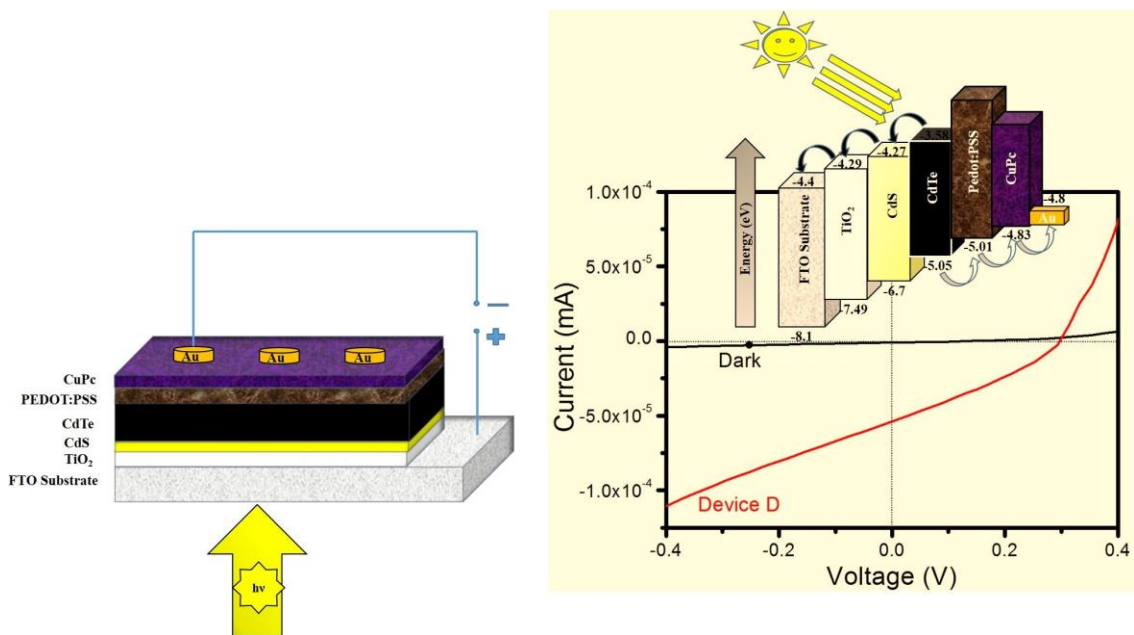
Figure 2.26: The schematic set up of Solar simulator.



Figure 2.27: Newport Sol3A class AAA solar simulator.

Chapter 3

Effect of CuPc and PEDOT:PSS as Hole Transport Layers in Planar Heterojunction CdS/CdTe Solar Cell



3.1 Introduction

In recent years, cadmium based binary (II-VI) chalcogenide materials such as CdTe has widely recognized as an alternative candidate for making PV devices. Besides, the direct bandgap (1.45 eV at 300K) and higher optical absorbance coefficient ($\alpha > 10^4 \text{ cm}^{-1}$) make it an ideal material for fabricating highly efficient solar cells (Razykov *et al.* (2012), Mitchell *et al.* (1977)). The conventional superstrate structured CdTe thin film solar cells are constructed with i) transparent conducting oxide (TCO) layered substrate as a front electrode, ii) commonly employed heterojunction partner n-type CdS as a buffer layer, iii) p-type CdTe as an absorbing layer and iv) metal over the CdTe layer as the bottom electrode. At the interface of thin CdS/CdTe, CdTe and CdS are miscible and form a highly intermixed layer ($\text{CdS}_{1-x}\text{Te}_x$), which helps reduce the interfacial defect density (Ferekides *et al.* (2000)). According to the Shockley-Queisser limit, theoretically calculated PCE of CdS/CdTe heterojunction thin film solar cell is higher than 33 %. However, experimentally proven world record efficiency on the lab-scale was 22.1 % (Polman *et al.* (2016), Green (2017)). Typically, to absorb the maximum range of solar energy spectrum, a high efficiency CdS/CdTe solar cell uses $>2 \mu\text{m}$ thick absorbing layer. On the other hand, if CdTe layer thickness approaches a certain limit ($>1 \mu\text{m}$) the performance of solar cells decreases due to the incomplete absorption, local shunting and carrier diffusion (Bai *et al.* (2011)).

Z. Fang *et al.* reported that the Schottky barrier limits the hole transport at CdTe/metal junction, which in turn decreases the device FF (Fang *et al.* (2011)). The CdTe solar cells have been already commercialized and available in large scale production, but still, research lies in finding a suitable back contact and designing the novel device architecture (Khrypunov *et al.* (2010)). Several researchers have demonstrated the enhancement of PCE in CdTe solar cells by introducing different front and back contact (charge transport electron/hole) layers (Potlog *et al.* (2011), Khurram *et al.* (2017), Britt and Ferekides (1993), Jarkov *et al.* (2011), Ye *et al.* (2011)). The main reason for introducing these electron and hole transporting layers is to enhance the carrier collection and transportation towards the bottom and top electrodes. To provide a suitable driving force to transfer the photogenerated charge carriers effectively, conduction band (CB) of the absorbing layer should be significantly higher than CB of the ETL and as well as the valence band (VB) of absorbing layer should be lower than that of the hole transport layer HTL (Lattante (2014)).

To date, CdTe solar cells have been extensively studied with different ETLs such as CdS, ZnS, ZnSe, TiO₂ (Britt and Ferekides (1993), Karaagac *et al.* (2013), Liu *et al.* (2015)). Mutalikdesai *et al.* have reported that the addition of the TiO₂ window layer inserted between the FTO substrate and the CdS layer helps to reduce the device leakage current in CdS/CdTe heterojunction thin film solar cell (Mutalikdesai and Ramasesha (2017)). Also E. Hernandez *et al.* has reported that the sputtered TiO₂ thin film (15 nm) can be used as a high resistance buffer layer to achieve higher conversion efficiency (12 %) in CdS/CdTe solar cells (Hernández-Rodríguez *et al.* (2016)). On the other hand, to avoid the Schottky or to form ohmic contact in CdTe solar cells, inorganic MoO₃, organic SPIRO OMeTAD, PEDOT:PSS and P3HT have been comprehensively studied as HTL (Khrypunov *et al.* (2010), Jarkov *et al.* (2011), Ye *et al.* (2011), Major *et al.* (2017)). Among them, PEDOT:PSS has the potential advantage of having high WF which helps to reduce the barrier height and also prevents the metal diffusion into the absorbing CdTe layer (Liu *et al.* (2015)). Moreover, the lower interfacial defects at the inorganic/polymer interface facilitates the decrease in charge carrier trapping and recombination in the device (Wang *et al.* (2016b)).

G. Khrypunov *et al.* reported that the metal interface with CdTe leads to a Schottky barrier (back diode behavior) instead of ohmic contact due to the high WF of CdTe. To overcome that issue, several research attempts have been made on high electrical conductivity polymer PEDOT:PSS as back contact in CdTe solar cells (Khrypunov *et al.* (2010), Jarkov *et al.* (2011), Ye *et al.* (2011)). However, the architecture on FTO/TiO₂/CdS/CdTe heterojunction along with two hole transport layers (back contacts) have not been extensively studied in CdS/CdTe based solar cells.

3.1.1 Objectives of the Work

The main objectives of the present chapter is, to fabricate and characterize the new architecture based planar heterojunction superstrate CdS/CdTe thin film solar cells (shown in **Fig. 3.1**), employed with two HTLs (PEDOT:PSS as HTL1 and CuPc as HTL2). Then to study the effect of two hole transporting layers along with TiO₂ as window layer and CdS as buffer layer in CdTe planar heterojunction PV devices. Further to understand the band alignment and charge carrier transport mechanism of electron and hole transporting layers in planar hetero-interface CdTe device architecture.

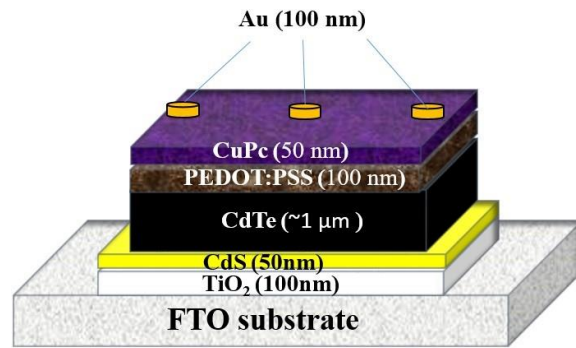


Figure 3.1: The schematic diagram of the novel CdS/CdTe planar heterojunction solar cell.

3.2 Experimental Details

3.2.1 Fabrication of Planar Heterojunction CdS/CdTe Solar Cells.

- Initially, the FTO substrates were cleaned by ultra-sonication with 1:1:1 ratio of acetone, 2-propanol, and de-ionized (DI) water for 15 min, after that it was dried under N₂ gas before further use (**Fig. 3.2**).

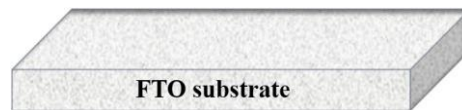


Figure 3.2: Cleaned FTO substrate.

- The window layer TiO₂ (100nm) thin film was deposited on top of the FTO coated glass substrate (resistivity 7 Ω/square) using RF magnetron sputtering technique. Then the coated substrates were air annealed in a furnace at 450 °C for 30 min (**Fig. 3.3**).
- The buffer layer of CdS (50 nm) thin film was deposited on top of the TiO₂/FTO substrate using the RF magnetron sputtering method. Then the coated substrates were annealed at 350 °C for 5 min under N₂ atmosphere (**Fig. 3.4**).

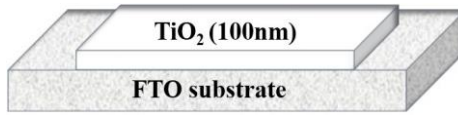


Figure 3.3: TiO₂ window layer (100 nm) coated FTO substrate.

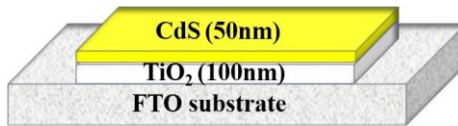


Figure 3.4: CdS buffer layer (50 nm) coated on the TiO₂/FTO substrate.

- On top of the CdS/TiO₂/FTO film $\sim 1 \mu\text{m}$ thick absorbing layer of CdTe was deposited by a thermal evaporation method. The coated CdTe/CdS/TiO₂/FTO films were annealed at 450 °C for 20 min in the N₂ atmosphere for improving the crystallinity and junction formation (**Fig. 3.5**).

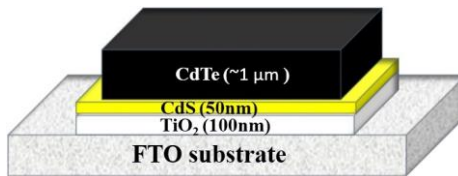


Figure 3.5: CZTS layer (1 μm) deposited over the CdS/TiO₂/FTO substrate.

- The HTL1 PEDOT:PSS (100 nm) was spin-coated at 3000 rpm under room temperature and then the film was air baked at 100 °C for 20 mins (**Fig. 3.6**). The HTL2 CuPc (50 nm) and 100 nm top electrode Au was deposited by thermal evaporation method (**Fig. 3.7**).

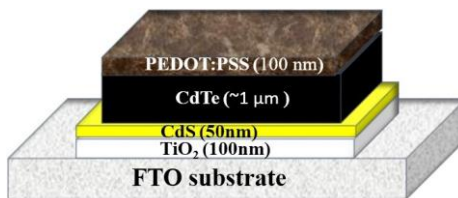


Figure 3.6: PEDOT:PSS (100 nm) spin-coated over CdTe/CdS/TiO₂/FTO substrate.

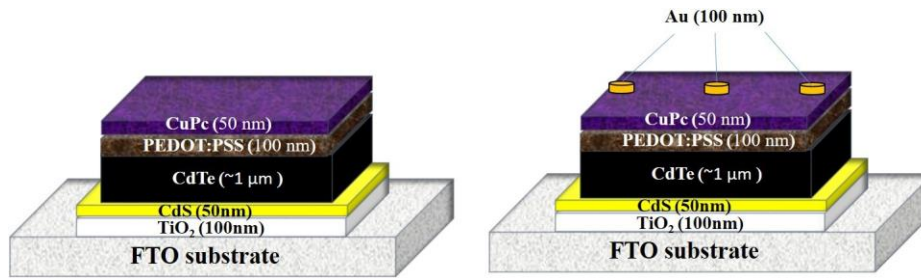


Figure 3.7: Au (100 nm) and CuPc (50 nm) deposited on top of PEDOT:PSS/CdTe/CdS/TiO₂/FTO substrate.

3.2.2 Characterization of the Deposited Films

The surface morphology and topographical information of the fabricated films were studied using a high-resolution FESEM and tapping mode AFM with the scanning area of $2 \mu\text{m} \times 2 \mu\text{m}$. The crystallographic analysis of deposited TiO₂, CdS, CdTe films were performed using grazing incidence X-ray diffractometer (GI-XRD) with the diffraction angle ranges from 20° to 70° using Cu K α source ($\lambda = 1.5405 \text{ \AA}$). The phase formation of the deposited films were investigated from Raman spectroscopy using the excitation wavelength of 532 nm. Chemical states of the deposited films were obtained by XPS under the condition of 13 mA emission current and 12 kV accelerating voltage (156 W). Before recording the XPS spectra of TiO₂, CdS and CdTe films were sputtered using Ar ion source (4 kV, area of $3 \times 3 \text{ mm}^2$) for removing the surface contaminations. The electronic structures (V_{bm} and WF) of deposited TiO₂, CdS, CdTe, PEDOT:PSS and CuPc films were characterized using UPS using He I source energy (21.22 eV). Finally, the current-voltage (I-V) performances of the devices were measured using a solar simulator under AM 1.5G.

3.3 Results and Discussion

3.3.1 X-ray Diffraction Studies of the Deposited Thin Films

The GI-XRD technique was used to observe the crystallinity of annealed TiO₂, CdS, and CdTe thin films. The GI-XRD geometry is particularly useful for thin films, wherein there is a significant increase in the path length of the beam into the layer, leading to better signal-to-noise ratio. **Fig. 3.8(a)** represents the relative intensity peaks of TiO₂ film presented at the diffraction angles of 25.3° , 37.9° , 48.2° , 54.1° , 55.1° and

61.9° which correspond to the orientations of (101), (004), (200), (105), (211) and (213) respectively (JCPDS:84-1285) (Matos *et al.* (2015)).

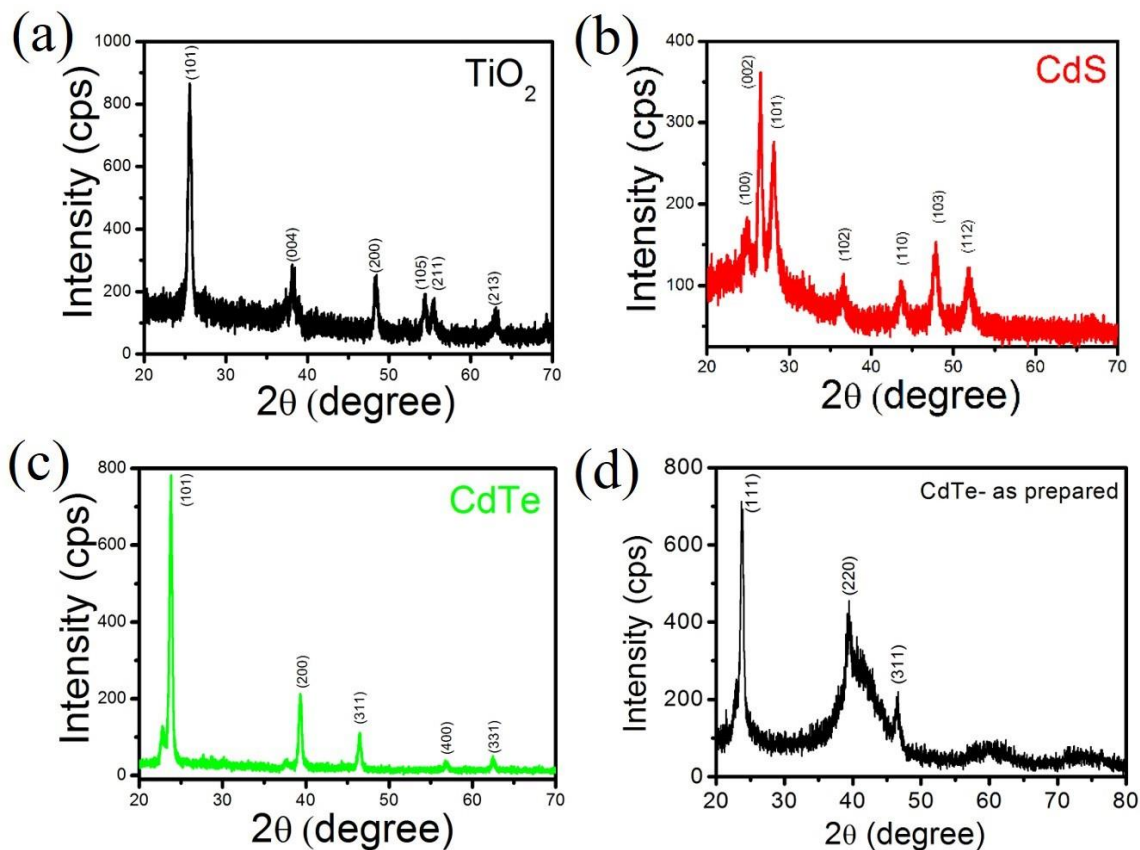


Figure 3.8: XRD patterns of annealed thin films (a) TiO₂ at 450 °C, (b) CdS at 350 °C, (c) as-prepared CdTe, (d) CdTe at 450 °C.

It reveals that the TiO₂ thin films were in dominant anatase polycrystalline structure without any impurity. The planes of CdS thin film (**Fig. 3.8(b)**) were oriented at (100), (002), (101), (102), (110), (103) and (112) which correspond to the diffraction angles of 25.0°, 26.6°, 28.3°, 36.6°, 43.6°, 47.8° and 51.8°. The calculation indicates that the deposited CdS film was in standard hexagonal wurtzite structure (JCPDS: 41-1049). The CdTe diffraction pattern (**Fig. 3.8(c)**) displays five crystalline peaks at 2θ values of 23.7°, 39.5°, 47.2° and 63.1° which correspond to the diffraction produced by the (111), (220), (311), (400) and (331) planes. This indicates the preferential crystallographic growth of CdTe, respectively. The annealed CdTe film showed an increased diffraction intensity, due to the improved crystallinity compared to the as-prepared thin films (**Fig. 3.8(d)**). The intense peak values of annealed CdTe thin film were in good

agreement with a cubic zinc blende structure (JCPDS:15-0770) (Shenouda and El Sayed (2015)).

3.3.2 Raman Spectroscopy Analysis of TiO₂, CdS, and CdTe Thin Films

The Raman vibrational spectra of TiO₂, CdS, and CdTe thin films is shown in **Fig. 3.9** which reveals that the crystal phases were well separated in frequency and thus offer accurate information about the presence of different crystal phases in the films. In general, the anatase phase of TiO₂ has six Raman active modes: $A_{1g} + 2B_{1g} + 3E_g$. **Fig. 3.9(a)** shows the Raman spectrum of the TiO₂ thin film, the peaks were located at 145 cm⁻¹, 398 cm⁻¹, 519 cm⁻¹, and 640 cm⁻¹ confirming the anatase phase of TiO₂. The prominently intense E_g (low-frequency) mode at 145 cm⁻¹ and 640 cm⁻¹, the bending vibrations of O-Ti-O peaks at 398 cm⁻¹ and 519 cm⁻¹ correspond to the B_{1g} mode of anatase TiO₂ (Zhang *et al.* (2000)).

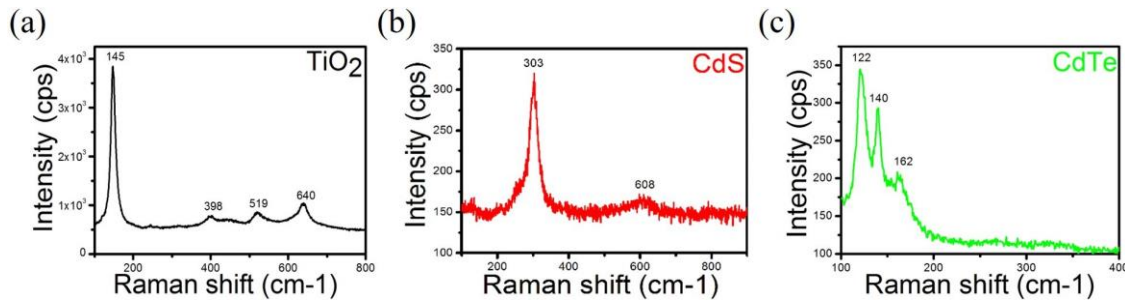


Figure 3.9: Raman spectra of (a) TiO₂ at 450 °C, (b) CdS at 350 °C, (c) CdTe at 450°C.

The peaks at 303 cm⁻¹ and 608 cm⁻¹ correspond to the fundamental optical phonon Longitudinal modes (LO) and the first overtone mode (2LO) of the annealed CdS film (see **Fig. 3.9(b)**) (Senthil *et al.* (2001)). The position rules for transverse (TO), LO and A₁ (Te) optical phonon modes of CdTe films were found to be at 140 cm⁻¹, 162 cm⁻¹ and 122 cm⁻¹ (**Fig. 3.9(c)**) respectively (Ma *et al.* (2015)). The phase identification studies carried out on TiO₂, CdS and CdTe films using Raman spectroscopy stand in good agreement with the XRD results.

3.3.3 X-ray Photoelectron Spectroscopy Analysis of TiO₂, CdS, and CdTe Thin Films

Fig. 3.10 shows the oxidation state of surface etched XPS spectra of TiO₂, CdS, and CdTe thin films. The Ti 2p_{3/2} and Ti 2p_{1/2} peaks of TiO₂ films were observed at the binding energies of 458.5 eV and 464.3 eV (**Fig. 3.10(a)**) respectively, which confirms the deposited films were in TiO₂ chemical state (Chu *et al.* (2012)).

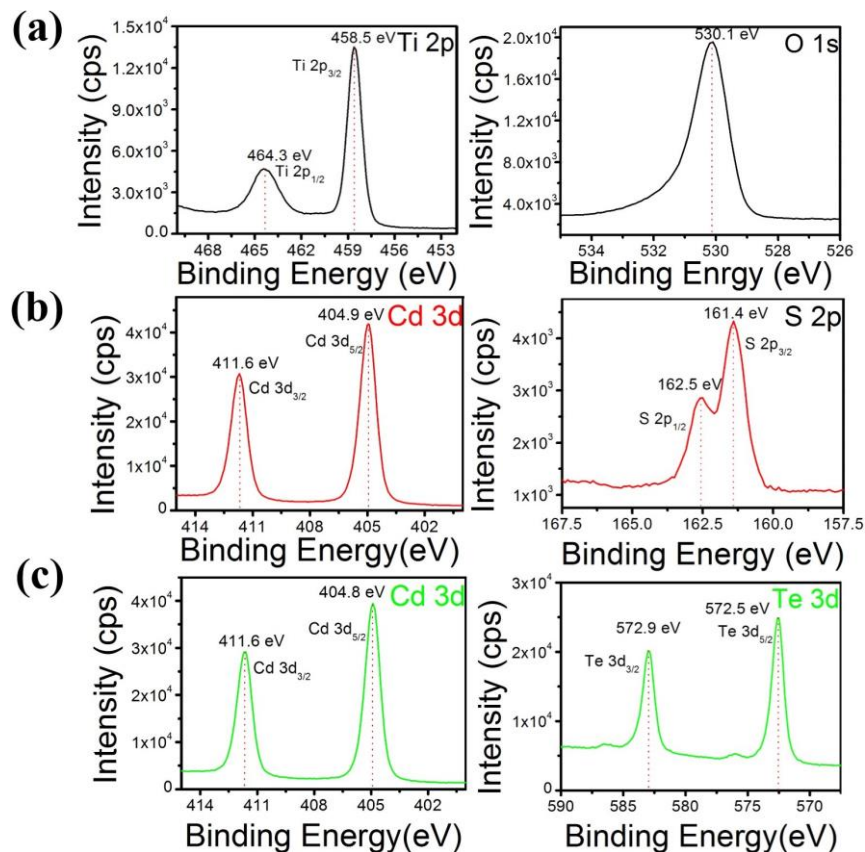


Figure 3.10: XPS spectra of annealed (a) TiO₂, (b) CdS, (c) CdTe thin films.

The peaks located at binding energies of 404.9 eV and 411.6 eV (**Fig. 3.10(b)**) were attributed to CdS thin film, which is consistent with the Cd²⁺ state. The S 2p core-level spectrum of CdS centered at 161.4 eV and 162.5 eV corresponded to the S 2p_{3/2} and S 2p_{1/2} of S²⁻ states respectively (Bhandari *et al.* (2014)). The peaks at the binding energies of 404.8 eV and 411.6 eV were related to Cd 3d_{5/2} and Cd 3d_{3/2} emissions of CdTe respectively. **Fig. 3.10(c)** shows the Te 3d region of the same XPS spectrum where observed peaks at the binding energies of 572.5 eV and 582.9 eV were related to Te 3d_{5/2}

and Te 3d_{3/2} (Jun-Feng *et al.* (2015)). The chemical states of all prepared films were well correlated with XRD and Raman studies. The O 1s spectra of spin-coated HTL1 PEDOT:PSS film has two major peaks located at 531.8 eV and 533.2 eV which were assigned to S=O and O–H bonds respectively (**Fig. 3.11(a-f)**).

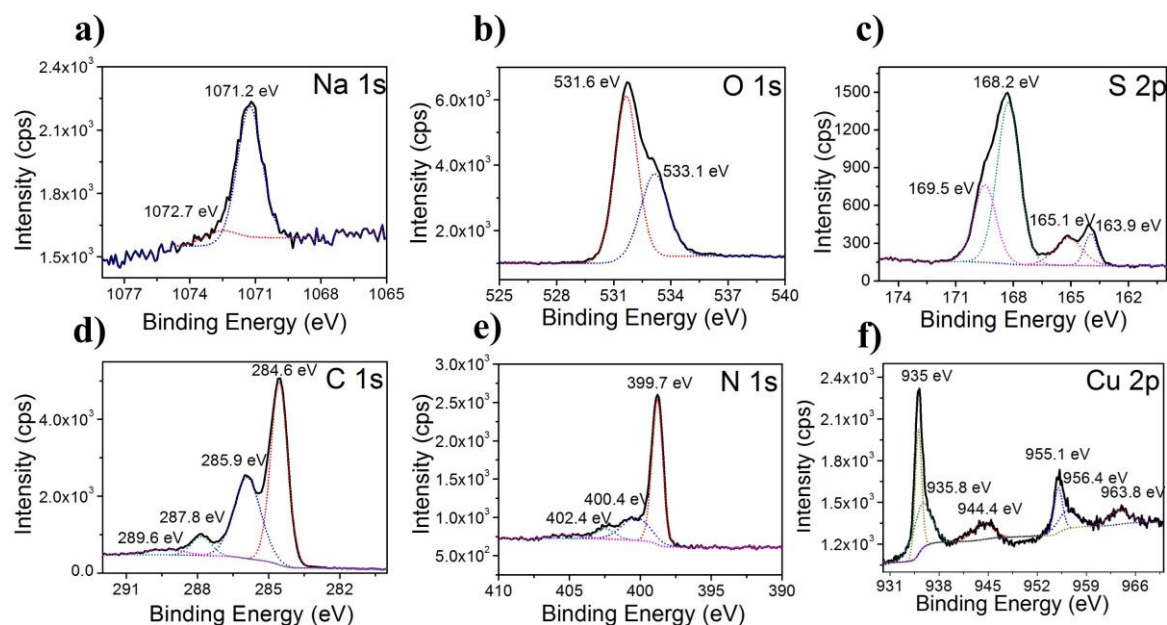


Figure 3.11: XPS spectra of (a-c) PEDOT:PSS, (d-f) CuPc.

Moreover, the O-H bond of PEDOT and PSS chains help to minimize the surface oxidation of CdTe at the interface, resulting in decrease device leakage current. Also, the presence of those bonds helped to enhance the hole transportation. The sulfur (S 2p) peaks from the PSS and PEDOT chains correspond to doublet at the binding energies of 169.5 eV and 165.1 eV, 168.2 eV, and 163.9 eV respectively (**Fig. 3.11(c)**) (Mahato (2017)). The high-resolution XPS spectrum of N 1s of HTL2 CuPc as shown in **Fig. 3.11(e)** comprises of the groups of nitrogen atoms in N-N, C-N and Cu-N bonding in the CuPc molecule. The corresponding electronic states of Cu 2p_{3/2} and 2p_{1/2} peaks were located at 935.2 eV and 955.1 eV respectively. The presence of Cu (II) state in CuPc molecule exhibits a ~ 9 eV binding energy (BE) difference between the major Cu peak and satellite peak at 944.4 eV (**Fig. 3.11(f)**) (Mali *et al.* (2012)).

3.3.4 Ultra-Violet Photoelectron Spectroscopy Analysis of the Fabricated Thin Films

The UPS spectra of TiO₂, CdS, CdTe, PEDOT:PSS and CuPc thin films were shown in **Fig. 3.12**. The surface WF (Φ) of the films was determined by the energy difference between the incident photon ($h\nu=21.22$ eV) and the mid-point of respective secondary onsets from the UPS spectrum. The measured BE of the TiO₂, CdS and CdTe films (from **Fig. 3.12**) were 17.12 eV, 17.46 eV, and 16.63 eV, which correspond to the WF of 4.1 eV, 3.76 eV and 4.59 eV respectively.

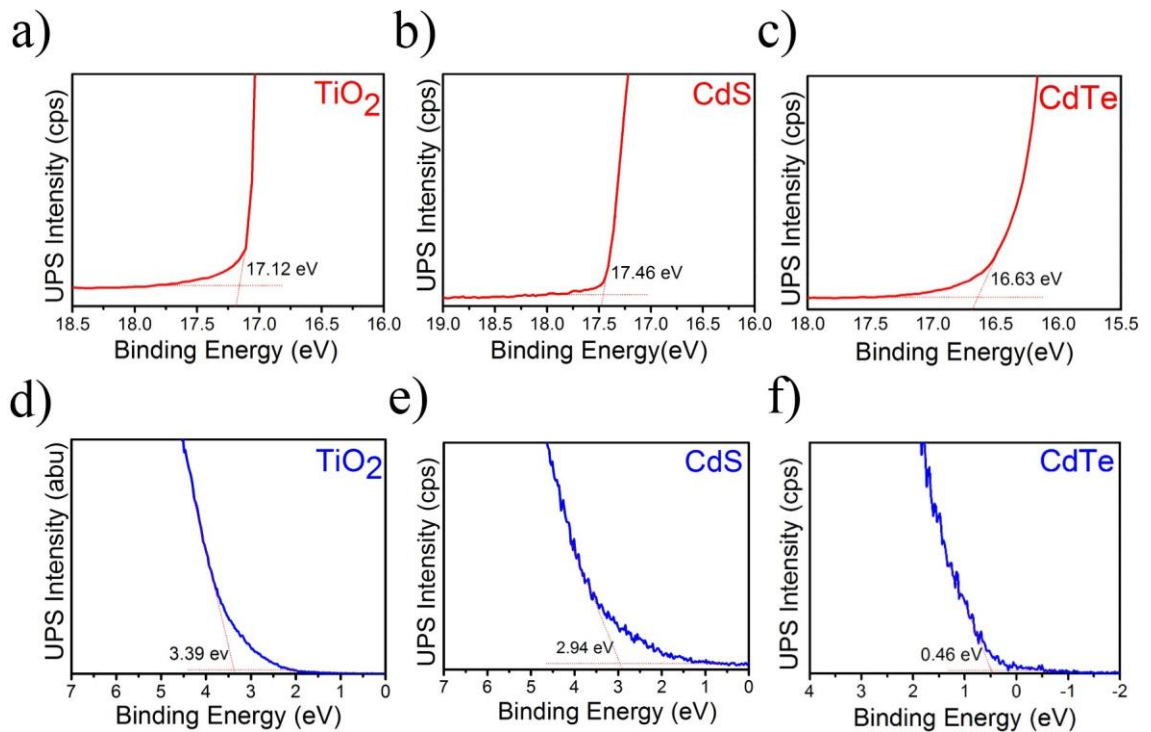


Figure 3.12: UPS spectra of annealed TiO₂, CdS, and CdTe thin films.

The V_{bm} was measured by linearly fitting the leading edge of the valence band and extrapolating the fitted line to the x-axis of the spectrum. The measured V_{bm} of TiO₂, CdS and CdTe films were 3.39 eV, 2.94 eV and 0.46 eV and the calculated valence band position ($VB=V_{bm}+\Phi$) are at 7.49 eV, 6.7 eV and 5.05 eV respectively. The bandgap (E_g) of TiO₂ (3.2 eV) and CdS (2.43 eV), were measured from the UV- visible spectroscopy (**Fig. 3.13(a,b)**) and the calculated CB positions ($VB-E_g$) are 4.29 eV and 4.27 eV respectively. Therefore, the Fermi levels (E_f) of TiO₂ and CdS (4.1 eV

and 3.76 eV) falls below the CB, which clearly reveals that both are consisted with n-type semiconductors. Similarly from **Fig. 3.12(f)** and **Fig. 3.13(c)**, the CdTe ($E_f=4.59$ eV) shows p-type semiconductor behavior, due to its E_f value which is closer to the valence band (5.05 eV) with respect to the calculated CB position of 3.58 eV ($E_g=1.47$ eV). **Fig. 3.13(d,e)** shows the WF of PEDOT:PSS and highest occupied molecular orbital (HOMO) level of CuPc were 5.01 eV and 4.83 eV respectively. **Fig. 3.13(f)** explains the schematic band diagram of fabricated devices.

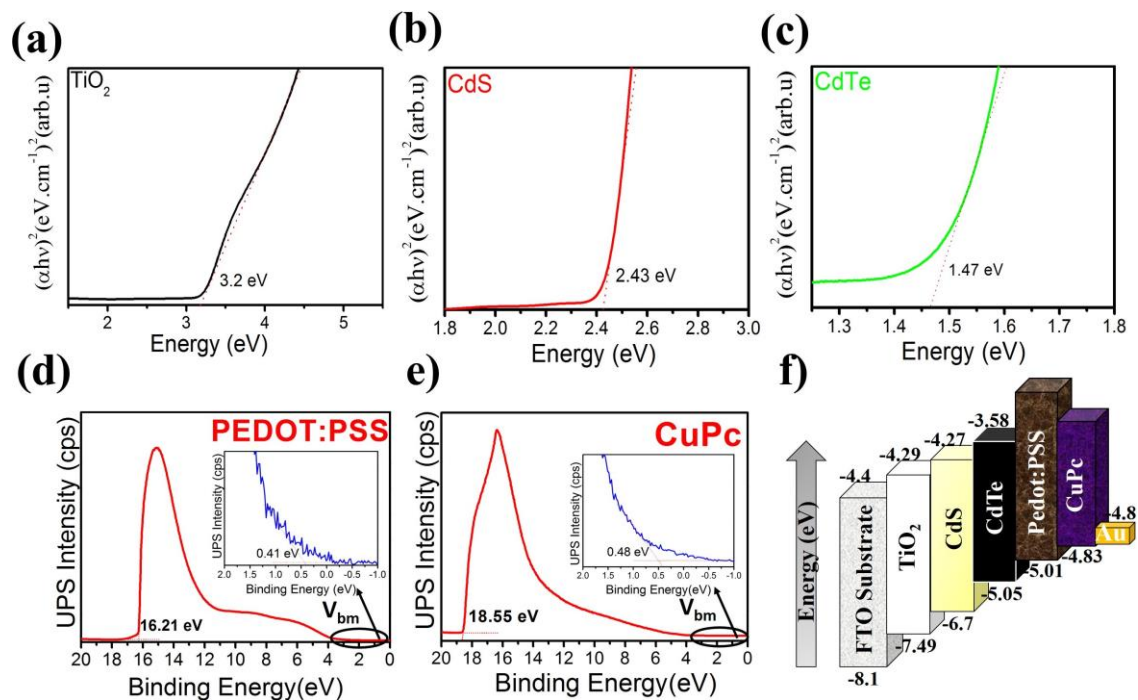


Figure 3.13: Optical band gap of deposited (a) TiO₂, (b) CdS, (c) CdTe thin films, UPS Spectra of (d) PEDOT:PSS (e) CuPC thin films and (f) schematic band diagram of fabricated devices.

3.3.5 Topographical Studies of the Fabricated Thin Films

Fig. 3.14(a-f) shows the cross-section and planar view FESEM images of FTO substrate and the deposited TiO₂, CdS, CdTe, PEDOT:PSS and CuPc films. Note that the CdS/CdTe solar cells shown in **Fig. 3.14(a-f)** were a superstrate configuration that starts with sequential growth of layers on the glass/transparent bottom electrode. **Fig. 3.14(a)** shows a lateral view of the transparent conducting oxide FTO (500 nm) coated over the glass substrate with the granular surface morphology (inset

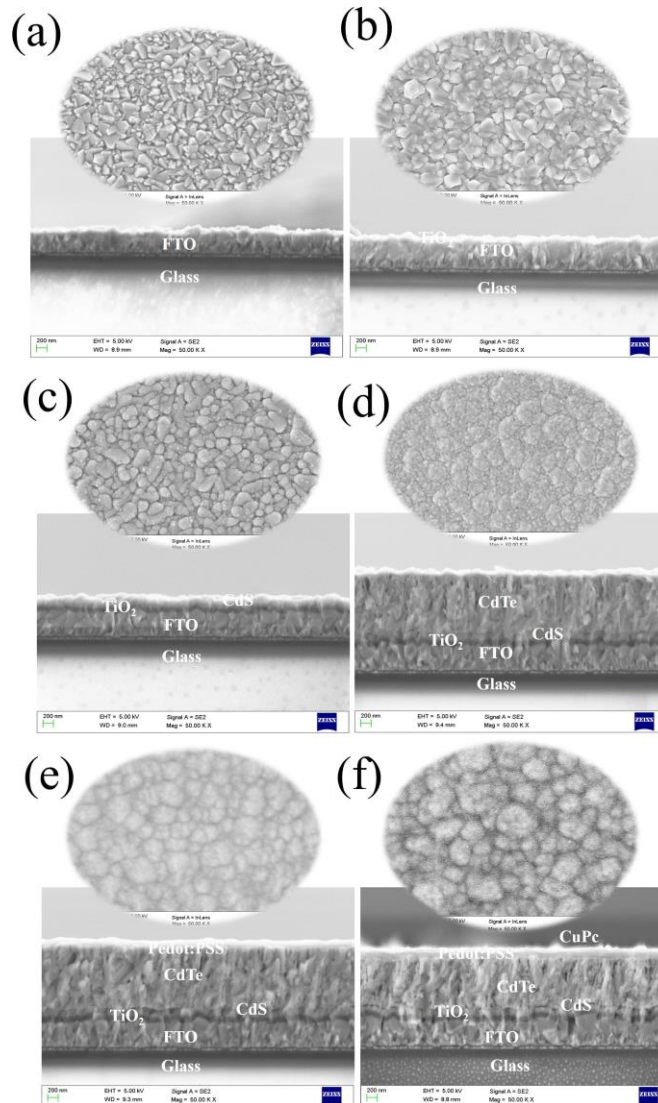


Figure 3.14: Surface morphology and cross section FESEM images (200 nm scale) of (a) FTO coated on glass, (b) TiO₂, (c) CdS, (d) CdTe, (e) PEDOT: PSS, (f) CuPc thin films.

Fig. 3.14(a). The uniform deposition of the TiO₂ window layer (**Fig. 3.14(b)**) helps to prevent the formation of shunt resistance in the device, which arises from the CdTe absorbing layer making contact with the bottom electrode (FTO) through CdS pinholes. **Fig. 3.14(c)** shows the cross-sectional view of the CdS buffer layer deposited over the n-type TiO₂/FTO. **Fig. 3.14(c)** inset shows the morphology of a highly dense, pinhole-free CdS buffer layer with an average grain size of ~ 30 nm. It is noted that an absorbing layer of polycrystalline CdTe film (**Fig. 3.14(d)**) was densely compact

and had good coverage over CdS/TiO₂/FTO. **Fig. 3.14**(e,f) shows the cross-sectional and surface view of spin-coated and thermal evaporated HTL1 and HTL2 on top of CdTe/CdS/TiO₂ layers respectively. It reveals that the HTL1 and HTL2 layers were uniformly deposited consecutively, which helps transport the charge carriers from the granular CdTe layer. Additionally, AFM was used to carry out to study topographical analysis of the deposited TiO₂, CdS, CdTe, PEDOT:PSS and CuPc thin films (**Fig. 3.15**(a-f)). The high-resolution AFM images (small area) 2D and 3D of prepared films also were consistent with FESEM studies.

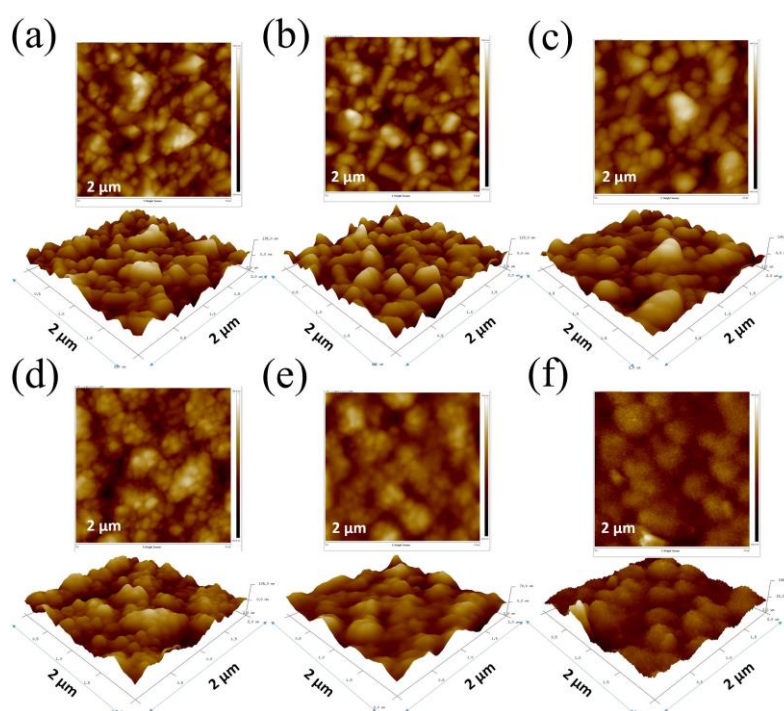


Figure 3.15: Typical high resolution 3D and 2D AFM topographic images of (a) FTO, (b) TiO₂, (c) CdS, (d) CdTe, (e) PEDOT:PSS, (f) CuPc.

3.3.6 Current-Voltage (I-V) Characteristics of the Fabricated Planar Heterojunction CdS/CdTe Devices

The I-V characteristics of the fabricated planar heterojunction CdS/CdTe solar cells are shown in **Fig. 3.16**. The I_{sc} , V_{oc} , FF, and conversion efficiency η of the fabricated devices (A-D) results are summarized in **Table 1**. All the measurements were carried out under 1 sun illumination (1000 W/m²), AM 1.5G solar simulator with an active

area of $\sim 0.2 \text{ mm}^2$. In the present work, the planar heterojunction solar cells were fabricated with four different architectures, device A: FTO/CdS/CdTe/Au, device B: FTO/TiO₂/CdS/CdTe/Au, device C: FTO/TiO₂/CdS/CdTe/PEDOT:PSS/Au, and device D: FTO/TiO₂/CdS/CdTe/PEDOT:PSS/CuPc/Au.

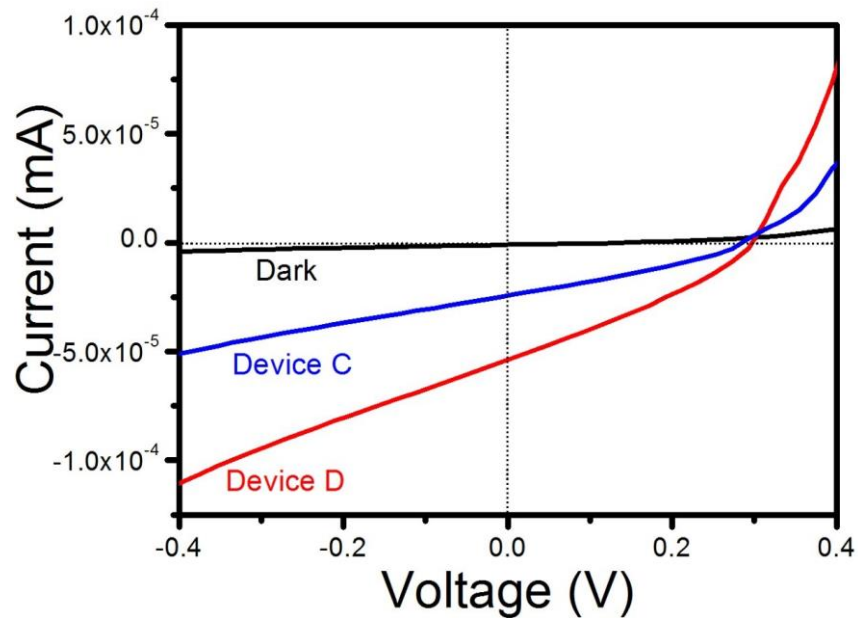


Figure 3.16: I-V characteristics of solar devices C and D.

The solid-state device C exhibited PCE of $I_{sc} = 2.41 \times 10^{-5} \text{ A}$, $V_{oc} = 0.28 \text{ V}$, $FF = 31 \%$, $\eta = 1.25 \%$ and for device D, $I_{sc} = 5.4 \times 10^{-5} \text{ A}$, $V_{oc} = 0.3 \text{ V}$, $FF = 30.7 \%$, $\eta = 2.74 \%$ respectively. When compared with device C, it clearly (see **Table 1**) shows an increase in the open-circuit voltage and short circuit current observed in device D from 0.28 V to 0.3 V and from $2.41 \times 10^{-5} \text{ A}$ to $5.4 \times 10^{-5} \text{ A}$ respectively. The photovoltaic performance of device D showed significant improvement when compared to device C, due to the influence of CuPc as HTL2 along with PEDOT:PSS as HTL1. It clearly shows that the addition of CuPc as HTL2 causes the band bending at the interfaces (PEDOT:PSS/CuPc/Au) as shown in UPS analysis, which increases the short circuit current in device D leading to higher efficiency of the device.

The observed cell parameters were considerably poor compared to the conventional CdS/CdTe solar cells. However, in this first attempt we demonstrated the effect of two back contact layers based prototype in CdS/CdTe planar heterojunction solar cells. The device D showed improved efficiency (2.74%), which is higher than previously reported architecture on FTO/TiO₂/CdS/CdTe/Au thin film solar cell by Mutalikde-

Table 3.1: The power conversion efficiency of fabricated devices.

Device	I_{sc} (A)	V_{oc} (V)	FF (%)	Efficiency η (%)
A	2.1e-6	0.22	31.8	0.081
B	9.08E-6	0.26	30.5	0.40
C	2.41e-5	0.28	31	1.25
D	5.4e-5	0.30	30.7	2.74

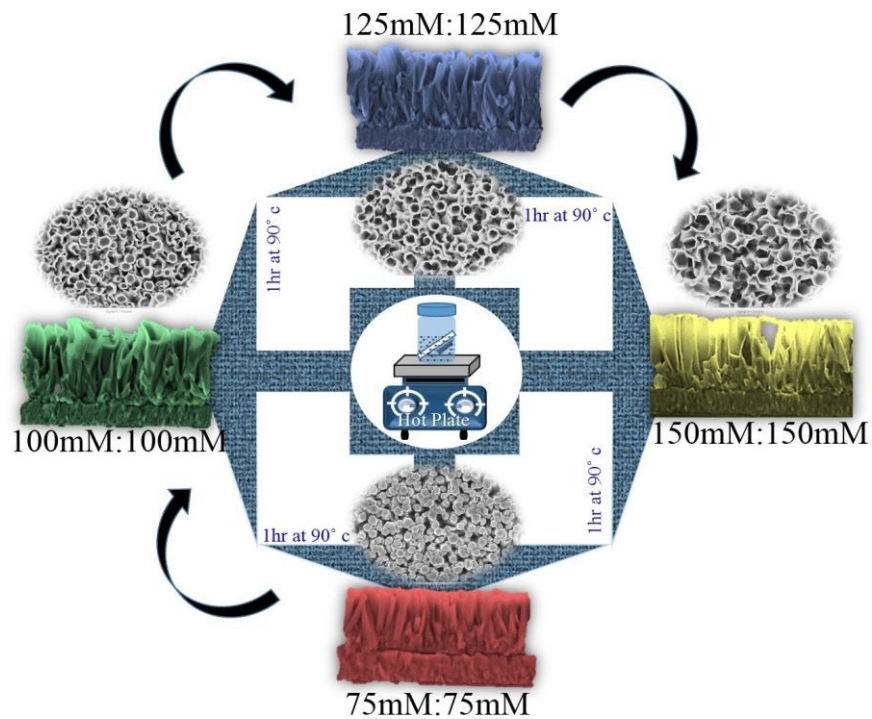
sai and Ramasesha (2017) (0.41 %). However, an appropriate materials design and careful optimization of layer thickness, annealing temperature, and device structure modification will pave the way for high-performance solar cells.

3.4 Conclusions

In summary, the effect of CuPc (HTL2) along with PEDOT:PSS (HTL1) on the performance of CdS/CdTe thin film planar heterojunction solar cells were investigated. Incorporation of CuPc in the device architecture showed the higher conversion efficiency of 2.74 %. This is due to its effective transportation of charge carriers towards the counter electrode (Au) when compared to the device C (1.25 %). This potential advancement will present a new viewpoint for the CdS/CdTe solar cell researchers and also it is useful in designing efficient future PV devices. Additionally, this strategy might be compatible with a broad range of organic photovoltaic materials and offers an effective approach to enhance the performance of CdTe devices. Although the present PCE is 2.74 %, a better theoretical understanding of their interfaces would help improve the design and PCE (Varadharajaperumal *et al.* (2019)).

Chapter 4

Controlled Growth of 1D-ZnO Nanotubes Using One-step Hot Plate Technique for CZTS Heterojunction Solar Cells



4.1 Introduction

1D-ZnO nanostructures are regarded as one of the most fascinating wide bandgap oxide semiconductors owing to its optical transparency in the visible region augments the excited charge carrier separation and transportation in various applications (Star *et al.* (2003), Gao and Wang (2005), Tong *et al.* (2006), Anta *et al.* (2012), Leung *et al.* (2014)). In recent years, several research efforts have been devoted to grow hollow 1D-ZNTs, due to its unique properties such as large surface area, high porosity, light trapping, and high carrier mobility which attract their applications in photocatalysts, gas sensor, biosensor, bio-photonics and solar cells (Vayssieres *et al.* (2001), Sun *et al.* (2006), Martinson *et al.* (2007), Chu *et al.* (2010), Chen *et al.* (2014)). Considering the broad range applications of ZNTs, the growth process generally demands cost-effective, rapid, large scale and modest techniques. So far, highly oriented ZNTs (over various substrates) were successfully synthesized from template assisted, hot plate assisted electrodeposition, hydrothermal and solution-processed techniques (Sun *et al.* (2006), Li *et al.* (2007), İpeksaç *et al.* (2013), Manthina and Agrios (2016), Vasireddi *et al.* (2017)). Among all the aforementioned methods, the simple hydrothermal technique offers an advantage to yield highly scalable, reproducible and most controllable production of ZNTs at low synthesis temperature (< 350 °C) (İpeksaç *et al.* (2013)).

In general, hydrothermally grown ZNTs were synthesized using two-step processes (excluding seed layer deposition). The first step is to prepare ZNRs by controlling the experimental parameters like reactant concentration and volume, reaction temperature and time, substrate positioning, pH and surfactant. The second step is to etch the grown ZNRs using electrolyte solutions, which mainly depends on solution concentration and volume, etching time and temperature (Sun *et al.* (2006), Luo *et al.* (2010)). Due to this complex two-step process, there is an urgent requirement to find a better alternative to replace it with a simple, one step, rapid and low-cost direct synthesis technique to grow ZNTs in large scale with comparable or better material, optical and electronic properties. To date, only a few reports are available on the direct growth process of ZnO tubular structures via conventional hot air oven method by keeping either long reaction time or subsequently cooling down the reaction temperature from high to low or post-deposition aging route (Tong *et al.* (2006), Xu *et al.* (2007)).

In recent years there has been a lot of research interest in fabricating the superstrate structure (a reverse process which is used to prepare conventional substrate cell) based

CZTS thin film solar cells combining with 1D nanostructures. Besides, the superstrate structure has been considered as one of the most suitable approaches to study the advantages of introducing 1D nanostructures in heterojunction as compared to the conventional heterojunction PV devices (Kurokawa *et al.* (2012), Yan *et al.* (2018b)).

4.1.1 Objectives of the Work

The main objective of this chapter work is to develop a simple and rapid one-step hot plate technique for systematic growth of highly oriented ZNRs into ZNTs over the FTO substrate (Fig. 4.1). Further, to study the effect of surface morphology and growth mechanism of ZnO nanostructures by varying precursor concentration, growth time and temperature using hot plate technique; to study the photovoltaic performance of nanostructure introduced, hetero-interface stoichiometry adjusted $\text{Cu}_2\text{Zn}_{1.5}\text{Sn}_{1.2}\text{S}_{4.4}/\text{ZNRs}$ and $\text{Cu}_2\text{Zn}_{1.5}\text{Sn}_{1.2}\text{S}_{4.4}/\text{ZNTs}$ thin films.

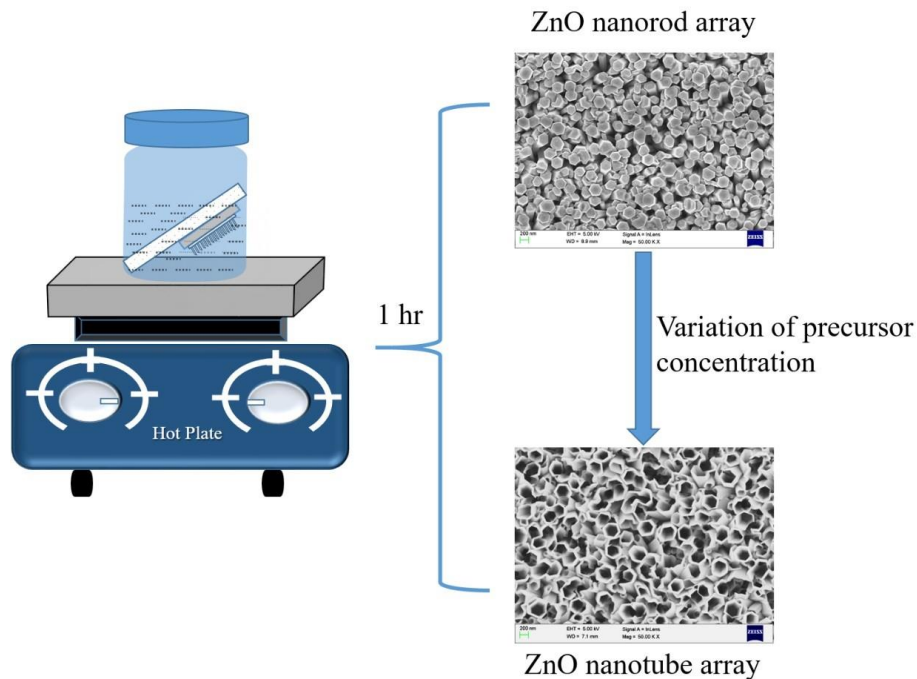


Figure 4.1: Schematic of the hot plate technique used.

4.2 Experimental Details

4.2.1 The Preparation of ZnO Nanostructures

- To synthesize ZnO nanostructures, analytical grade chemicals were used without any extra purification. Before further use, the FTO substrates ($7 \Omega/\text{sqr}$) were ultrasonicated by 1:1:1 ratio solution of DI water, IPA and acetone for 10 mins. Initially, the ZnO (50 nm) seed layer was deposited on top of the FTO substrate using RF magnetron sputtering.

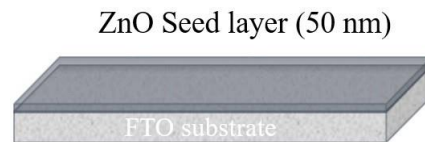


Figure 4.2: ZnO seed layer (50nm) coated FTO substrate.

- The preparation of aqueous solution with 1:1 ratio of zinc chloride (ZnCl_2) and hexamethylenetetramine (HMTA) (as 25mM:25mM, 50mM:50mM, 75mM:75mM, 100mM:100mM, 125mM:125mM, 150mM:150mM and 175mM:175mM) were dissolved in DI water (50 ml) and sonicated for 10 mins. The seeded ZnO/FTO substrates (conducting surface facing down) were kept in a slanting position inside an isolated weighing bottle (shown in **Fig. 4.1**). The solution mixture was introduced into the bottle, after that, it was properly sealed and kept directly over the hot plate. The growth temperature in the hot plate was held at 90°C and experiments were carried out for 1 hr (**Fig. 4.1**) after which it was allowed to cool down naturally (~ 45 mins) to room temperature. Finally, the coated 1D-ZnO nanostructures were thoroughly rinsed with DI water and dried in a hot air oven at 100°C for 5 mins.

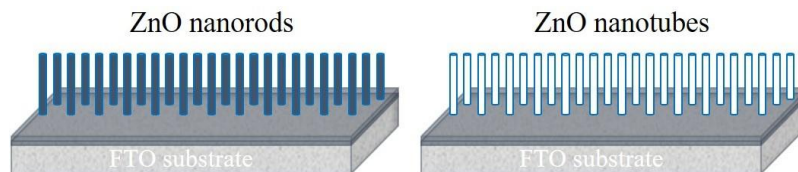


Figure 4.3: ZnO nanostructures (nanorods and nanotubes) deposited on top of FTO substrates.

4.2.2 Preparation of CZTS Alloy and ZNRs/CZTS, ZNTs/CZTS Heterojunction Solar Cell

- The CZTS alloy, prepared from pure Cu, Zn, Sn and S (99.999 % Alfa Aeser), were weighed in a stoichiometric ratio of 2:1.5:1.2:4.4. The materials were transferred into cleaned quartz ampoules and sealed under a pressure of $\sim 1 \times 10^{-5}$ Torr.
- Initially, the ampoule was heated up to 500 °C (5 °C/min) and maintained at that temperature for 1 hr in a furnace. The temperature of the furnace was then further increased to 950 °C. The ampoule was rotated for 24 hrs and then gradually cooled down to room temperature.
- To study the photovoltaic behavior of the grown ZNTs and ZNRs, stoichiometry adjusted $\text{Cu}_2\text{Zn}_{1.5}\text{Sn}_{1.2}\text{S}_{4.4}$ thin film ($\sim 1 \mu\text{m}$), using single-source material (alloy), was deposited on top of ZnO nanostructures at a substrate temperature of 150 °C by the thermal evaporation method (see **Fig. 4.4**).

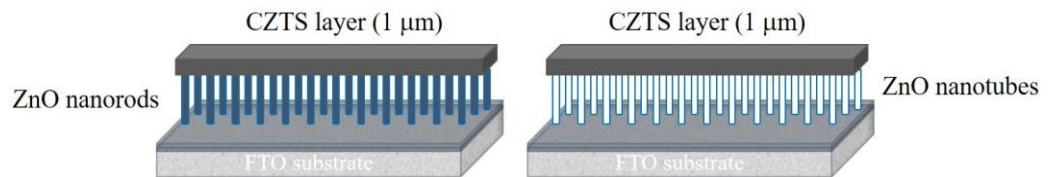


Figure 4.4: CZTS layer deposited over ZnO nanostructures/FTO substrates.

- Au (100 nm) was deposited on top of CZTS/ZnO nanostructures by thermal evaporation method.

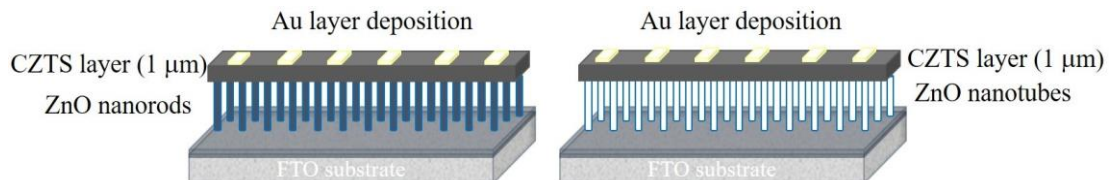


Figure 4.5: Top electrode Au deposited on CZTS/ZnO nanostructures/FTO substrates.

4.2.3 Characterization Techniques

The topographical (lateral and spatial) information of the grown ZnO nanostructures were studied using a high-resolution FESEM. The chemical concentration of absorber CZTS thin film was determined by EDS recorded at 8.5 mm working distance with a beam current of ~ 10 nA and an accelerating voltage of 15 kV. The luminescence properties of ZnO nanostructures were recorded (300 nm to 1000 nm) using CL analysis with the beam current of ~ 20 nA and 20 kV as an accelerating voltage. The phase formation and crystallographic information of the hot plate grown ZnO nanostructures were performed by Raman spectroscopy and XRD respectively.

The surface level oxidation states of grown ZnO nanostructures and CZTS films were obtained from XPS under the condition of 10 mA emission current and 11 kV accelerating voltage (110 W). The DRS of the fabricated films were recorded by the UV-Vis spectrometer (250 nm-1000 nm). The electronic structure of ZnO nanostructures was characterized using UPS with He I source energy (21.22 eV). The current-voltage (I-V) characteristics of the devices were measured using a solar simulator under AM 1.5G.

4.3 Results and Discussions

4.3.1 Surface Morphology of ZnO Nanostructures

Fig. 4.6(a-h) shows the surface morphology of vertically (002) grown high aspect ratio ZnO nanostructures. The growth of open-ended hexagonal faceted ZNRs and their systematic transformation of ZNTs with respect to precursor concentrations was revealed by the FESEM top and a cross-sectional view (inset). The hot plate, single-step growth process strongly contrasts with increased reactant concentrations (25mM:25mM to 175mM:175mM), which affect the ZNRs nanostructures to transform into hollow ZNTs (see **Fig. 4.6(a-g)**). Upon further increasing the reactant concentrations to 200mM:200mM, it was observed that ZNTs are completely distorted and forming ZnO nanoflowers or nanoflakes (shown in **Fig. 4.6(h)**).

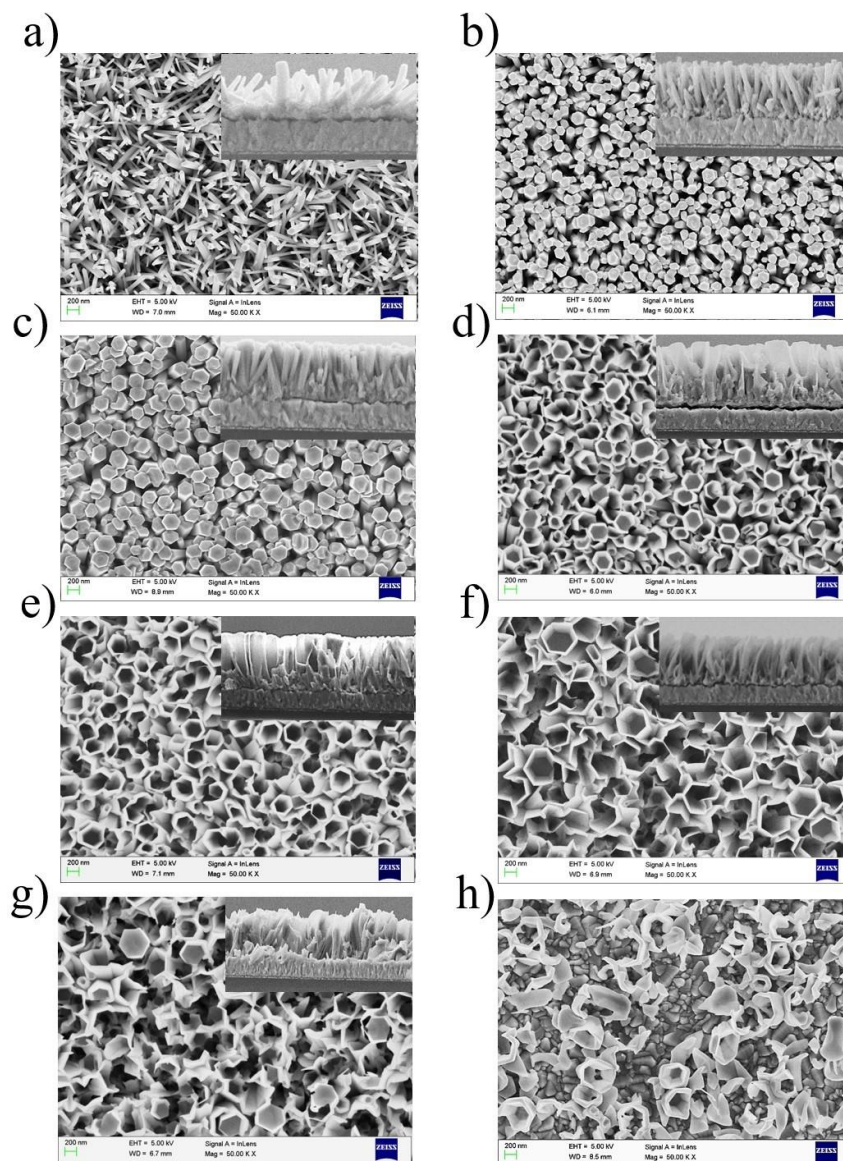


Figure 4.6: 50,000X magnification FESEM images (inset: cross-sectional view) of ZnO nanostructures grown with concentrations of (a) 25mM:25mM (randomly oriented ZNRs), (b) 50mM:50mM (oriented ZNRs), (c) 75mM:75mM (ZNRs formation), (d) 100mM:100mM (ZNTs transformation), (e) 125mM:125mM (ZNTs formation), (f) 150mM:150mM (ZNTs opening up), (g) 175mM:175mM (ZNTs completely opened up), (h) 200mM:200mM (ZNTs completely distorted).

4.3.2 Systematic Growth Process of ZnO Nanostructures

The schematic of the precursor concentration variation, reaction process stages, nanostructures formation and confirming nanorods transformation into nanotubes is shown

in **Fig. 4.7**. The vertical cross-sectional image of a single nanotube in **Fig. 4.7** (top image) clearly shows the nanotube formation.

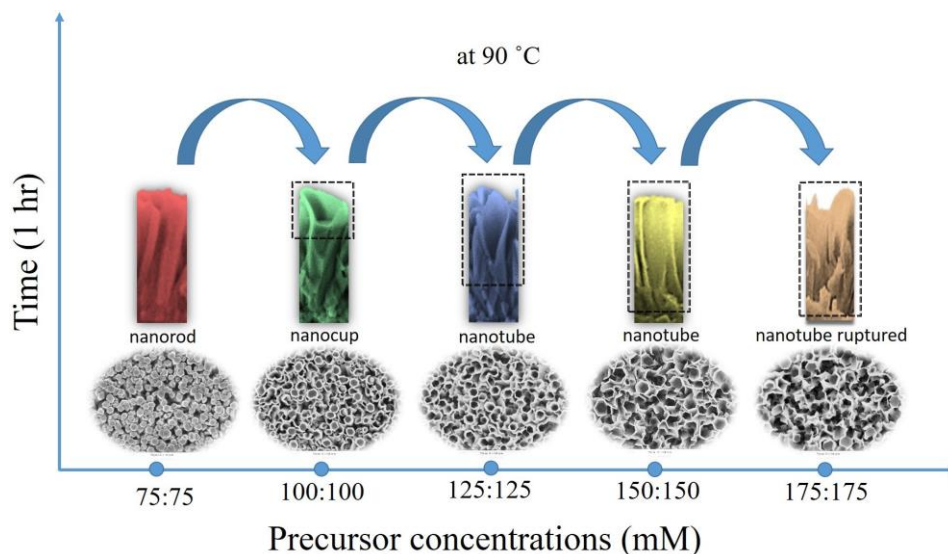


Figure 4.7: Schematic of ZnO nanostructures formation v/s variation of precursor concentrations. Bottom: SEM images of ZnO nanostructures. Top: Cross-sectional view of ZnO single nanorod and nanotube.

The dehydration of Zn^{2+} and Cl^{2-} ions from zinc chloride along with hydroxide (OH) ions from HMTA contained in the aqueous precursor solution decide the growth condition of ZnO nanostructures. Also, as the precursor's concentration exceeds 175mM:17mM (e.g., 200mM:20mM), there was no evidence of the growth of ZNTs (see **Fig. 4.6(h)**). Instead, the transformed nanotubes were found to be ruptured completely.

4.3.3 X-ray Diffraction of ZnO Nanostructures

The macroscopic and microscopic appearances of large area ($\sim 2 \text{ cm}^2$) ZnO nanostructures using a single-step hot plate technique are shown in **Fig. 4.8(a)**. The measured XRD clearly shows the (002) peak as the dominant one, which shows that as-grown ZnO nanostructures exhibit (002) crystalline plane (**Fig. 4.8(b)**). No impurity (Zn or any other) peaks were observed in the recorded XRD spectra. The growth mechanism can be explained by the coordination of Zn^{2+} and OH ions with each other and then undergoing dehydration to form ZnO. The decomposition reaction in HMTA

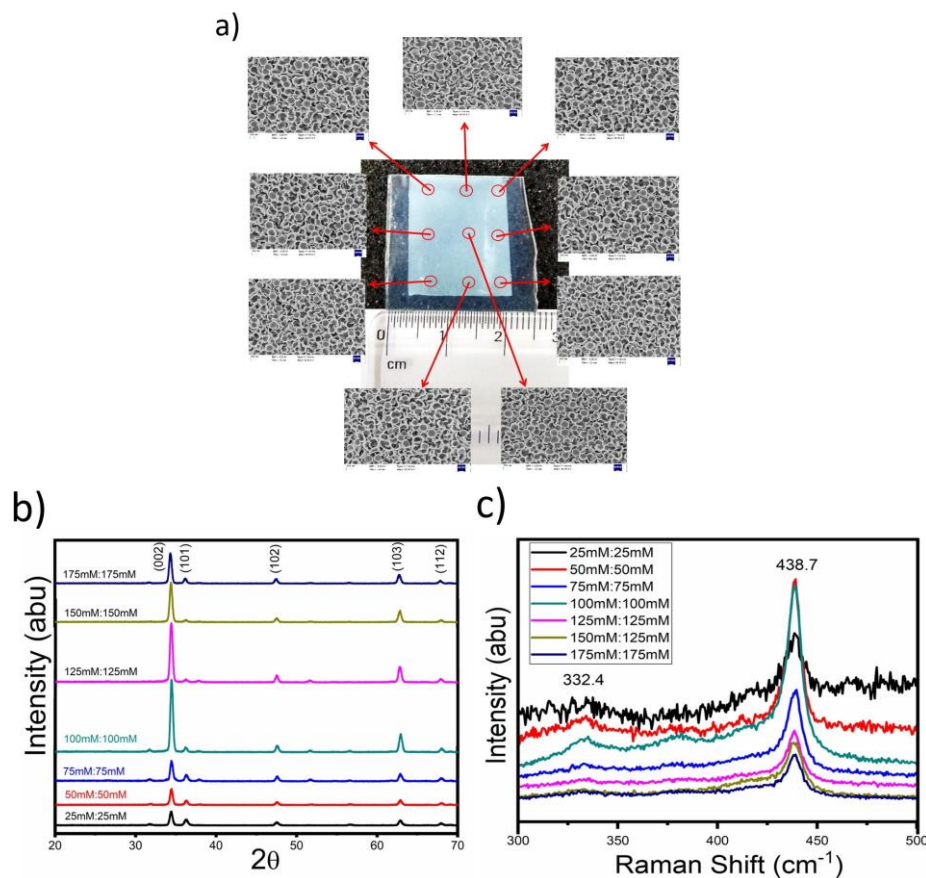
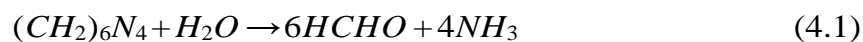


Figure 4.8: (a) Photograph (center) and FESEM images depicting the uniform large area (~ 2 cm²) growth of ZNTs, (b) XRD and (c) Raman spectra of grown 1D-ZnO nanostructures grown using different precursor concentrations.

supplies the ammonia and hydroxyl ions (formaldehyde) in the aqueous solution (described in **equations. 4.1 and 4.2**). Due to the endothermic process with low energy, the direct hot plate method allows ZNTs to grow along the z-axis (002) along with seed layer (001) direction (explained via **equations. 4.3 and 4.4**). However, the exact function of HMTA during the ZnO nanostructures growth is still unclear (Strano *et al.* (2014)).





4.3.4 Raman Spectroscopy Analysis of ZnO Nanostructures

The Raman spectra (300 cm^{-1} to 600 cm^{-1}) of grown ZnO nanostructures contain several sets of optical vibrational modes ($A_1 + 2B_1 + E_1 + 2E_2$), which confirms the ZnO wurtzite structure with C^4 (P63mc) symmetry (shown in **Fig. 4.8(c)**) (Xing *et al.*, 2003). The peak positions at 332.4 cm^{-1} and 438.7 cm^{-1} correspond to the characteristic polar transverse A_1 mode and non-polar optical phonon high E_2 mode respectively.

4.3.5 X-ray Photoelectron Spectroscopy Analysis of ZnO Nanostructures

The surface level oxidation and chemical states of as-prepared 1D nanostructure films were carried out by XPS (**Fig. 4.9(a,b)**). **Fig. 4.9(a)** shows the high resolution scan of Zn $2p_{1/2}$ and Zn $2p_{3/2}$ with peak positions located at 1044.27 eV and 1021.18 eV respectively which represents the Zn-O bonding. The spin-orbital splitting (ΔE) between Zn $2p_{1/2}$ and Zn $2p_{3/2}$ was 23.09 eV, which was identical to the ZnO phase. Also, it indicates that the grown ZnO nanostructures were in Zn^{2+} state (Al-Gaashani *et al.* (2013)). Similarly, the two O 1s peaks located at 529.8 eV and 531.5 eV were attributed to O-O and O-Zn bonding respectively (**Fig. 4.9(b)**). These observed Raman and XPS results consistent with that of XRD data.

4.3.6 Optical Properties of ZnO Nanostructures

Fig. 4.9(c) shows the CL spectra of as-deposited ZnO nanostructures. The peak positions for all the nanostructures at 375.6 nm (3.3 eV), 556.3 nm (2.23 eV) and 755.9 nm (1.64 eV) corresponded to near-band-edge emission, oxygen vacancy and deep level emission respectively (Wang *et al.* (2016a)). The optical properties of ZNRs and ZNTs films were measured at the wavelength (λ) below 400 nm (UV region). The sharp absorption edges were observed for ZNRs and ZNTs at 375.8 nm and 364.7

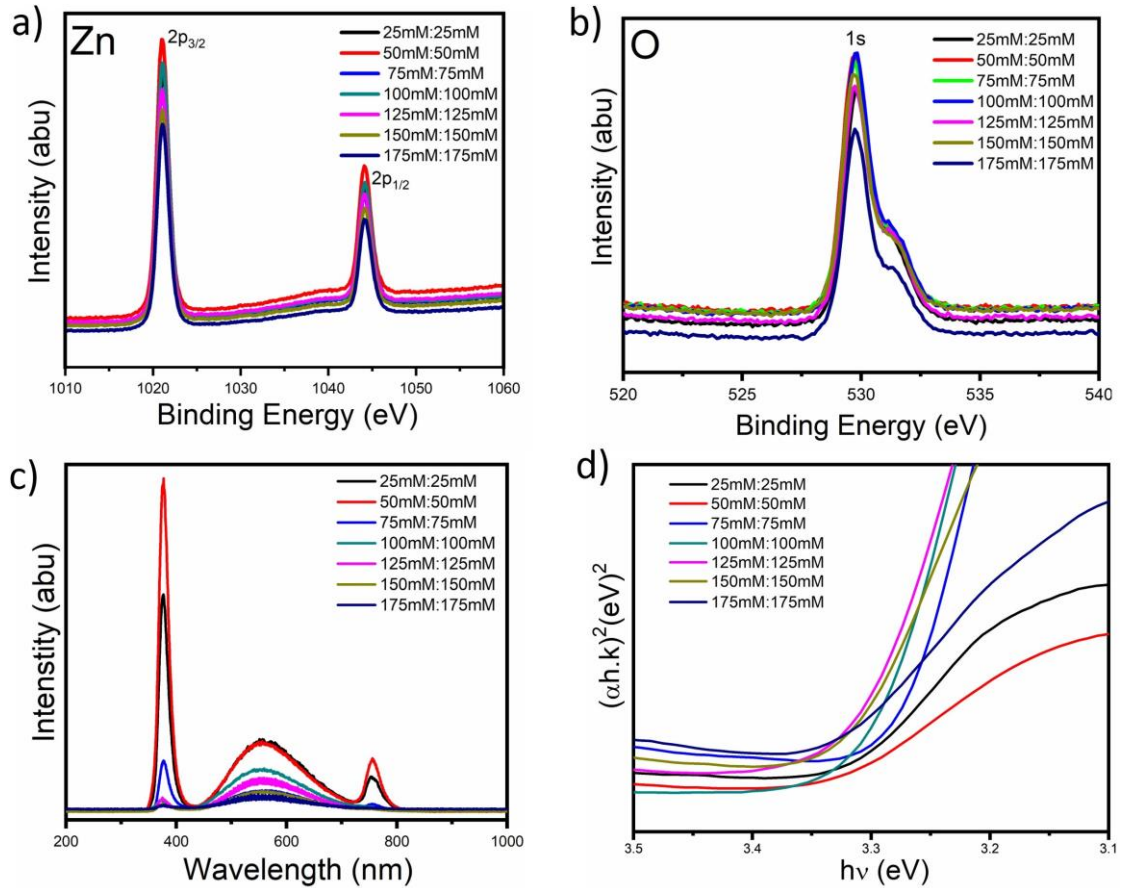


Figure 4.9: (a) and (b) XPS, (c) CL and (d) UV-Visible spectroscopy of 1D-ZnO nanostructures.

nm respectively. The calculated bandgap (E_g) of ZnO nanostructures from reflectance spectra using Kubelka–Munk as a function of incident photon energy and the calculated values were around 3.3 eV to 3.4 eV (**Fig. 4.9(d)**) respectively. The slight shift in ZNTs bandgap ($\Delta E_g = 0.1$ eV) as compared to ZNRs may be attributed to its optical confinement, especially due to light scattering effects and internal stress, surface roughness, and oxygen vacancies (Schlur *et al.* (2018)).

4.3.7 Materials and Optical Properties of CZTS Absorber

The grown nanostructures, ZNRs, and ZNTs films were employed with a p-type stoichiometric adjusted $\text{Cu}_2\text{Zn}_{1.5}\text{Sn}_{1.2}\text{S}_{4.4}$ absorbing layer. The crystalline and elemental concentration levels of CZTS (450 °C annealed) were studied from XRD and energy

dispersive spectroscopy (EDS) analysis techniques (**Fig. 4.10(a)** and (b)). The observed diffraction peaks (from **Fig. 4.10(a)**) of CZTS thin films were obtained at (112), (200), (220), (312), (400), (332), (424) and correspond to 2θ values of 28.52° , 32.70° , 47.45° , 56.25° , 69.38° , 76.82° , 88.59° respectively. This result indicates that the deposited CZTS thin films were highly crystalline with single-phase (JCPDS: 26-0575). The stoichiometric ratio of CZTS film from EDS measurement are shown in **Fig. 4.10(b)** (Ahmed *et al.* (2012)). The 450°C annealed CZTS film bandgap ($E_g=1.49$ eV) was determined using the UV-Vis spectrum and is shown in **Fig. 4.10(c)**.

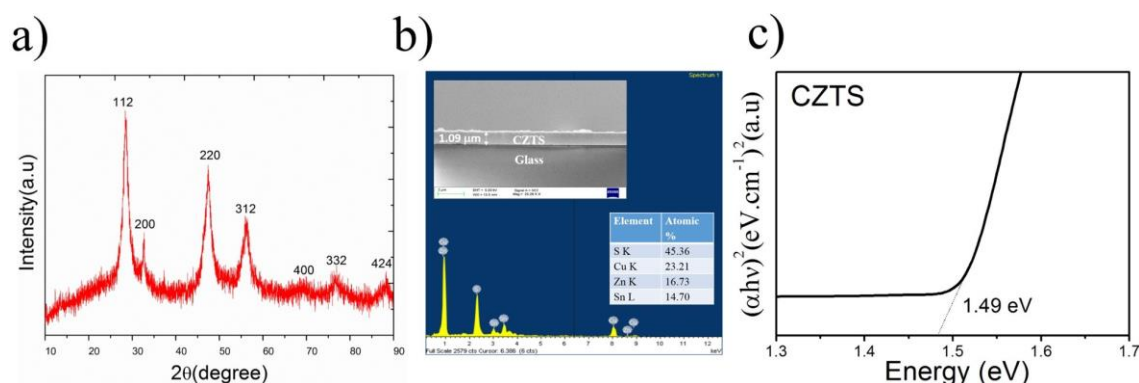


Figure 4.10: (a) XRD, (b) EDS (inset: cross-sectional FESEM images of CZTS/glass substrate), (c) UV-Visible spectrum of CZTS (450°C annealed) thin films.

4.3.8 X-ray Photoelectron Spectroscopy Analysis of CZTS Absorber

Fig. 4.11(a-d) shows the XPS high-resolution core-level spectra of CZTS thin film (Cu 2p, Zn 2p, Sn 3d, and S 2p). The calibration of the recorded binding energy scale was made with respect to the adventitious C 1s peak position (284.6 eV). The binding energy values of Cu 2p_{3/2} and Cu 2p_{1/2} were located at 928.87 eV and 948.76 eV which corresponds to copper (+1) state. The narrow doublet peaks of Zn 2p spectra (Zn 2p_{3/2} and Zn 2p_{1/2}) appeared respectively at the binding energies of 1021.25 eV and 1044.39 eV which signifies the presence of Zn (+2) chemical state. The Sn (+4) oxidation state was confirmed by the Sn 3d_{5/2} and Sn 3d_{3/2} peak positions located respectively at 484.96 eV and 493.35 eV. The S 2p_{3/2} and S 2p_{1/2} spectra exhibit the peak positions at 161.8 eV and 163 eV which were consistent with the expected sulfide phase in the deposited film (Sripan *et al.* (2017b)).

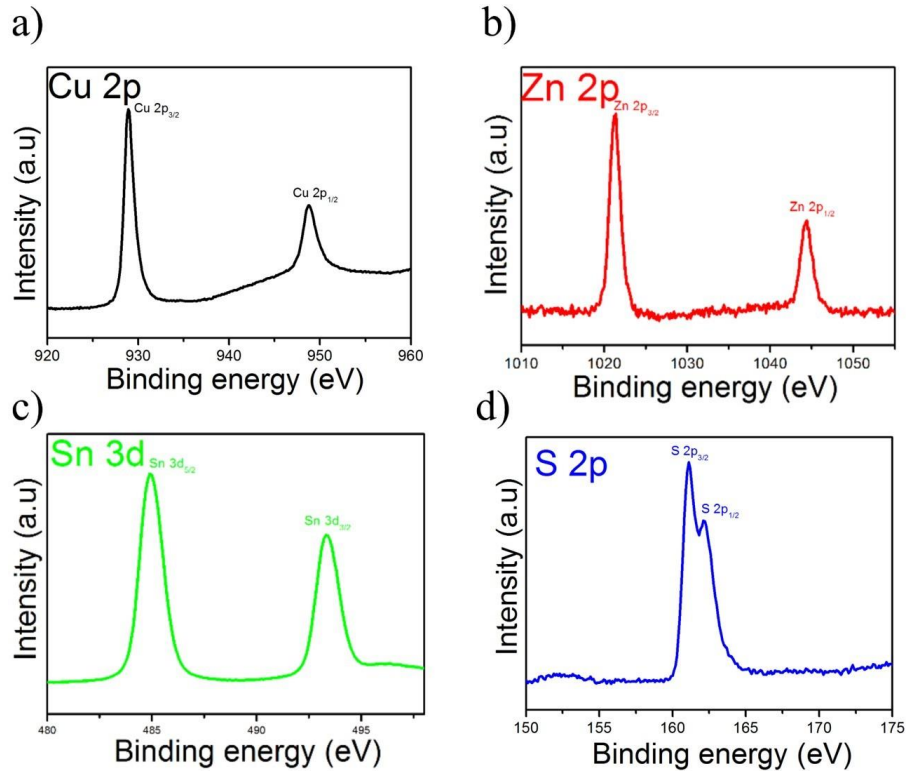


Figure 4.11: XPS core-level spectra of CZTS (450 °C annealed) thin films (a) Cu 2p, (b) Zn 2p, (c) Sn 3d and (d) S 2p.

4.3.9 Ultra-Violet Photoelectron Spectroscopy Analysis of ZnO Nanostructures and CZTS Absorber

To determine the direction of the charge carrier transport and study the heterojunction band alignment, UPS spectra were recorded (**Fig. 4.12(a and b)**). The secondary onset energy (E_1) and the V_{bm} (E_2) of ZNRs, ZNTs and CZTS were observed at 17.34 eV, 17.40 eV, and 16.68 eV, 3.27 eV, 3.24 eV and 0.49 eV respectively. The calculated VB (E_v) energies of ZnO nanostructures and CZTS films were 7.15 eV, 7.06 eV, and 5.03 eV respectively. Therefore, the CB energies (E_c) ($E_v - E_g$) of ZnO nanostructures and CZTS films were estimated to be 3.85 eV, 3.66 eV, and 3.54 eV respectively. **Fig. 4.12(c,d)** shows the band diagram of the fabricated heterojunction devices.

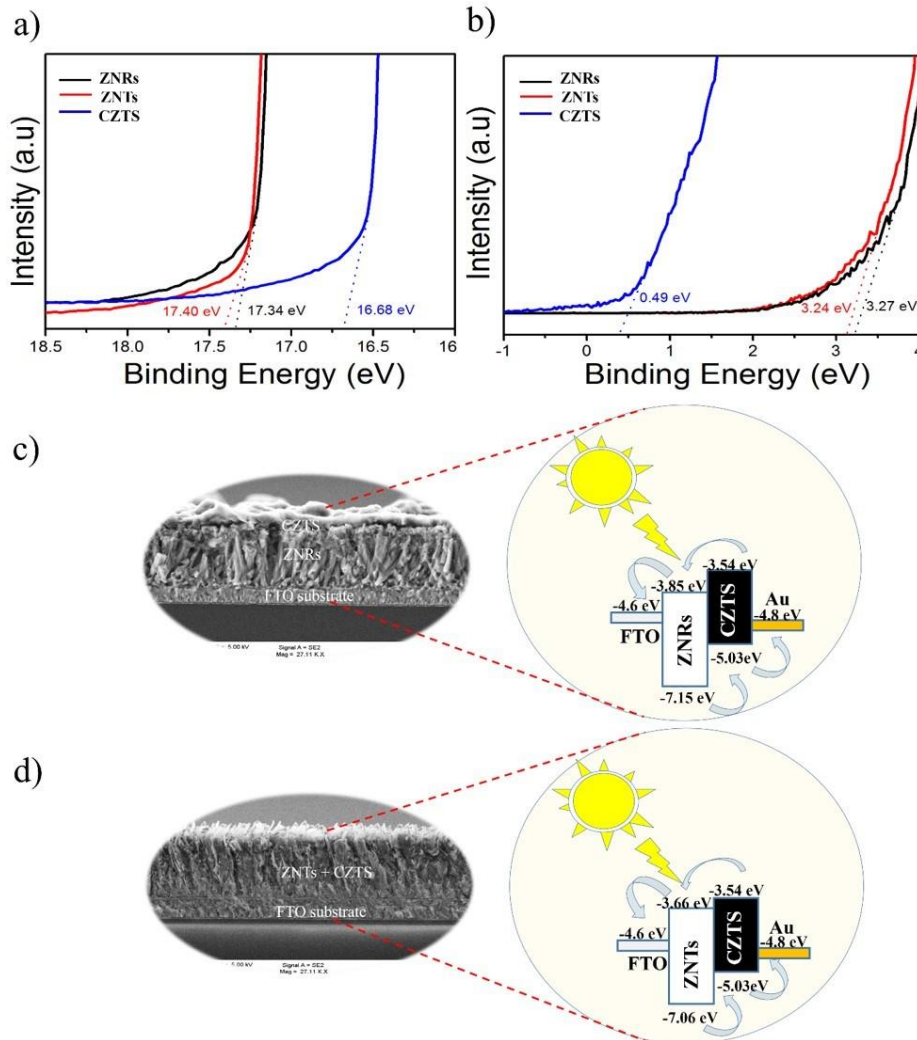


Figure 4.12: (a) and (b) UPS spectra of ZnO nanostructures and CZTS thin film, (c) and (d) schematic band diagram of the ZNRs/CZTS and ZNTs/CZTS heterojunction devices.

4.3.10 Current-Voltage (I-V) Characteristics of Superstrate (ZnO nanostructures/CZTS) Heterojunction Devices

I-V characteristics of the ZnO nanostructures over thin CZTS film shows the diode behaviour in dark and under illuminated condition (1 Sun, AM 1.5G), which confirms the formation of a p-n heterojunction between ZnO nanostructures and CZTS (Fig. 4.13(a,b)) thin film. The increased reverse bias current for ZNTs structured device indicates the effective charge carrier transformation between ZNTs/CZTS interface that may be due to the band offset (ZNTs CB position slightly above the CB of ZNRs shown

in UPS analysis).

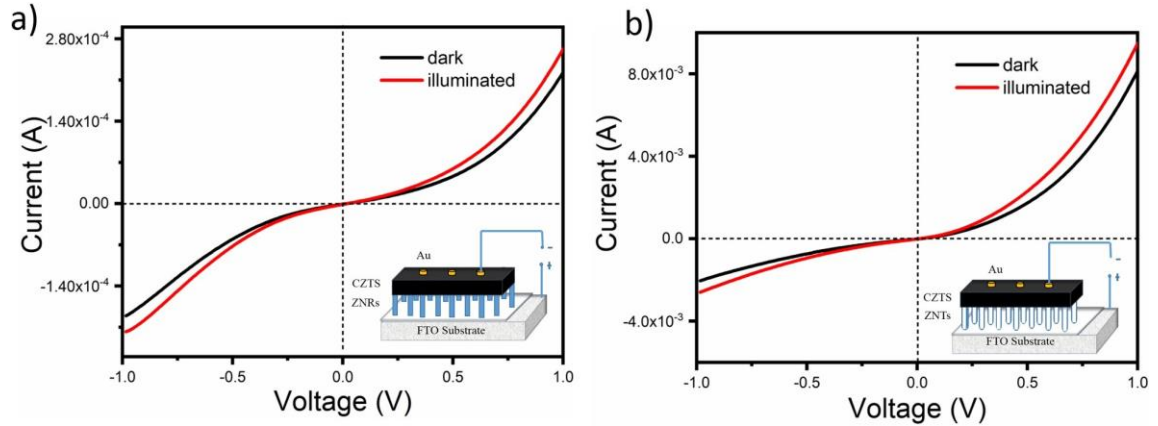


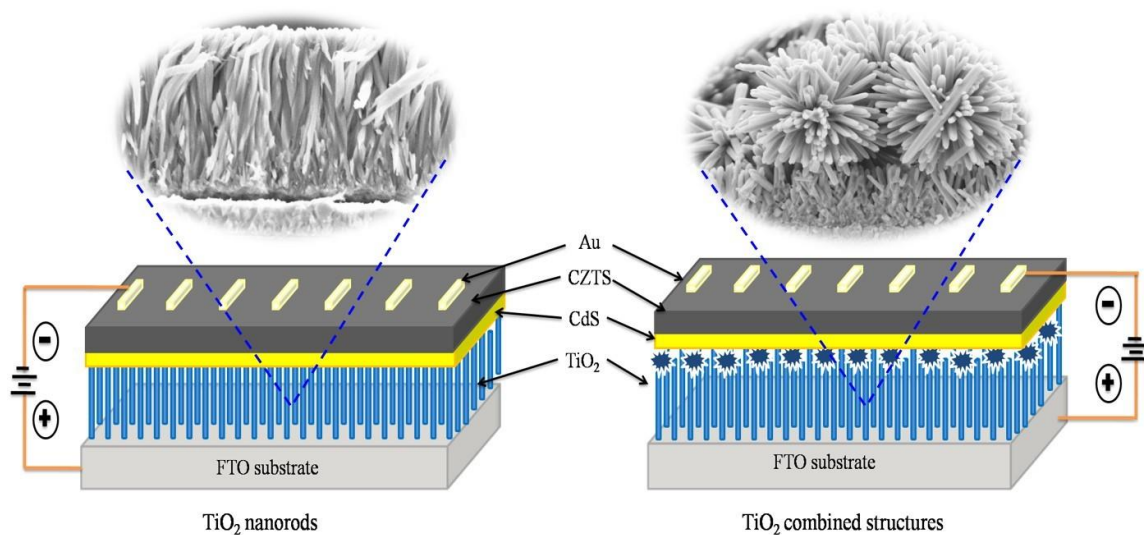
Figure 4.13: I-V spectra of (a) The ZNRs/CZTS, (b) ZNTs/CZTS heterojunction devices.

4.4 Conclusions

In summary, a simple, rapid, single-step, direct hot plate solution technique to grow highly vertical ZNRs, ZnO nano cups and ZNTs with hexagonal (002) wurtzite crystal structure was demonstrated. Surface morphology images have clearly shown that, by keeping growth time the same (1 hour) and increasing the reactant concentration (25mM:25mM to 175mM:175mM), grown nanostructures were found to be transformed from ZnO nanorods to nanotubes. Further increasing the reactant concentration (to 200mM:200mM) ZNTs were completely distorted forming ZnO nanoflowers and nanoflakes. Standard characterization techniques have confirmed their structural, optical and electronic properties. Proposed single-step direct hot plate synthesis process has been shown to be a very useful in rapid, controlled growth of large scale ZNRs and ZNTs at low cost over any ZnO seeded substrates. Also, it can be extended to fabricate highly oriented, large area ZnO nanorods and nanotubes for various applications. Further, it was observed that ZnO nanotube incorporated CZTS films form a better heterojunction with a higher photocurrent. Finally, the present work opens up a new perspective of introducing ZnO nanostructures in CZTS based heterojunction solar cells (Varadharajaperumal *et al.* (2020)).

Chapter 5

Morphology Controlled n-type TiO_2 and Stoichiometry Adjusted p-type $\text{Cu}_2\text{ZnSnS}_4$ Thin Films for Photovoltaic Applications



5.1 Introduction

Recently, in CZTS thin film solar cells, to separate the photogenerated charge carriers and improve the device efficiency, many researchers have explored introducing an interfacial or buffer layer like CdS and ZnS, etc., (Tajima *et al.* (2017)). Among them, CdS is one of the most commonly used buffer layers which showed the highest efficiency of 12.6 %, owing to its wider optical band gap (~ 2.5 eV) and good interfacial properties with CZT(S,Se) (Wang *et al.* (2014)). Moreover, further augmentation for enhancing the LHE and charge carrier transportation in CZTS was achieved by introducing an effective photoanode or window layer in the hetero-interface (CdS/CZTS) geometry. The TiO₂ is one of the widely used n-type window layer in DSSCs, QD solar cells, QD-DSSCs, perovskite, and CZTS solar cells, due to its high transparency in the visible region, low cost, non-toxicity and large refractive index (Hagfeldt *et al.* (2010), Robel *et al.* (2006), Kim and Park (2014), Wang *et al.* (2013), Wang and Demopoulos (2015), Hanaor and Sorrell (2011)). It was reported that the DSSCs have shown higher PCE along with the TiO₂ nanoparticles as a window layer (Hagfeldt *et al.* (2010), Fan *et al.* (2011)). In contrast, the nanoparticles have a large surface area for enhancing the electron trap at the grain boundaries (at the interface), which results in the creation of recombination centers and reduction of net electron transportation (Dou *et al.* (2016)).

Hendry *et al.* 2006 and Zhao. K. *et al.* 2016 had demonstrated that the mobility of electron in metal oxides strongly depended on its morphological structure (Hendry *et al.* (2006), Zhao *et al.* (2016)). The highly oriented 1D TiO₂ nanostructures such as nanorods and nanotubes assist the photogenerated electrons by providing an uninterrupted electrical pathway towards the bottom electrode (Liu and Aydil (2009), Roy *et al.* (2010)).

A variety of synthesis methods have been studied and explored to grow TiO_2 nanorods, which includes CVD, glancing angle deposition, oblique angle deposition and hydrothermal technique (Liu and Aydil (2009), Pradhan *et al.* (2003), Colgan *et al.* (2004), He *et al.* (2008)). Among them, the hydrothermal method is a simple, cost-effective and suitable for large scale deposition. Besides, the crystallinity and surface morphology of the films can be easily tuned by changing the deposition parameters such as reaction temperature, growth time, pH, precursor's volume and concentration (Liu and Aydil (2009)). Additionally, in the past few decades, a lot of research activities were directed to improve the charge separation and quick electron transportation via constructing TiO_2 hierarchical nanostructures within the solar cell architecture (Zhu *et al.* (2012), Lü *et al.* (2010)).

5.1.1 Objectives of the Work

The major goal of this chapter is, to synthesize the window layer of highly oriented TiO_2 1D nanorods and 3D-hierarchical or combined nanostructures on FTO substrate using single-step hydrothermal method. Then, to combine n-type TiO_2 1D/3D nanostructures and stoichiometry adjusted p-type CZTS materials to develop a novel inverted (superstrate) CZTS solar cells (FTO/TiO_2 1D/3D nanostructures/ $\text{CdS}/\text{CZTS}/\text{Au}$) and to study the effect of 1D & 3D TiO_2 nanostructures as an electron transporting layer in superstrate type CZTS thin film PV devices (**Fig. 5.1**).

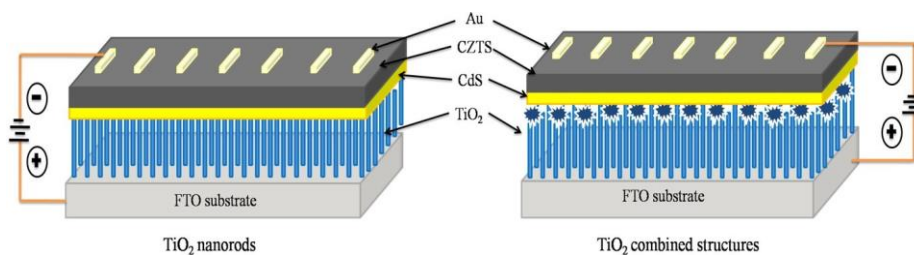


Figure 5.1: The schematic diagram of TiO_2 nanorods and TiO_2 combined structures (TiO_2 nanostructured films) PV device architectures.

5.2 Experimental Details

5.2.1 The FTO/TiO₂ (1D and 3D)/CdS/CZTS/Au Device Fabrication

The methodology for device fabrication with the above configuration is as follows:

- The FTO substrates (resistivity 7 Ω /square) were cleaned by ultra-sonication with 1:1:1 ratio of acetone, 2-propanol, and DI water for 15 min, after that it was dried under N₂ gas before further use. Rutile phase of TiO₂ nanostructured films were synthesized on top of FTO coated glass substrate by single-step hydrothermal method (without any surfactants).

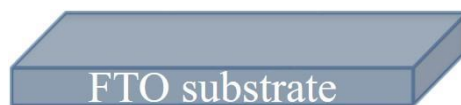


Figure 5.2: Cleaned FTO substrate

- TiO₂ seed layer (50 nm) was deposited over FTO substrates by RF magnetron sputtering, then the substrates were air annealed in a furnace at 450 °C for 30 min.

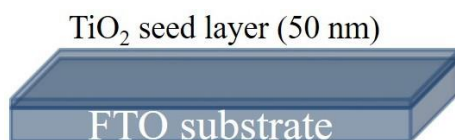


Figure 5.3: TiO₂ seed layer (50nm) coated FTO substrate

- A mixture of concentrated hydrochloric (HCl) acid (35-38 %) and DI water in 2:1 ratio were sonicated at ambient temperature for 5 min. For the growth of TiO₂ nanostructured films, 0.5 mL of titanium (IV) isopropoxide (TTIP) precursor and 1:1 ratio of 0.5 mL of TTIP and titanium (IV) butoxide (TBO) precursors were respectively added dropwise into the mixtures. Then, both solutions were further sonicated for 5 min at ambient temperature. Following this, the solutions were poured into 50 mL Teflon lined stainless steel autoclaves.

- The seed layer coated TiO₂ (50 nm)/FTO substrates were placed inside the autoclave by conducting surface facing up. The sealed autoclaves were kept inside the hot air oven and heated up to 180 °C and maintained for 60 min. After completion of the hydrothermal process, the autoclaves were cooled down slowly to reach room temperature and then the films were thoroughly rinsed with DI water.

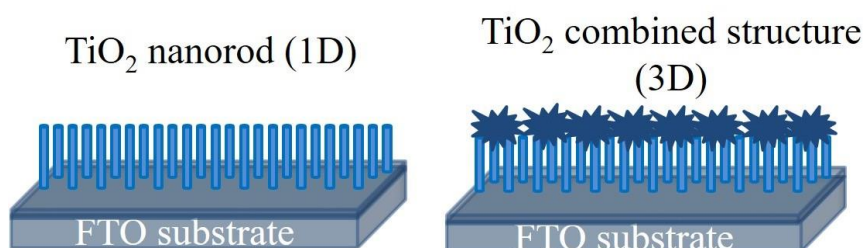


Figure 5.4: TiO₂ nanostructured (1D & 3D) films deposited on FTO substrates

- The deposition of the CdS buffer layer on top of FTO/TiO₂ (1D and 3D) was carried out using the CBD method using the precursor of cadmium sulphate (CdSO₄), thiourea (CH₄N₂S) and ammonium hydroxide (NH₄ OH). 0.0015 mol of CdSO₄ dissolved with 35 mL of DI water, followed by 7.8 mL of NH₄OH (1.5 mol) solution was vigorously added (solution A). 0.05 mol of CH₄N₂S dissolved in 35 mL of DI water (solution B) was added dropwise to mix with solution A. The TiO₂ nanostructured thin films were immersed into the prepared solution contained in a beaker. The solution was modestly stirred and the temperature was maintained around 70 °C to form CdS buffer layer (yellowish) for 3-4 min. The deposition lasted for 7 min (~ 50 nm), then the samples were rinsed with DI

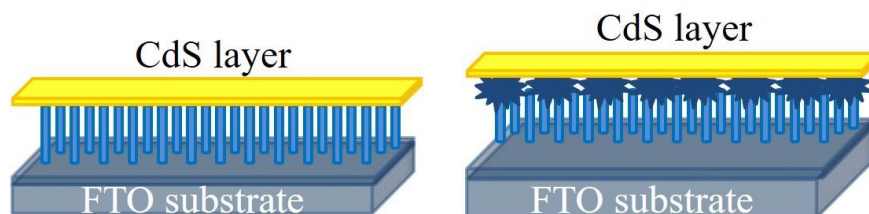


Figure 5.5: CdS coated on TiO₂ nanostructured (1D & 3D) films/FTO substrates

water and allowed to dry at room temperature. Following this, the films were annealed under a nitrogen atmosphere at 350 °C for 2 min.

- An absorbing layer of stoichiometric adjusted CZTS thin film (1 μm) was deposited on top of CdS/TiO₂ nanostructured (1D & 3D) films/FTO using thermal evaporation technique at a substrate temperature of 150 °C using single-source material. Then, the coated films were annealed under a nitrogen atmosphere at 450 °C for 30 min.

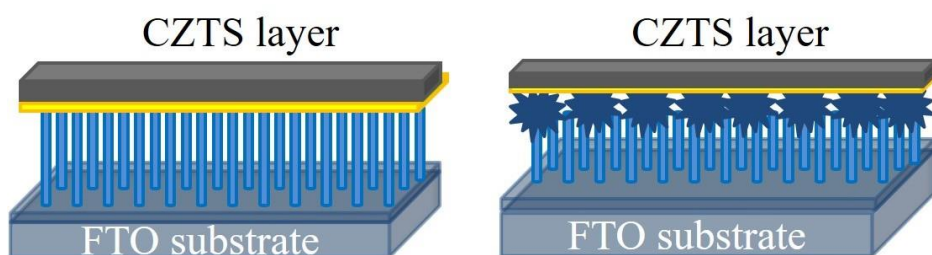


Figure 5.6: CZTS layer deposited on top of CdS/TiO₂ nanostructured (1D & 3D) films/FTO substrates.

- Deposition of top electrode Au (100 nm) over CZTS/CdS/TiO₂ nanostructured (1D & 3D) films/FTO was carried out by the thermal evaporation method.

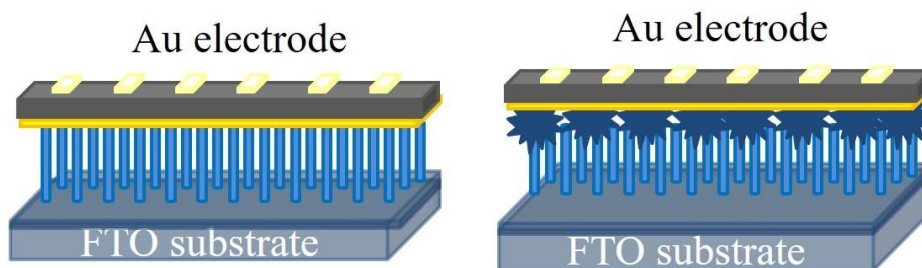


Figure 5.7: Top electrode Au deposited on top of CZTS/CdS/TiO₂ nanostructured (1D & 3D) films/FTO substrates.

5.2.2 Characterization Techniques

The surface morphology and luminescence property of the fabricated thin films were studied using FESEM and CL. The CL spectra were recorded with ~ 20 nA beam

current, 20 kV as an accelerating voltage and the wavelength range from 300 nm to 1000 nm. Structural analysis of the TiO₂ nanostructured films and CZTS thin films were carried out by XRD using Cu-K α source (wavelength=1.5405 Å) with diffraction angle from 10° to 80°. The detailed structural properties were analyzed using high-resolution TEM. The samples were prepared by mixing a few mg of TiO₂ nanostructured films with isopropyl alcohol of concentration 0.2 g/mL followed by ultrasonication for 20 min. The solution was dispersed in a carbon coated copper grid and then it was dried at 100 °C for 2 h.

The phase formation of TiO₂ nanostructured films and CZTS thin films were investigated employing Raman spectroscopy using 532 nm as the excitation wavelength. The chemical state analysis of TiO₂ nanostructured films were performed by XPS. The XPS survey along with core level high-resolution spectra were obtained by monochromatic Al K α X-ray (1486.6 eV) at the vacuum level of 10⁻⁹ Torr. The measurement was carried out at an applied beam current of 9 mA and an acceleration voltage of 13 kV (117 W). The UPS studies were carried out to find the V_{bm} of TiO₂ nanostructured films using the source energy of He I (21.22 eV). The DRS of TiO₂ nanostructured films and the absorption spectrum of CZTS films were recorded by the UV-Vis spectrometer in the range of 250 nm-500 nm and 500 nm-1100 nm at room temperature respectively. The current-voltage (I-V) performance of the fabricated devices was measured by the solar simulator under AM 1.5G.

5.3 Results and Discussion

5.3.1 The Surface Morphology Studies of TiO₂ Nanostructured Films, CZTS Thin Film and the Fabricated Hetero-Interface Devices

The FESEM images of as-deposited TiO₂ nanostructured films are shown in **Fig. 5.8**(a-f). The grown TiO₂ nanorods were in tetragonal shape with square top facets (see **Fig. 5.8**(a,b)) and highly dense over the surface of the FTO substrate. **Fig. 5.8**(c,d) shows the uniformly dispersed microspheres on the surface of nanorod arrays. The TiO₂ nanorods had an average diameter of ~ 50 nm and length around ~ 2.5 μ m. Besides, with an addition of another titanium precursor TBO with TTIP, there was a formation of marigold-like structure on top of the nanorods which resulted in increase in the length up to ~ 6 μ m (nanorods along with microspheres) and diameter (microspheres) around ~ 8 μ m.

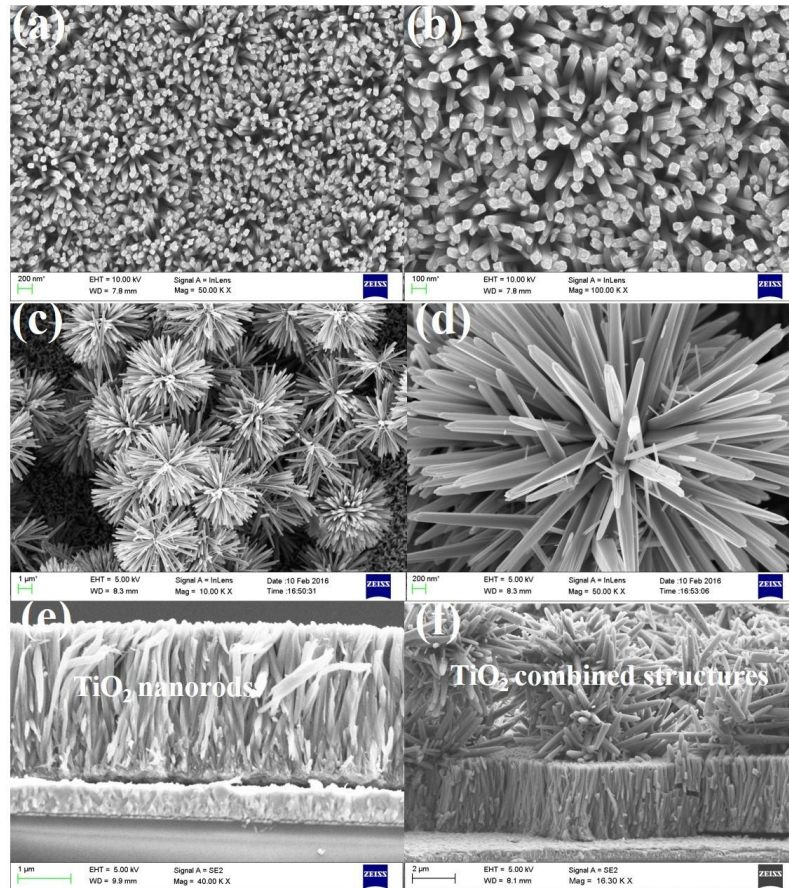


Figure 5.8: FESEM images of (a & b and c & d) top and (e & f) cross-sectional view of TiO_2 nanostructured films.

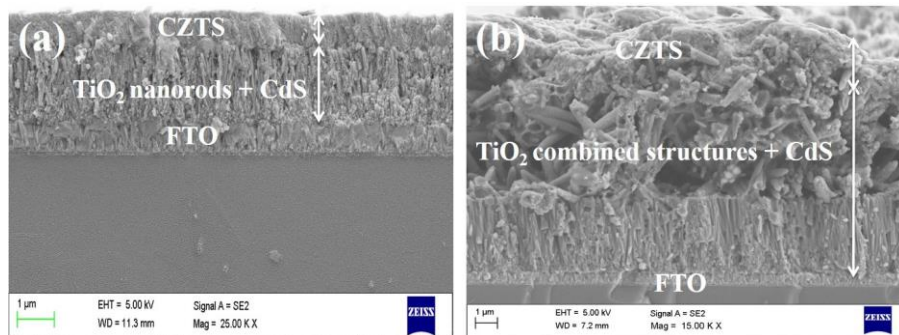


Figure 5.9: Cross-sectional FE-SEM image of the devices (a) annealed $\text{Cu}_2\text{Zn}_{1.5}\text{Sn}_{1.2}\text{S}_{4.4}/\text{CdS}/\text{TiO}_2$ nanorods/FTO and (b) annealed $\text{Cu}_2\text{Zn}_{1.5}\text{Sn}_{1.2}\text{S}_{4.4}/\text{CdS}/\text{TiO}_2$ combined structures.

The cross-sectional FESEM images of TiO_2 nanorods and TiO_2 combined structures are shown in **Fig. 5.8**(e,f), which reveals the vertically oriented TiO_2 nanorods and highly dense uniformly dispersed microspheres on the surface of nanorod arrays. **Fig. 5.9**(a,b) depicts the lateral view of CZTS/CdS/ TiO_2 nanostructured films/FTO, which shows CdS anchored on top of TiO_2 nanostructured films and uniform deposition of CZTS film over the CdS/ TiO_2 nanostructured films. **Fig. 5.10**(a-d) shows FESEM images of as-prepared and 450 °C annealed CZTS/ TiO_2 nanostructured film (1D & 3D) devices. It revealed that annealing led to re-crystallization and increase in grain size over the CdS/ TiO_2 nanostructured films compared to the as-prepared CZTS films. However, the deposited films were smooth, homogeneous and uniform, but in the case of annealed films, the presence of voids or cavities due to deficiency of the elements was observed.

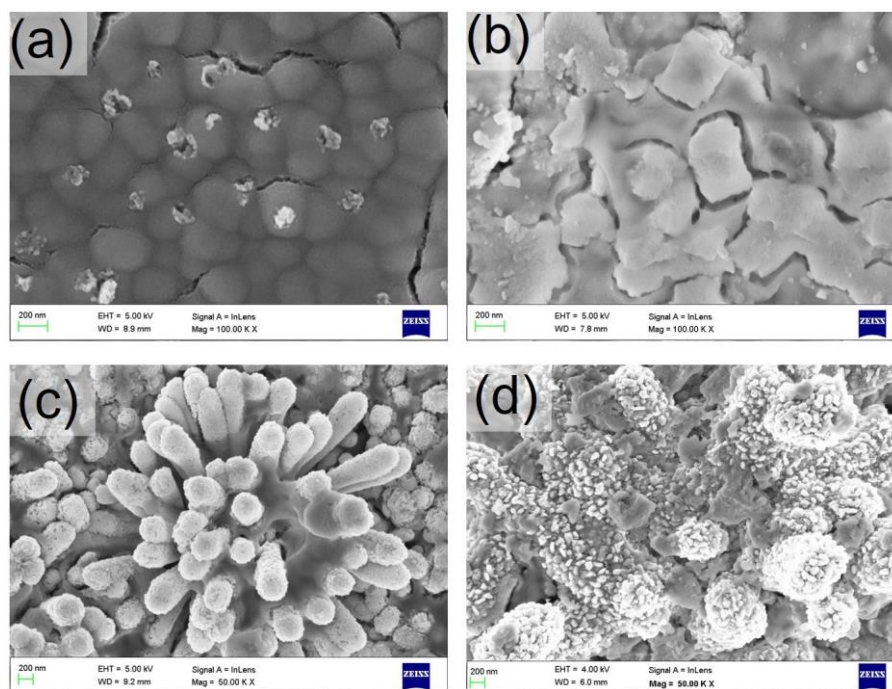


Figure 5.10: FESEM images of (a & b) as-deposited and (c & d) 450 °C annealed CZTS over CdS/ TiO_2 nanostructured films.

5.3.2 X-ray Photoelectron Spectroscopy Analysis of TiO₂ Nanostructured Films

The XPS analysis was performed to study the surface and sub-surface level composition and chemical states (depth information up to ~ 10 nm) of rutile phase TiO₂ nanostructured films. **Fig. 5.11(a)** shows the survey spectra of TiO₂ nanostructured films. The peak presents binding energies of 529.6 eV and 458.4 eV were corresponds to O 1s and Ti 2p_{3/2} orbitals respectively. **Fig. 5.11(b)** shows the high-resolution Ti 2p spectrum with binding energies of 458.4 eV and 464.1 eV were assignable to 2p_{3/2} and 2p_{1/2}, respectively and they were separated from each other by 5.7 eV. This indicates that in the synthesized TiO₂ nanostructured films, Ti atoms were in Ti⁴⁺ chemical state. It also confirms that there was no evidence of the Ti³⁺ state observed in the Ti 2p spectra. A well-formed binding energy peak at 529.6 eV was attributed to oxygen bonding in the TiO₂ matrix (**Fig. 5.11(c)**). One shoulder peak at 533.1 eV was observed and is attributed to hydrolysis for samples prepared by the hydrothermal method. (Mali *et al.* (2016), Li *et al.* (2015)).

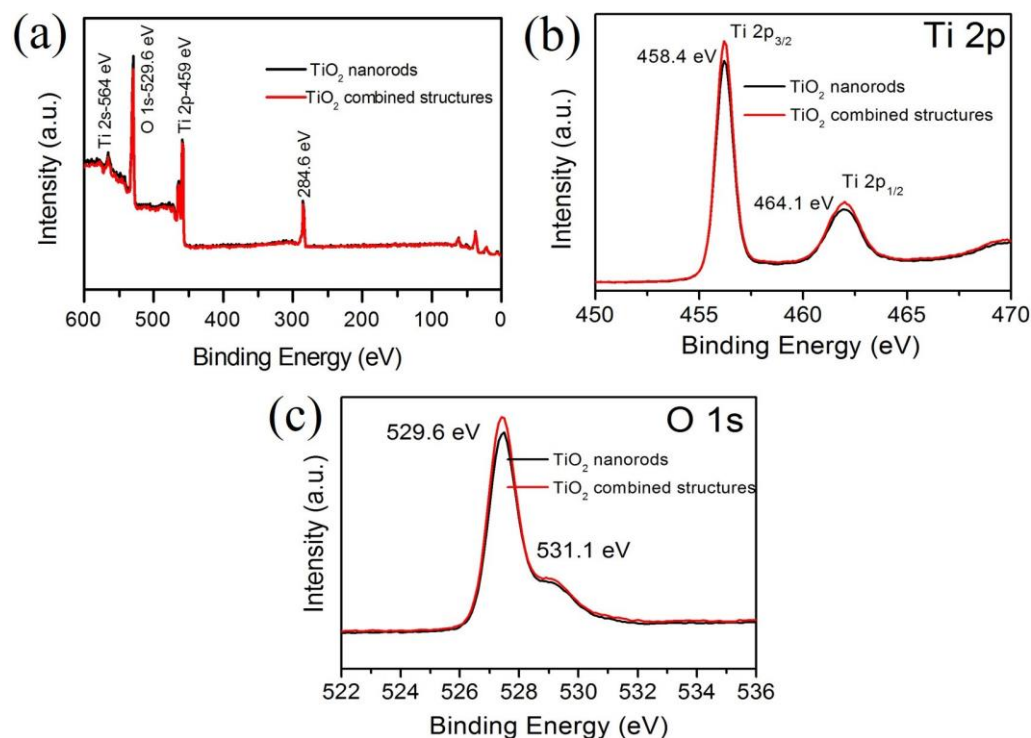


Figure 5.11: XPS spectra of TiO₂ nanostructured films (a) wide (b) Ti 2p (c) O 1s.

The adventitious C 1s spectral line 284.6 eV (C-C) was taken as reference for the

shift correction of Ti 2p and O1s spectra (**Fig. 5.11(b,c)**). It was observed that, in both the TiO₂ nanostructured films, there was no shift in peak position and extra shoulder peaks, while it showed a slight variation in their peak intensity. Also, it revealed that there was no change in their composition and chemical state, which confirms the formation of TiO₂ phase.

5.3.3 Raman Spectroscopy of TiO₂ Nanostructured and CZTS Thin Films

Fig. 5.12(a) shows the laser Raman spectra of TiO₂ nanostructured films. Based on the space group D_{4h}^{14} for rutile and assumed site symmetries for the Ti and O atoms within the unit cell, the Raman-active “lattice vibrations” are assigned as follows: $A_{1g}(610\text{ cm}^{-1})+B_{1g}(144\text{ cm}^{-1})+B_{2g}(827\text{ cm}^{-1})+E_g(446\text{ cm}^{-1})$. The typical Raman bands of rutile phase at 237 cm^{-1} (two phonon bands), $446\text{ cm}^{-1}(E_g)$ and $608\text{ cm}^{-1}(A_{1g})$ were attributed to Ti-O-Ti vibrations and the characteristic peaks of rutile TiO₂ crystal system (Wang and Demopoulos (2015), Mali *et al.* (2016), Sutiono *et al.* (2016), Ji *et al.* (2016)). The sharpness of the peaks and their intensity signifies that the samples were highly crystalline and pure. Also, there was no peak observed for blue shift of the E_g mode among the samples and the TiO₂ nanostructures can be ascribed to the characteristic vibrational modes of the rutile phase which is consistent with XPS analysis.

Quaternary Cu based chalcogenide solar cells (Cu-poor and Zn-rich) showed the highest energy conversion, due to the formations of V_{Cu} , Zn_{Cu} , and anti-site defect Cu_{Zn} . These defects reduce the secondary phase formation and show enhancement in its tunable optical and electrical properties, makes it a promising material for thin film solar cells (Wang *et al.* (2014), Lee *et al.* (2015), Haass *et al.* (2015), Su *et al.* (2015), Liu *et al.* (2016)). **Fig. 5.12(b)** shows the Raman spectra of as-prepared and annealed CZTS thin films. The most intense mode at 338 cm^{-1} and the weaker modes at 287 cm^{-1} and 369 cm^{-1} were closer to the reported Raman modes of CZTS (Yang *et al.* (2012), Mitzi *et al.* (2011), Wang and Demopoulos (2015), Sripan *et al.* (2017b), Ge *et al.* (2014), Tosun *et al.* (2013), Shavel *et al.* (2012)). Himmirch *et al.* reported the strongest peak at 338 cm^{-1} corresponding to the A_1 symmetry and it is related to the vibration mode of S atoms (Himmirch and Haeuseler (1991)). According to that, it confirms the presence of CZTS primary kesterite structure (338 cm^{-1}) and also secondary peak at 287 cm^{-1} to 288 cm^{-1} (**Fig. 5.12(b)**). Besides, an increase in their peak intensity indica-

tes a slight improvement in the crystallinity of the sample annealed at 450 °C. There was no evidence of impurities such as binary and ternary sulphide phases found in the Raman spectra of thin film annealed at 450 °C.

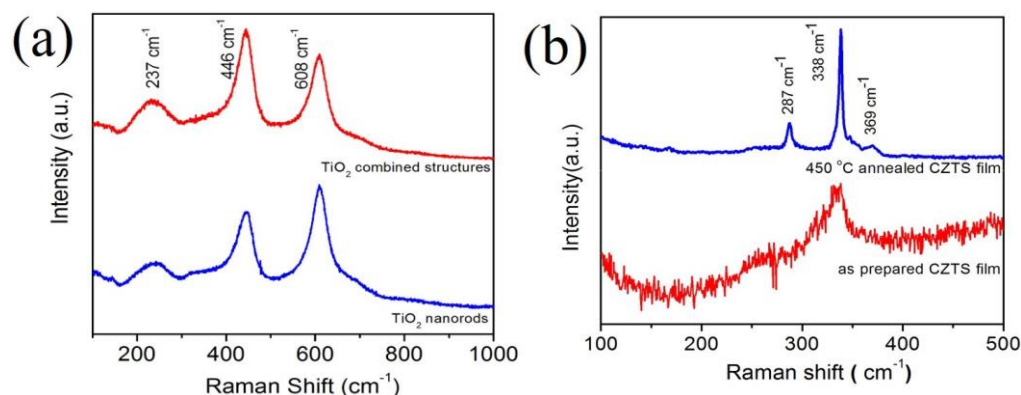


Figure 5.12: Raman spectra of (a) TiO₂ nanostructured films, (b) Cu₂Zn_{1.5}Sn_{1.2}S_{4.4} thin films.

5.3.4 X-ray Diffraction of TiO₂ Nanostructured and CZTS Thin Films

The crystal structure and phase confirmation of TiO₂ nanostructured films were examined by XRD (**Fig. 5.13(a)**). The diffraction peaks of TiO₂ nanostructured films were highly crystalline with the tetragonal rutile phase (JCPDS card no. 21-1272). Very strong rutile peaks were observed at 27.4° for TiO₂ nanorods and 36.1° for TiO₂ combined structures, which corresponds to the growth orientation of (101) and (110) respectively (Hendry *et al.* (2006), Zhu *et al.* (2012), Mali *et al.* (2016)). No other significant impurity peaks were detected in XRD results indicating that the fabricated samples were in pure rutile phase with the scanning Bragg's angles 2θ range from 20° to 90°. However, in TiO₂ nanorods film (110) peak was noticeably small as compared to the highest diffraction intensity of (101) peak. The highly intense (101) peak along with the small (002) peak in the nanorods film suggests that the rutile crystal grows with (101) plane parallel to the FTO substrate. Due to changes in the precursor volume (0.5 ml TTIP and 0.5 ml TBO) for TiO₂ combined structures, (110) peak had the highest intensity than (101) peak and it clearly shows, the microspheres grew well along (110) direction, together with nanorods.

The XRD pattern of as-prepared and annealed Cu₂Zn_{1.5}Sn_{1.2}S_{4.4} thin films are shown in **Fig. 5.13(b)**. The CZTS crystal structure is a tetrahedrally coordinated system,

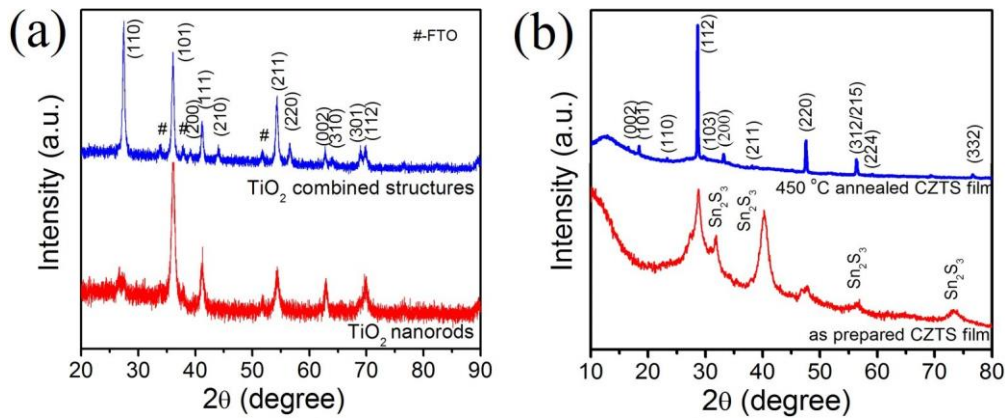


Figure 5.13: XRD patterns of (a) TiO₂ nanostructured films (b) Cu₂Zn_{1.5}Sn_{1.2}S_{4.4} thin films.

where each sulphur anion is bonded with four cations (Cu, Zn, and Sn) and each cation is bonded with four other sulphur anions. In general, phase purity of kesterite layers were difficult to confirm unambiguously, because of possible secondary chalcogenide phases such as Sn₂S₃, Cu₂S, ZnS, SnS and Cu₂SnS₃ which show very similar XRD patterns (Mitzi *et al.* (2011), Sripan *et al.* (2016), Dhakal *et al.* (2014), Muska *et al.* (2013), Zhou *et al.* (2011), Li *et al.* (2011)). As deposited Cu₂Zn_{1.5}Sn_{1.2}S_{4.4} film consists of Sn₂S₃ impurity peaks along with the CZTS phase. After annealing in the nitrogen atmosphere at 450 °C, Sn₂S₃ impurity phase peaks disappeared and peak intensity of the CZTS phase improved (see **Fig. 5.13(b)**). It can be inferred that, at and above this annealing temperature, all the elements in CZTS combined to form a single phase. Also, in stoichiometry adjusted CZTS polycrystalline film, the kesterite single phase formation occurring at lower annealing temperature with enhanced carrier concentrations (Sripan *et al.* (2016)).

5.3.5 Transmission Electron Microscopy Analysis of TiO₂ Nanostructured Films

Fig. 5.14(a,b) shows the high-resolution TEM images and fast Fourier transform (FFT) patterns of TiO₂ nanostructured film petals respectively. The upper inset image in **Fig. 5.14(a)** shows the lattice fringe at 1.47 Å, 2.19 Å and 3.25 Å indicating that the crystal was formed along the (001), (111) and (110) planes respectively. The corresponding FFT further verified that the nanorods were of highly oriented

crystalline nature. Also, these results indicated a good crystalline quality of the grown material, which is consistent with the XRD results as shown in **Fig. 5.13(a)**.

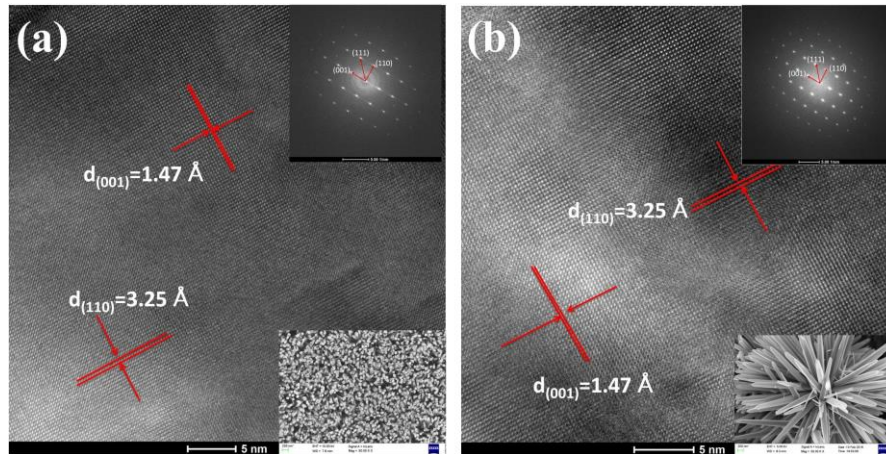


Figure 5.14: HRTEM and FFT (inset) images of (a) TiO₂ nanorods (b) TiO₂ combined structures.

5.3.6 Optical Properties of TiO₂ Nanostructured Films

The optical band gap of TiO₂ nanostructured films was calculated from Kubelka–Munk function $(kh\nu)^2$ versus incident photon energy plot and the values were obtained were 3.03 eV and 3.12 eV respectively (**Fig. 5.15(a,b)**). These results were in good agreement with the reported value of rutile phase TiO₂ nanostructures (Janotti *et al.* (2010)). The optical band gap of Cu₂Zn_{1.5}Sn_{1.2}S_{4.4} thin film was determined (**Fig. 5.13(c)**) by extrapolating the linear region of the plot of $(\alpha h\nu)^2$ versus photon energy $(h\nu)$ and taking the intercept on the $h\nu$ axis where $y=0$. The bandgap of the absorbers were determined at 1.75 eV and 1.63 eV for as prepared and 450 °C annealed thin films respectively. The decreased bandgap in 450 °C annealed film, may be attributed to the reduction in the number of unsaturated defects and the consumption of binary and ternary compound formations in CZTS. Room-temperature CL measurement was used to study the luminescent properties of TiO₂ nanostructured films, as shown in **Fig. 5.16(a,b)**. The obtained CL curves were deconvoluted into two peaks for TiO₂ nanorods, at 420 nm and 495 nm and for TiO₂ combined structures into three peaks, at 416 nm, 458 nm and 525 nm respectively.

The peaks at 420 nm and 416 nm correspond to the free exciton emission of titania groups near defects. The broad peaks from 465 nm to 525 nm were attributed to oxy-

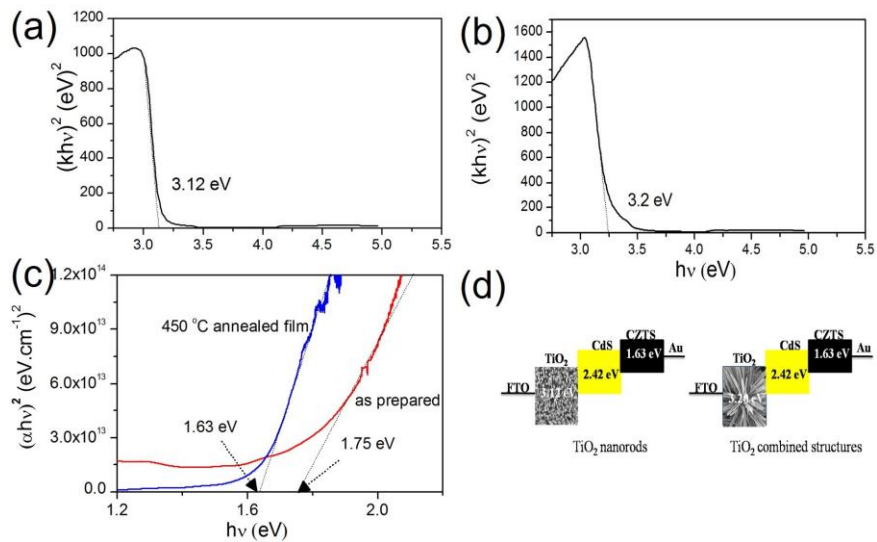


Figure 5.15: Spectral behaviour of $(kh\nu)^2$ versus photon energy for TiO₂ (a) nanorods, (b) combined structures, (C) $(\alpha h\nu)^2$ as a function of photon energy ($h\nu$) for CZTS thin films, (d) schematic band diagram of FTO/TiO₂ nanostructured films/CdS/CZTS/Au devices.

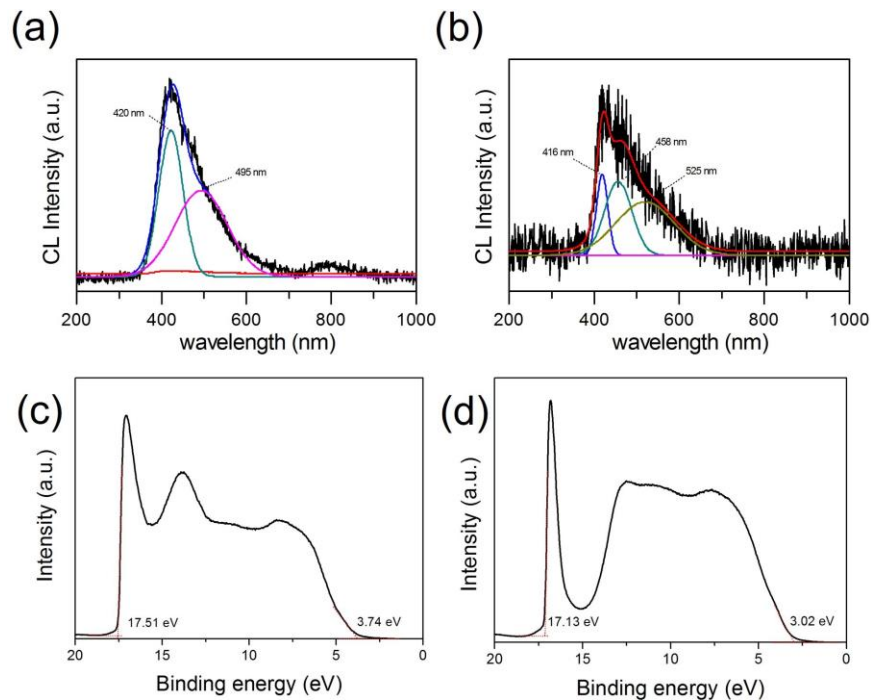


Figure 5.16: CL spectra of (a) TiO₂ nanorods, (b) TiO₂ combined structures and UPS spectra of (c) TiO₂ nanorods, (d) TiO₂ combined structures.

gen vacancies on the surface of TiO₂ nanostructures (Lei *et al.* (2001)). To further determine the charge transfer direction of the photo-generated electrons, UPS spectra were recorded for TiO₂ nanostructured films (**Fig. 5.16(c,d)**). The upper emission onset energy (E₁) and the lower emission onset energy (E₂) of secondary photoelectrons appeared at 17.51 eV and 3.74 eV for TiO₂ nanorods and 17.13 eV and 3.02 eV for TiO₂ combined structures respectively. Using the relation $\Phi = h\nu - (E_1 + E_2)$, the calculated valence band (VB) energies of these TiO₂ nanostructures were 7.45 eV and 7.11 eV respectively. Thus, the conduction band energies (E_c) of TiO₂ nanostructured films were estimated to be 4.42 eV and 3.99 eV from E_v-E_g relation.

5.3.7 Current-Voltage (I-V) Characteristics of the Fabricated (Au/CZTS/CdS/TiO Nanostructured films/FTO) Devices

Fig. 5.17(a,b) shows the PV performance of FTO/TiO₂ nanostructured films/CdS/CZTS/Au solar cells. The conversion efficiency η of TiO₂ nanorods based device was found to be 0.55 % with $I_{sc} = 4.2 \times 10^{-5}$ A, $V_{oc} = 0.10$ V and FF = 23.1 %. The device with TiO₂ combined nanostructures showed an efficiency of 1.45 % with $I_{sc} = 7.7 \times 10^{-5}$ A, $V_{oc} = 0.14$ V and FF = 26.5 % for the same active area of 0.196 mm². Both devices are shown in the inset of **Fig. 5.17(a,b)**.

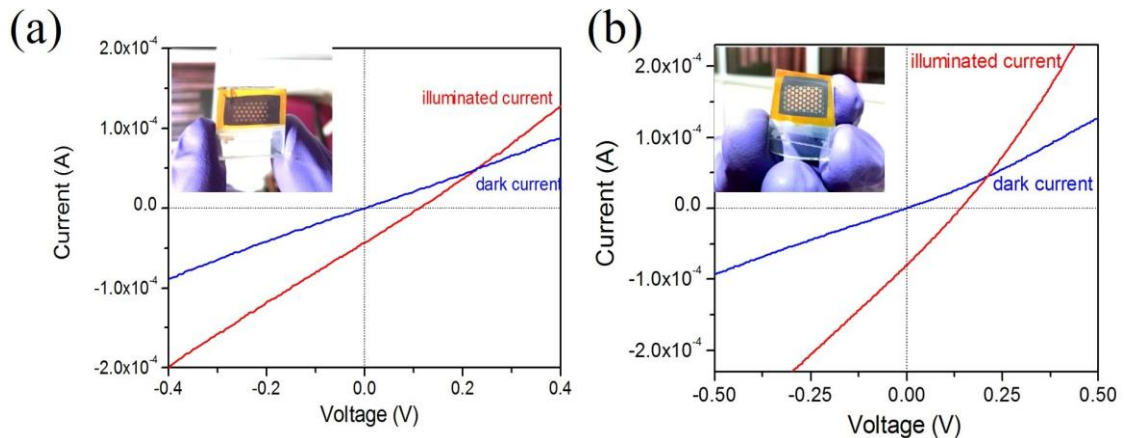


Figure 5.17: I-V curve of CZTS/CdS/TiO₂ nanostructured thin film solar cells (a) TiO₂ nanorods (b) TiO₂ combined structures.

The current increased sharply with the increase of reverse bias voltage, indicating the presence of junction between the CZTS/CdS/TiO₂ in both the devices. The com-

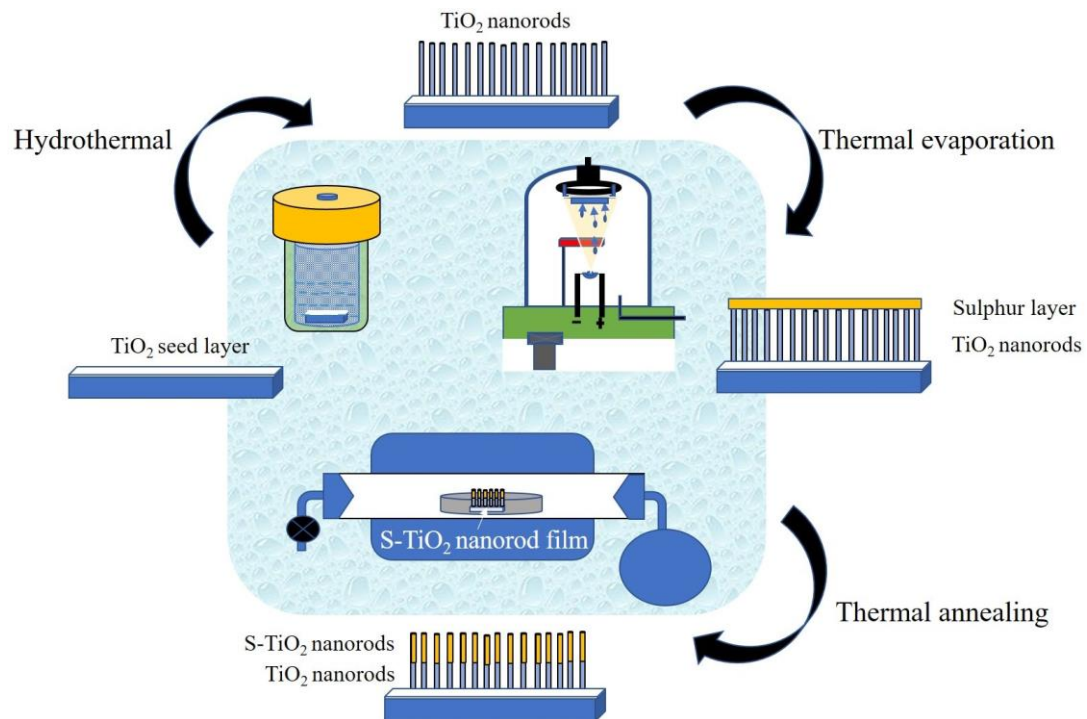
bined nanostructure TiO₂ films based PV cell facilitate more light trapping, increased light-harvesting ability than TiO₂ nanorods due to higher surface area and showed better PCE. Observed lower conversion efficiency of the fabricated devices may be due to the faster electron-hole recombination at the junctions, series resistance between the materials and sulphur deficiency at higher annealing temperatures (>500 °C) which affect FF of the devices.

5.4 Conclusions

In summary, highly oriented rutile phase of 1D-TiO₂ nanorods and 1D & 3D TiO₂ combined structures were successfully grown on the FTO substrate using the single-step hydrothermal process. The grown combined nanostructures were explored for their application in CZTS based solar cells. The device performance analysis showed that FTO/TiO₂ combined structures/CdS/CZTS/Au solar cells exhibited better PCE of $\eta = 1.45$ % compared to the solar cells with TiO₂ nanorods alone (0.55 %). The improvement in efficiency can be attributed to the multiple functions of the incorporated TiO₂ combined structures and sulfurization temperatures of CZTS. A detailed theoretical analysis is required to understand the charge transport mechanism in such structures. However, the present work will offer a new perspective for the performance enhancement of TiO₂/CZTS based solar cells. Also, this work opens up a challenging task for the fabrication of promising photoelectrodes (novel 1D and 3D combined nanostructures) in superstrate configured non-stoichiometric CZTS thin film solar cells. With appropriate design, the stoichiometry of materials and with theoretical understanding of transport mechanism, a high-performance PV device can be realized using the proposed architecture (Varadharajaperumal *et al.* (2017)).

Chapter 6

Toxic-free Surface Level Sulphur Doped 1D Ti-O_x-S_y Nanorods for Superstrate Heterojunction CZTS Thin Film Solar Cells



6.1 Introduction

Recently, a CIGS/Se based thin film solar cell was reported with the device efficiency of higher than 22 % (Bermudez and Perez-Rodriguez (2018)). However, due to the heavy restriction on safe usage, expensive and limited supply of In and Ga, there is a need to find a better alternate absorber with desirable optical bandgap (E_g) (~ 1.5 eV) for such solar cells (Ramasamy *et al.* (2012)). To overcome such issues, recently quaternary chalcogenide CZTS with similar properties as CIGS has attracted huge attention in order to develop a cost-effective and sustainable risk-free solar module (Guo *et al.* (2010), Ramasamy *et al.* (2012)). Moreover, it has the promising advantages of being a direct bandgap material with high absorption coefficient (10^4 cm⁻¹) and a tuneable optical band gap, which favourably helps to cover the entire solar energy spectrum (Kim *et al.* (2014)). Theoretically predicted power conversion of CZTS is 32.2 %, but the fabricated devices via solution and vacuum based methods showed PCEs of 12.6 % and 11.6 % respectively (Lee *et al.* (2015), Yan *et al.* (2018a)).

In CZTS heterojunction solar cells the charge carrier transport properties are greatly influenced by the band offsets position (at hetero-interface). Typically, an efficient CZTS thin film solar cells incorporate a high resistive thin buffer layer of n-CdS ($E_g=2.5$ eV). But, the toxic material and interface recombination (cliff-like band alignment) effects with the absorbing layer, causes an unfavourable condition for the n-type partner to produce an efficient and eco-friendly PV devices (Yan *et al.* (2018a)). At the same time, to enhance the light transmittance property in shorter wavelength regions, non-toxic wide bandgap semiconductors such as ZnO, TiO₂ and SnO were employed as a window layer (Wang *et al.* (2016a), Varadharajaperumal *et al.* (2017), McCandless and Birkmire (2000)). Among them, TiO₂ has been extensively studied as an electron extraction layer (EEL) owing to its interesting properties such as appropriate energy band alignment, chemical stability, low cost, and high charge carrier transportability. In addition, it is believed that the window layer made up of nanostructure may assist further to improve the device PCEs (Varadharajaperumal *et al.* (2017), Shaikh *et al.* (2018)). In other words, a photoanode made up of vertically aligned 1D-TiO₂ nanostructure (nanorods or nanowires and nanotubes) helps augment the visible region transparency and provide a shorter electron pathway (Feng *et al.* (2008), Wu *et al.* (2017)). Further, to utilize the 1D nanostructures, recently an increased number of investigations were carried out on superstrate (reverse type)

configured heterojunction PV devices Berruet *et al.* (2017), Tumbul *et al.* (2019), Yan *et al.* (2018a). As compared to conventional substrate type solar cells, it is proved that nanostructured superstrate solar devices helps to avoid the encapsulation complexity (top transparent electrode) and the charge carrier recombination loss. However, these type of PV devices were reported with lesser efficiency, while they have the potential to facilitating the electron injection and reduce the device module cost.

During last two decades, doping TiO₂ nanostructures with metals and non-metals has been an effective technique to manipulate its electronic band structure. Besides, these impurities will efficiently help extend the photoabsorption (from UV to the visible region) and also assist the injection and transport the photo excited electrons (Marschall and Wang (2014), Turkten *et al.* (2019)). At the same time, metal doping induces the material defects, as a resultant it reduces the TiO₂ photoelectron transportation (act as recombination centres), and thermal stability. To overcome such issue, recently doping non-metal elements such as nitrogen (N), sulphur (S), carbon (C), potassium (K), boron (B), iodine (I), fluorine (F) and phosphorous (P) have been explored as they have shown great potential to alter TiO₂ band offset (Wu *et al.* (2007), Czoska *et al.* (2008), Zhang *et al.* (2011), Pellegrin *et al.* (2011), Di Valentin and Pacchioni (2013), Marschall and Wang (2014), Szkoda *et al.* (2015), Ansari *et al.* (2016), Shin *et al.* (2016), Qin *et al.* (2017), Samsudin and Abd Hamid (2017)). Among them, S doped TiO₂ (S-TiO₂) has been considered as one of the most promising candidates owing to its dual ionic nature of S (anionic S²⁻ and cationic S^{4+/6+}) which helps to substitute both O and Ti ions in the TiO₂ crystal structure (Ohno *et al.* (2004), Li *et al.* (2014a)). To date, several research groups have deliberately made an attempt to attain S-TiO₂ via oxidative annealing of TiS₂, co-precipitation methods, sol-gel, hydrothermal and solvothermal process (Ohno *et al.* (2004), Czoska *et al.* (2008), Dunnill *et al.* (2009), Qin *et al.* (2017), Etghani *et al.* (2019)). However, the above mentioned synthesis routes have remained an open challenge in terms of producing film uniformity and implementing S atom into the TiO₂ matrix through toxin-free methods.

6.1.1 Objectives of the Work

The major scope of this present chapter is, to develop a non-toxic (H_2S free) way to dope (surface level) sulphur atoms into a 1D- TiO_2 nanostructure matrix via thermal evaporation followed by post-annealing ($350\text{ }^\circ\text{C}$, $450\text{ }^\circ\text{C}$ and $550\text{ }^\circ\text{C}$ for 30 mins); to fabricate a novel stoichiometry adjusted superstrate CZTS solar cells using surface-level sulphurated 1D-TNRs buffer layer and to study the photovoltaic effect of different temperature post annealed S-TNRs films employed heterojunction PV devices.

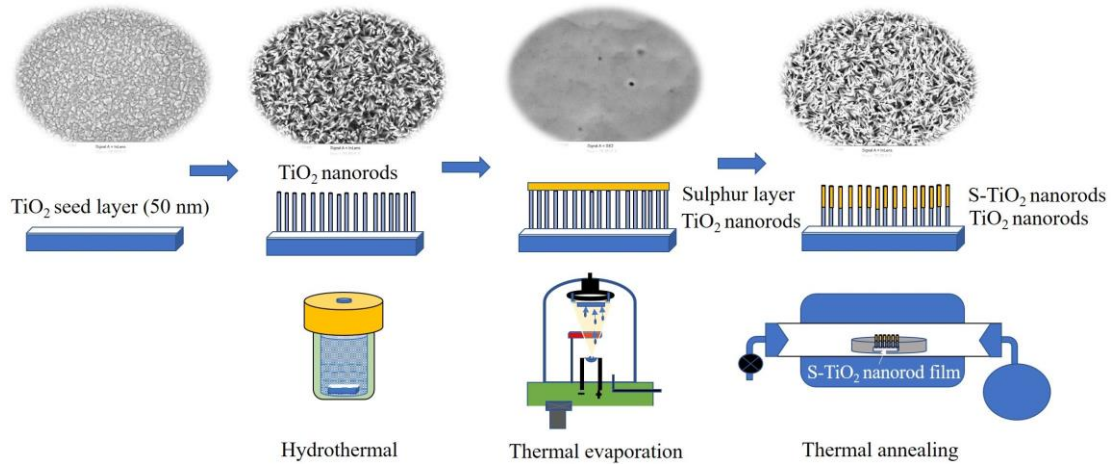


Figure 6.1: Schematic of the S-TNRs film synthesis process.

6.2 Experimental Details

6.2.1 Preparation of 1D TNRs and 1D S-TNRs Films

The methodology followed here is as follows:

- All the chemicals were used without further purification after procuring from the commercial sources. An array of the 1D-TNRs film was fabricated via the hydrothermal method as described in **Chapter 5**. To fabricate Sulphur doped TNRs films, the grown TNRs films were transferred into the thermal evaporation chamber for sulphur (50 nm) deposition at room temperature.



Figure 6.2: Sulphur layer (50 nm) coated on TiO_2 nanorods/FTO substrate.

- Following this, the S-layer (50 nm) coated 1D-TNRs films were kept inside the tubular furnace for sulphur diffusion process at 350 °C, 450 °C and 550 °C respectively for 30 mins. Importantly, the experiments were not carried out beyond 550 °C, due to degradation of the FTO substrate material (i.e., an increase in sheet resistance).

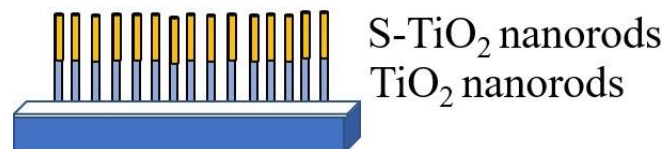


Figure 6.3: Post annealed S-TNRs/TNRs/FTO substrate.

6.2.1.1 Preparation of Non-Stoichiometric CZTS Absorbing Layer and Device Fabrication

- The stoichiometry adjusted CZTS ($\text{Cu}_2\text{Zn}_{1.5}\text{Sn}_{1.2}\text{S}_{4.4}$) alloy was prepared from pure Cu, Zn, Sn and S (99.999 % Alfa Aeser) elements by thermal molten technique as discussed in **Chapter 4**. Further to form p-n heterojunction, the prepared bulk alloy of CZTS was used to deposit CZTS thin films ($\sim 1 \mu\text{m}$) over S-TNRs/TNRs/FTO films at room temperature using the thermal evaporation method. The deposition parameters and other details were described in **Chapter 5**. Followed by this the top electrode Au (100 nm) was deposited using the thermal evaporation technique.

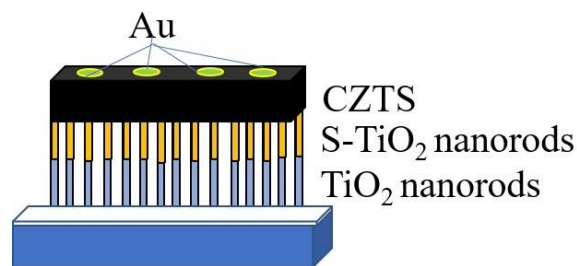


Figure 6.4: Schematic of Au/CZTS/S-TNRs/TNRs/FTO substrate hetero-interface device.

6.2.2 Characterization Techniques

The surface morphology studies with and without sulphurated TNRs films were carried out using FESEM. The doping concentrations of the deposited films were determined by EDS. The EDS spectra were recorded with ~ 10 nA beam current, 15 kV accelerating voltage at 8.5 mm working distance. The crystal structures of the synthesized films were examined by GIXRD using Cu $K\alpha$ source ($\lambda = 1.5405 \text{ \AA}$) with diffraction angle from 20° to 80° . Phase identification of TNRs and S-TNRs films were respectively characterized by Raman spectroscopy and XPS. The XPS core level high-resolution spectra were recorded from monochromatic Al $K\alpha$ X-ray (1486.6 eV) at a 10^{-9} Torr chamber vacuum. The measurement was carried out at an applied beam current of 10 mA and an acceleration voltage of 11 kV (110 W). To identify the doping depth of S atoms in TiO_2 matrix, an in-situ XPS depth profile experiment was carried out using Ar^+ ion at 4 kV accelerating voltage with 9 mm^2 etch area. The optical band gaps were calculated using UV-Vis DRS at room temperature with the spectral range of 250 nm-1000 nm. Current-voltage (I-V) performances of the fabricated devices were measured from a solar simulator under AM 1.5G.

6.3 Results and Discussion

6.3.1 The Surface Morphology and Compositional Analysis of Pristine TNRs and S-TNRs Thin Films

Fig. 6.7(a-d) shows the surface morphology of pristine TNRs and post annealed S-TNRs (350°C , 450°C , and 550°C) films. The FESEM micrographs clearly show the controlled growth of TNRs and S-TNRs over the FTO substrate. Also, it was observed that there were no prominent changes in their surface morphology as a function of calcinating temperatures (see **Fig. 6.7(a-d)**). The EDS analysis was carried out to quantify the atomic ratio of sulphur in post annealed S-TNRs samples (**Fig. 6.8(a-d)**). The film annealed at 350°C showed an increased elemental concentration of sulphur (0.41 %). On the other hand, when the annealing temperature exceeded 350°C , a reduced compositional ratio of sulphur in TiO_2 nanostructure (for 450°C was 0.29 % and for 550°C was 0.14 %) (**Fig. 6.8(b-d)**) was observed. This may be due to the sulphur degradation (above 350°C). However, the presence of sulphur concentration within the TiO_2 matrix was confirmed using EDS.

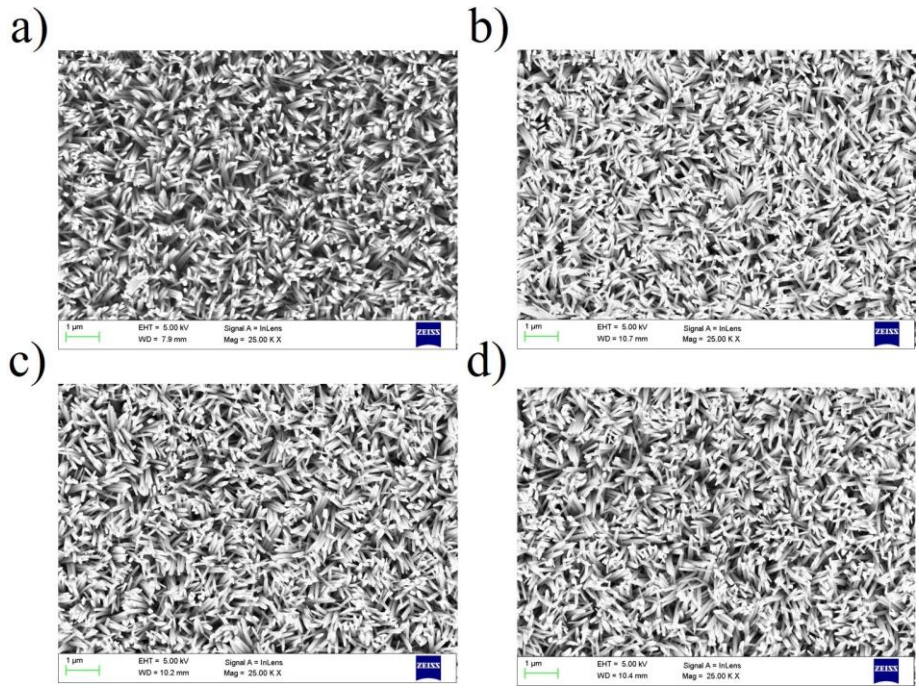


Figure 6.5: FESEM images of (a) Pristine TNRs, (b) 350 °C, (c) 450 °C and (d) 550 °C annealed S-TNRs thin films.

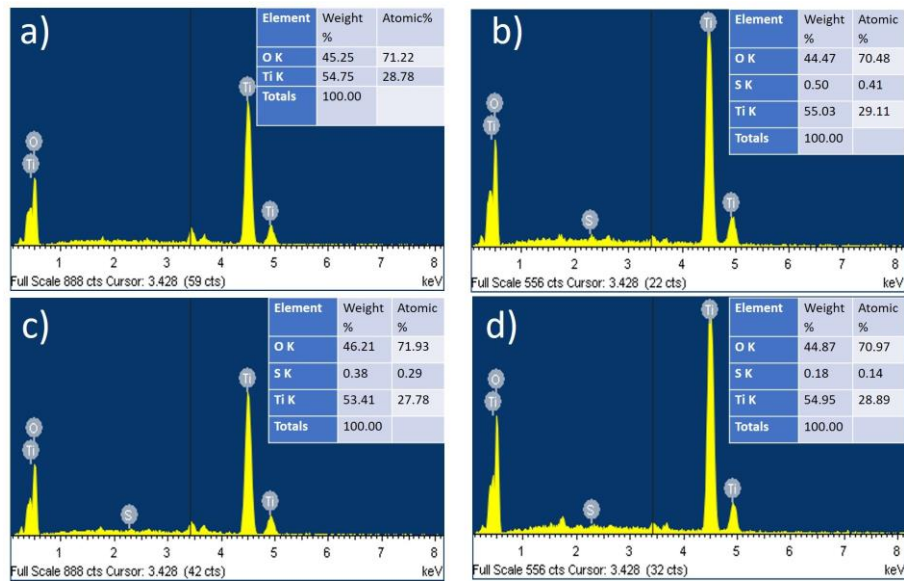


Figure 6.6: EDS analysis of (a) Pristine TNRs, (b) 350 °C, (c) 450 °C and (d) 550 °C annealed S-TNRs thin films.

6.3.2 The Crystal Structure and Phase Identification of Pristine TNRs and S-TNRs Thin Films

Raman spectroscopy was carried out to identify the crystal phases of pristine TNRs and post annealed S-TNRs thin films (**Fig. 6.9(a)**). Three major peaks were observed at 236.8 cm^{-1} , 444.3 cm^{-1} , and 608.9 cm^{-1} corresponding to Raman vibrational E_g and Ti–O stretch modes of rutile phase TiO_2 respectively (Frank *et al.* (2012)). It is indicated that there was no evidence of any impurity peaks and thermally diffused S-TNRs films ($350\text{ }^\circ\text{C}$, $450\text{ }^\circ\text{C}$ and $550\text{ }^\circ\text{C}$) also showed the same rutile TiO_2 crystal structure. Importantly, from the spectra, it was observed that the $350\text{ }^\circ\text{C}$ annealed S-TNRs film showed reduced peak intensities. Further, the XRD analysis was carried out to understand the crystal structure of the fabricated films. **Fig. 6.9(b)** shows the XRD of as-deposited and post annealed S-TNRs films. The obtained results confirmed that the pristine and post annealed S-TNRs films were in the pure rutile phase (JCPDS card no. 21-1272) (Zhu *et al.* (2017)). Upon increasing the annealing temperature, there was no significant shift in peak positions. Besides, it was noticed that the proposed methodology (sulphur deposition followed by annealing) does not affect the TiO_2 crystal structure. However, annealing at $350\text{ }^\circ\text{C}$ influenced the S-TNRs film diffraction peak intensities, which indicated the distribution of S atoms among the nanocrystal (**Fig. 6.9(c)**). In other words, only parts of the extrinsic doping caused slight changes in their crystal lattice. These results corroborated with Raman studies.

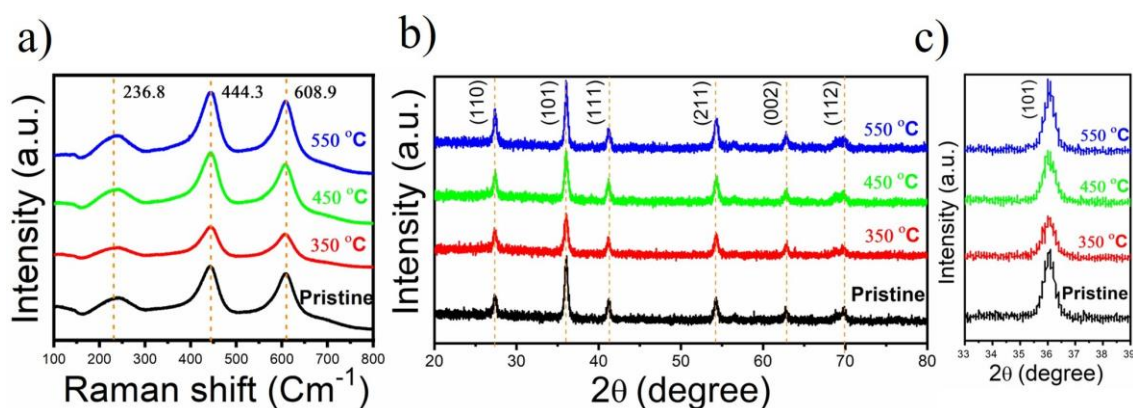


Figure 6.7: Pristine TNRs and post annealed S-TNRs thin films (a) Raman spectra, (b and c) XRD spectra.

6.3.3 The Chemical State Analysis of Pristine TNRs and S- TNRs Thin Films

The valence state of TNRs and S-TNRs films were examined by recording their XPS spectra (shown in **Fig. 6.10**). The recorded high-resolution XPS spectra (C 1s, Ti 2p, O 1s, and S 2p orbitals) of pristine and surface sulphureted TNRs films peaks were shift corrected to adventitious carbon (C-C) peak position (284.6 eV). The Ti 2p peaks obtained at the binding energies (BE) of 464.4 eV and 458 eV were attributed to Ti 2p_{1/2} and Ti 2p_{3/2} respectively. Also, no obvious peaks were observed at 454 eV, which indicates the absence of Ti-S bond in the TiO₂ lattice (**Fig. 6.10(a)**). The peak observed at 530.2 eV is attributed to the Ti-O-Ti bond. The presence of O-S bond at 532.5 eV provides convincing evidence of the incorporation of S atoms into the TiO₂ matrix (Ti-O-S) (**Fig. 6.10(b)**). Similarly, in 350 °C, 450 °C and 550 °C annealed S-TNRs films, S 2p ionization was observed at 169.37 eV and 168.4 eV (**Fig. 6.10(c)**), which were ascribed to the chemical states of S⁶⁺ and SO₄²⁻ ions anchored on the surface of TiO₂ nanorods respectively (Niu *et al.* (2013), Zhu *et al.* (2015)). Moreover, an increased S 2p peak intensity was evidently observed for 350 °C annealed S-TNRs film, which indicated the higher concentration of S atoms in the TNRs film.

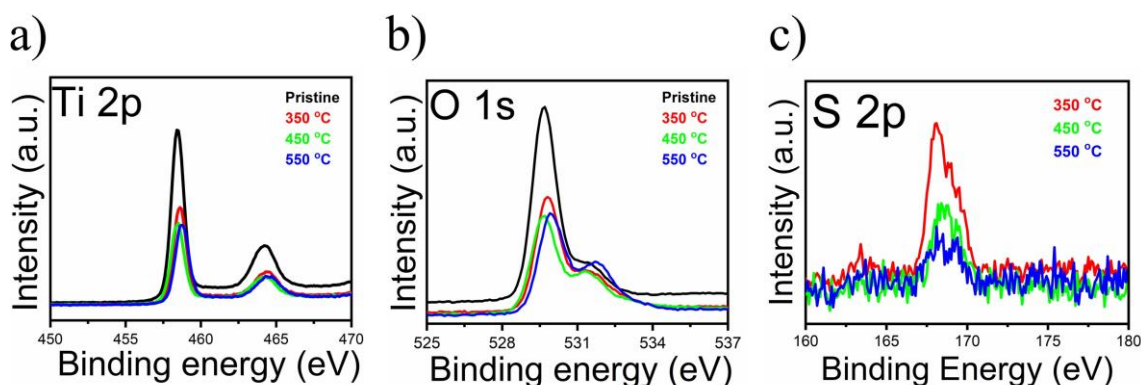


Figure 6.8: XPS high-resolution spectra of (a) Ti 2p, (b) O 1s and (c) S 2p orbitals.

6.3.4 The Optical Properties of Pristine TNRs and S-TNRs Thin Films

UV-Vis DRS was performed to study the optical properties of pristine TNRs and S-TNRs films (**Fig. 6.11**). The E_g of the specimens was calculated from the reflectance spectra, using Kubelka–Munk function $(kh\nu)^2$ vs incident photon energy. The pristine TNRs film exhibited a strong absorption band at 412 nm, corresponding optical band gap of 3.01 eV. The DRS spectra of 350 °C, 450 °C and 550 °C annealed S-TNRs films showed a slight red shift in their peak positions, corresponding to the calculated bandgap of 2.89 eV, 2.92 eV and 2.97 eV respectively. The shift may be attributed to a reduction in the electron transition energy caused by additional intermediate electronic bands of TiO_2 (Ohno *et al.* (2004)).

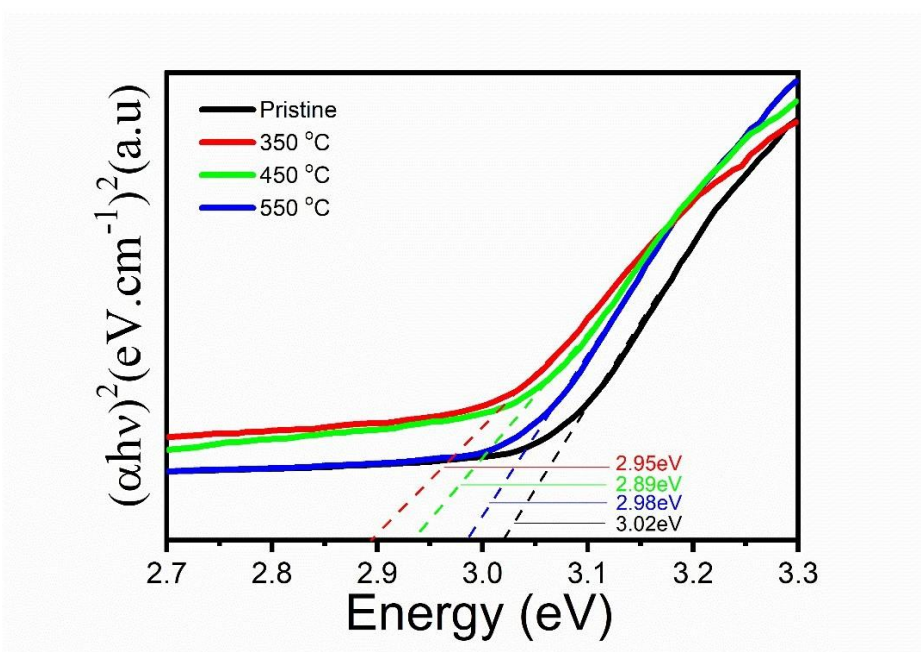


Figure 6.9: UV-Vis DRS spectra of as-deposited and post annealed films.

6.3.5 The Lateral Doping Concentration Studies of 350 °C Annealed S-TNRs Film

To determine the lateral doping concentration, the cross-sectional FESEM image with EDS analysis was carried out on 350 °C annealed S-TNRs thin film (**Fig. 6.12**) samples. It can be seen that the sulphurated TNRs diameter ~ 60 nm and length $\sim 2.5 \mu\text{m}$, which was the same as that for an undoped TNRs film. The EDS spectra

were recorded at four localized regions along the depth of the film as shown in **Fig. 6.12**. The spectrum measured at the film surface (position 1) showed the S element concentration of 0.39 %. The S concentrations as observed at positions 2 and 3 were 0.28 % and 0.08 % respectively. The spectrum measured at position 4 (~ 500 nm depth) showed only the presence of Ti and O elements, not S element, which revealed that there was no diffusion of S atoms below that region of TNRs film. These results confirmed that doping had taken place up to ~ 500 nm depth of the nonorods from the top. Further, to confirm the vertical compositional profile of sulphur present (depth

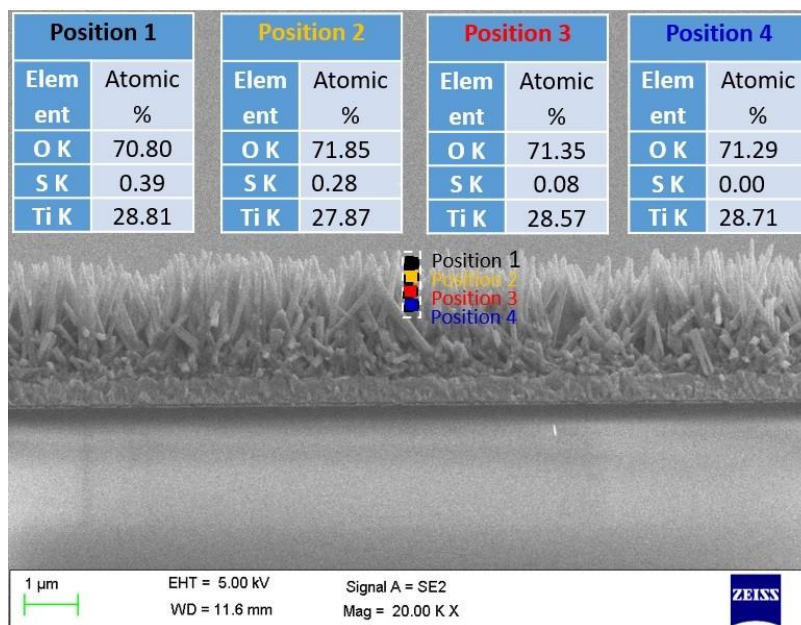


Figure 6.10: Cross-sectional FESEM image of elemental compositions of 350 °C annealed S-TNRs film.

of sulphur doping) in the TNRs matrix, the destructive depth profiling XPS analysis was carried out using monoatomic argon (Ar^+) ion as etching source. **Fig. 6.13(a)** shows the schematic of the depth profile experiment. Initially, the 350 °C annealed S-TNRs film surface was etched with Ar^+ ion beam for 30 sec. Then the film was depth profiled up to 1200 sec to identify the lateral doping concentration of sulphur in TNRs film. **Fig. 6.13(b-d)** shows an evolution in etching time (30 sec to 1200 sec) XPS spectra of Ti 2p, O 1s, and S 2p orbitals respectively. The result indicated that with increasing sputtering time, S 2p peaks gradually decreased and disappeared after 1200 sec, which is consistent with cross-sectional EDS analysis (**Fig. 6.12**).

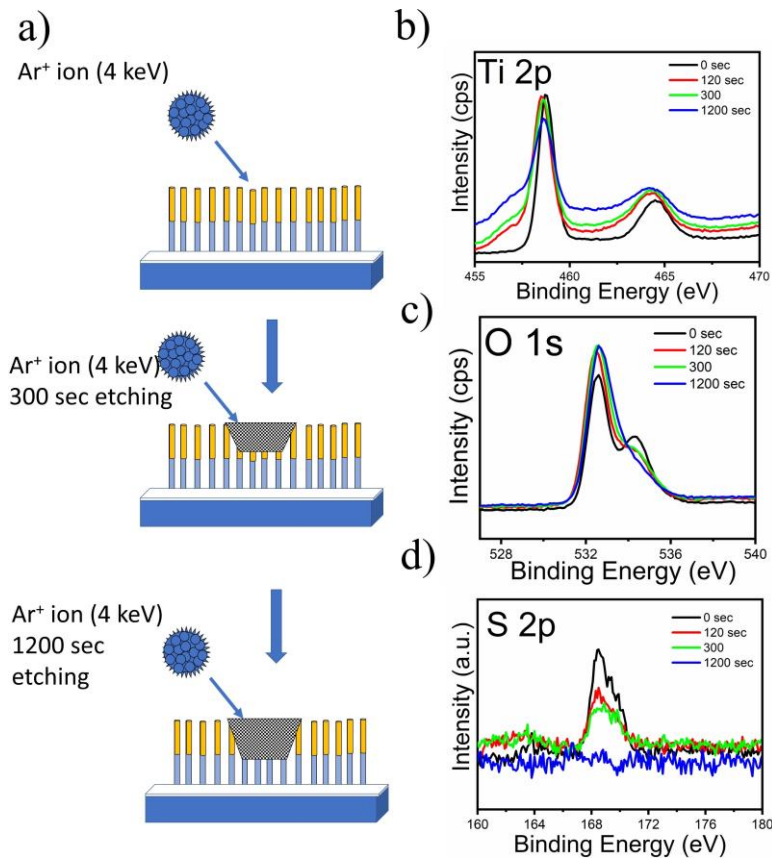


Figure 6.11: (a) Schematic of destructive XPS depth profiling, evaluation in etching cycles XPS spectra of (b) Ti 2p, (c) O 1s and (d) S 2p orbitals.

6.3.6 The Current-Voltage Characteristics of Fabricated Heterojunction Devices

To fabricate the pristine TNRs/CZTS and post annealed S-TNRs/CZTS heterojunction devices, the thermally evaporated CZTS (absorber) thin film was used and its materials and optical properties were described in **Chapter 4**. **Fig. 6.14(a-d)** show the photo current-voltage (I-V) performance of the fabricated thin films devices. The I_{sc} of the fabricated devices increased from 1.59×10^{-4} A to 5.54×10^{-4} A and the V_{oc} increased from 0.39 V to 0.59 V. The device fabricated with 350 °C annealed S-TNRs/CZTS showed a higher power conversion efficiency of $\eta = 3.05$ % ($I_{sc} = 5.54 \times 10^{-4}$ A, $V_{oc} = 0.59$ V and FF =34 %) compared to other devices (**Table 1**).

Table 6.1: The efficiency of fabricated PV devices.

Device	I_{sc} (A)	V_{oc} (V)	FF (%)	Efficiency η (%)
Pristine	1.59e-4	0.39	16	0.32
350°C	5.54e-4	0.59	34	3.05
450°C	3.19e-4	0.43	38	1.66
550°C	2.78e-4	0.38	25	0.85

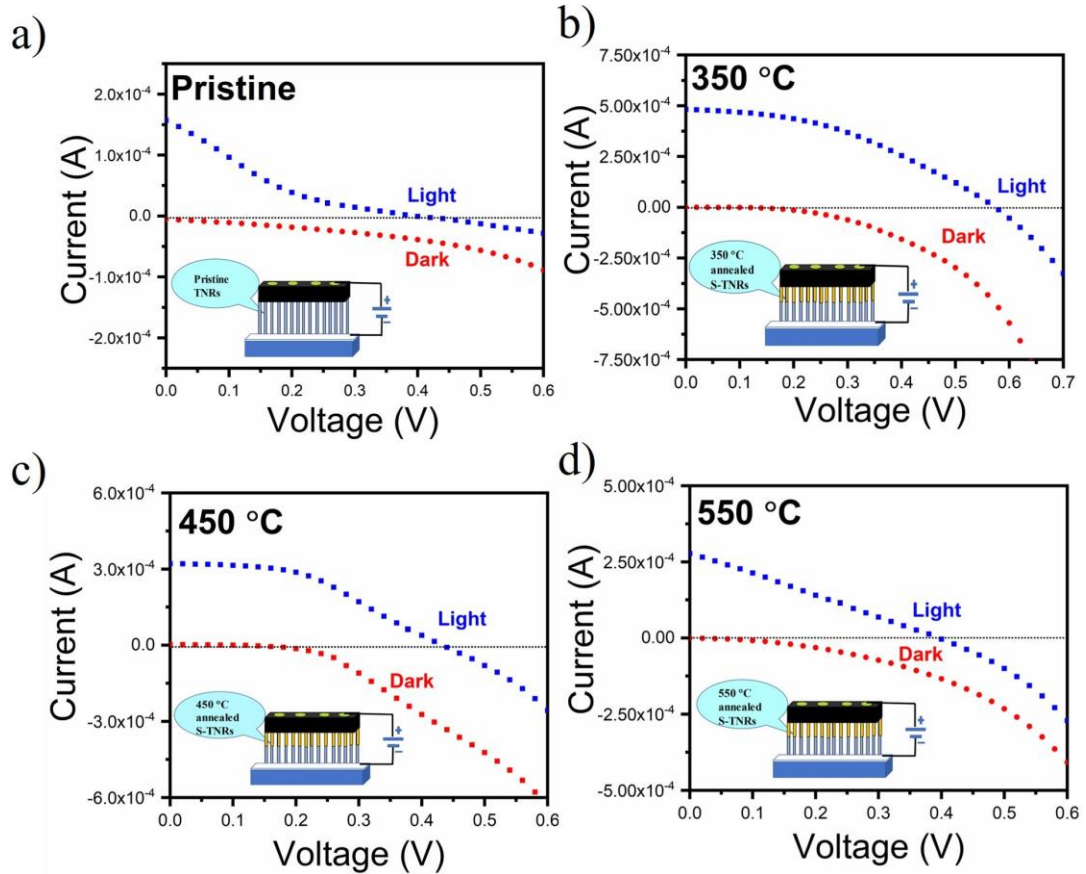


Figure 6.12: Photo I-V characteristics of (a) Pristine TNRs/CZTS, (b) 350 °C, (c) 450 °C and (d) 550 °C annealed S-TNRs/CZTS thin films heterojunction devices.

These results clearly show that 350 °C annealed S-TNRs film is preferable to dope sulphur atoms in the TiO_2 lattice, leading to band bending for better electron transportation. Also, its increased I_{sc} and V_{oc} indicated the enhanced electrons pathway and reduced recombination. However, it can be inferred that at above the 350 °C an-

ealing temperature, the device performances were degraded considerably which may be due to the sulphur deficiency and interface charge carrier recombination.

6.4 Conclusions

In summary, a facile non-toxic way of surface-level (shallow level) doping of sulphur atoms into 1D-TNRs via thermal evaporation followed by the post-annealing process is demonstrated in this chapter. In the post annealed S-TNRs films, no significant structural and surface morphological changes were observed from standard characterization techniques such as XRD, Raman, and FESEM. Interestingly, the formation of the $\text{Ti-O}_x\text{-S}_y$ phase on the surface of TNRs (for the sulphurated film at 350 °C) was observed from XPS. Further, depth profiling XPS and cross-sectional FESEM with EDS analysis confirm the depth of S element doping in TiO_2 matrix. Besides, doping S atoms into the TiO_2 matrix with different annealing temperatures (350 °C to 550 °C) proved to be an effective way to narrow down the bandgap of TNRs films. More importantly, due to S-modification, there is a slight absorbance in the visible region and thus it helps develop Cd free buffer layer in CZTS thin film solar cells. The enhanced photovoltaic performance (3.05 %) was measured for 350 °C sulphurated TNRs/CZTS devices. Finally, present work will offer a new perspective way to precisely dope S atoms (surface level) into nanostructured photoanode for solar cell applications.

Chapter 7

Conclusions and Future Scope

7.1 Conclusions

Chapter 1 summarized the significance of solar energy, material selection, basics of chalcogenide (CdTe and CZTS), and operating mechanism of superstrate type thin film solar cells. Also it provides, a thorough literature survey on the current status of CdTe and CZTS thin film solar cells. **Chapter 2** described the experimental methods and characterization techniques used to design and develop the superstrate thin film solar cells. In order to prepare the CZTS alloy and thin film, thermal molten technique was followed by thermal evaporation. RF magnetron sputtering was used to deposit (ZnO and TiO₂) seed layers and CdS (thin film) buffer layer. Hot plate and hydrothermal methods were used to synthesise 1D-ZnO (nanorods and nanotubes) and 1D & 3D TiO₂ nanostructured (nanorods and microspheres with nanorods) films. Thermal evaporation technique was used to deposit the absorbing layers of CdTe and CZTS. Also, it was respectively used for the deposition of S layer, organic hole transport layer CuPc, and top electrode Au. CBD and spin coating techniques were used to decorate the CdS layer on top of 1D & 3D TiO₂ nanostructures and to deposit PEDOT:PSS layer respectively. FESEM and AFM were used to study the topographical information of the deposited films. XRD and TEM were used to identify the crystallographic studies of the prepared thin films. The material phase and oxidation state (surface and depth) of the fabricated films were studied using Raman and XPS. Optical properties of the synthesised materials were characterized by UV-DRS and CL spectroscopy. The chemical composition of CZTS and S-TNRs were studied using EDS analysis. To identify the band offset position (Φ and V_{bm}) of the fabricated films,

UPS technique was used in the present thesis work. The photovoltaic response was recorded using Solar simulator under AM 1.5G.

Chapter 3 investigated the effect of two hole transporting layers (CuPc and PEDOT:PSS) in CdS/CdTe thin film planar heterojunction solar cells. Due to the effective transportation of charge carriers, the device designed with CuPc/PEDOT:PSS showed the higher conversion efficiency (2.74 %) than PEDOT:PSS device alone (1.25 %). This strategy of incorporating two hole transport layers might offer an effective approach to enhance the conversion efficiency of CdTe PV device.

Chapter 4 addressed the transformation process of ZNRs to ZNTs by varying Zinc reactant concentration (25mM:25mM to 175mM:175mM) using single step hot plate technique. The grown nanostructures were utilized to fabricate the hetero-interfaced ZNRs/CZTS and ZNTs/CZTS solar cells. It was shown that a higher photocurrent resulted due to ZNTs incorporated in CZTS film.

Chapter 5 described the growth process of highly oriented rutile phase 1D-TiO₂ nanorods and 3D-TiO₂ combined structures on top of FTO substrate using single-step hydrothermal process. The grown nanostructures were examined for their application in CZTS superstrate solar cells. It was seen that a higher conversion efficiency resulted for the combined nanostructured device (1.45 %) compared to 1D-TiO₂ nanorods alone (0.55 %).

Chapter 6 described a shallow level (surface level) doping of sulphur atoms into 1D-TNRs attained via thermal evaporation followed by the post-annealing process. Then, the fabricated S-TNRs were evaluated for CZTS photovoltaic applications. Due to the higher concentration of S atoms in TiO₂ matrix, an enhanced photovoltaic performance (3.05 %) was recorded for 350 °C sulphurated TNRs/CZTS device. Also, the proposed technique offered to develop Cd free buffer layer and control the doping depth of S atom in any desired nanostructured photoanodes for solar cell applications.

7.2 Future Scope

In the present thesis, we have designed and investigated the role of two electron and hole transport layers in planar heterojunction superstrate CdS/CdTe solar cells. Further studies can be carried out to enhance the V_{oc} of the device by engineering the energy band of HTLs (organic and inorganic materials). Also, the window layer (metal oxide) made up of 1D nanostructures may help reduce the diffusion losses of electrons towards the electrodes. The performance of stoichiometry adjusted CZTS superstrate thin film solar cells can be further improved by incorporating Se atoms in the CZTS compound which enhances the absorption co-efficient. Moreover, in the present work the absorbing layer was deposited by evaporation method. However, the solution processed CZTS deposition may assist to sensitize the material over the surface of nanostructured window layer to achieve higher efficiency. Also, ZnO and TiO₂ nanostructured (1D & 3D) window layers can be doped with suitable metal ions for the effective separation of photogenerated charge carriers. In addition, there is a lot of scope for theoretical modelling and simulation in understanding the transport mechanism in these types of superstrate, heterostructure inorganic solar cells. This will further help in improving the design and selecting the appropriate materials to build cost effective, large area and high performance organic/inorganic photovoltaic devices.

Bibliography

Abbe, G. and H. Smith (2016). Technological development trends in solar-powered aircraft systems. *Renewable and Sustainable Energy Reviews*, **60**, 770–783.

Ahmed, S., K. B. Reuter, O. Gunawan, L. Guo, L. T. Romankiw, and H. Deligianni (2012). A high efficiency electrodeposited $\text{Cu}_2\text{ZnSnS}_4$ solar cell. *Advanced Energy Materials*, **2**(2), 253–259.

Akhtar, K., S. A. Khan, S. B. Khan, and A. M. Asiri, Scanning electron microscopy: Principle and applications in nanomaterials characterization. *In Handbook of Materials Characterization*. Springer, 2018, 113–145.

Al-Gaashani, R., S. Radiman, A. Daud, N. Tabet, and Y. Al-Douri (2013). XPS and optical studies of different morphologies of ZnO nanostructures prepared by microwave methods. *Ceramics International*, **39**(3), 2283–2292.

Aldakov, D., A. Lefrançois, and P. Reiss (2013). Ternary and quaternary metal chalcogenide nanocrystals: synthesis, properties and applications. *Journal of Materials Chemistry C*, **1**(24), 3756–3776.

Altamura, G. (2014). *Development of CZTSSe thin films based solar cells*. Ph.D. thesis.

Ansari, S. A., M. M. Khan, M. O. Ansari, and M. H. Cho (2016). Nitrogen Doped Titanium Dioxide (N-Doped TiO_2) for Visible Light Photocatalysis. *New Journal of Chemistry*, **40**(4), 3000–3009.

Anta, J. A., E. Guillén, and R. Tena-Zaera (2012). ZnO-based dye-sensitized solar cells. *The Journal of Physical Chemistry C*, **116**(21), 11413–11425.

- Bai, Z., J. Yang, and D. Wang** (2011). Thin film CdTe solar cells with an absorber layer thickness in micro and sub-micrometer scale. *Applied Physics Letters*, **99**(14), 143502.
- Baig, H., H. Kanda, A. M. Asiri, M. K. Nazeeruddin, and T. Mallick** (2020). Increasing efficiency of perovskite solar cells using low concentrating photovoltaic systems. *Sustainable Energy & Fuels*.
- Barkhouse, D. A. R., O. Gunawan, T. Gokmen, T. K. Todorov, and D. B. Mitzi** (2012). Device characteristics of a 10.1% hydrazine-processed $\text{Cu}_2\text{ZnSn}(\text{Se},\text{S})_4$ solar cell. *Progress in Photovoltaics: Research and Applications*, **20**(1), 6–11.
- Bauhuis, G., P. Mulder, E. Haverkamp, J. Huijben, and J. Schermer** (2009). 26.1% thin-film GaAs solar cell using epitaxial lift-off. *Solar Energy Materials and Solar Cells*, **93**(9), 1488–1491.
- Baykara, M. Z. and U. Schwarz**, Atomic force microscopy: Methods and applications. *In Encyclopedia of Spectroscopy and Spectrometry*. Elsevier, 2017.
- Beard, M. C.** (2011). Multiple exciton generation in semiconductor quantum dots. *The Journal of Physical Chemistry Letters*, **2**(11), 1282–1288.
- Bergman, J. I., J. Chang, Y. Joo, B. Matinpour, J. Laskar, N. M. Jokerst, M. A. Brooke, B. Brar, and E. Beam** (1999). Rtd/cmos nanoelectronic circuits: thin-film InP-based resonant tunneling diodes integrated with CMOS circuits. *IEEE Electron Device Letters*, **20**(3), 119–122.
- Bermudez, V. and A. Perez-Rodriguez** (2018). Understanding the cell-to-module efficiency gap in Cu (In, Ga) (S, Se)₂ photovoltaics scale-up. *Nature Energy*, **3**(6), 466.
- Berruet, M., Y. Di Iorio, C. Pereyra, R. Marotti, and M. Vázquez** (2017). Highly-efficient superstrate $\text{Cu}_2\text{ZnSnS}_4$ solar cell fabricated low-cost methods. *physica status solidi (RRL)–Rapid Research Letters*, **11**(8), 1700144.
- Bhandari, K. P., H. Choi, S. Jeong, H. Mahabaduge, and R. J. Ellingson** (2014). Determination of heterojunction band offsets between CdS bulk and PbS

quantum dots using photoelectron spectroscopy. *Applied Physics Letters*, **105**(13), 131604.

Bhattacharya, S. and S. John (2019). Beyond 30% conversion efficiency in silicon solar cells: A numerical demonstration. *Scientific reports*, **9**(1), 1–15.

Britt, J. and C. Ferekides (1993). Thin-film CdS/CdTe solar cell with 15.8% efficiency. *Applied physics letters*, **62**(22), 2851–2852.

Bumrah, G. S. and R. M. Sharma (2016). Raman spectroscopy–basic principle, instrumentation and selected applications for the characterization of drugs of abuse. *Egyptian Journal of Forensic Sciences*, **6**(3), 209–215.

Bunaciu, A. A., E. gabriela Udriștioiu, and H. Y. Aboul-Enein (2015). X- ray diffraction: Instrumentation and applications. *Critical Reviews in Analytical Chemistry*, **45**(4), 289–299.

Burungale, V., V. Satale, A. More, K. Sharma, A. Kamble, J. Kim, and P. Patil (2016). Studies on effect of temperature on synthesis of hierarchical TiO₂ nanostructures by surfactant free single step hydrothermal route and its photo-electrochemical characterizations. *Journal of colloid and interface science*, **470**, 108–116.

Chen, S., X. Gong, A. Walsh, and S.-H. Wei (2009). Crystal and electronic band structure of Cu₂ZnSnX₄ (X= S and Se) photovoltaic absorbers: First-principles insights. *Applied Physics Letters*, **94**(4), 041903.

Chen, Y.-H., Y.-M. Shen, S.-C. Wang, and J.-L. Huang (2014). Fabrication of one-dimensional ZnO nanotube and nanowire arrays with an anodic alumina oxide template via electrochemical deposition. *Thin Solid Films*, **570**, 303–309.

Cho, J. W., A. Ismail, S. J. Park, W. Kim, S. Yoon, and B. K. Min (2013). Synthesis of Cu₂ZnSnS₄ thin films by a precursor solution paste for thin film solar cell applications. *ACS applied materials & interfaces*, **5**(10), 4162–4165.

Chu, D., Y. Masuda, T. Ohji, and K. Kato (2010). Formation and photocatalytic application of ZnO nanotubes using aqueous solution. *Langmuir*, **26**(4), 2811–2815.

- Chu, D., A. Younis, and S. Li** (2012). Direct growth of TiO₂ nanotubes on transparent substrates and their resistive switching characteristics. *Journal of Physics D: Applied Physics*, **45**(35), 355306.
- Cibira, G.** (2018). Relations among photovoltaic cell electrical parameters. *Applied Surface Science*, **461**, 102–107.
- Colgan, M., B. Djurfors, D. Ivey, and M. Brett** (2004). Effects of annealing on titanium dioxide structured films. *Thin Solid Films*, **466**(1-2), 92–96.
- Copeland, A. W., O. D. Black, and A. Garrett** (1942). The photovoltaic effect. *Chemical reviews*, **31**(1), 177–226.
- Czoska, A., S. Livraghi, M. Chiesa, E. Giamello, S. Agnoli, G. Granozzi, E. Finazzi, C. D. Valentin, and G. Pacchioni** (2008). The nature of defects in fluorine-doped TiO₂. *The Journal of Physical Chemistry C*, **112**(24), 8951–8956.
- Darr, J. A., J. Zhang, N. M. Makwana, and X. Weng** (2017). Continuous hydrothermal synthesis of inorganic nanoparticles: applications and future directions. *Chemical reviews*, **117**(17), 11125–11238.
- Deng, X. and E. A. Schiff** (2003). Amorphous silicon based solar cells.
- Dhakai, T. P., C.-Y. Peng, R. R. Tobias, R. Dasharathy, and C. R. Westgate** (2014). Characterization of a CZTS thin film solar cell grown by sputtering method. *Solar Energy*, **100**, 23–30.
- Dhawale, D. S., A. Ali, and A. C. Lokhande** (2019). Impact of various dopant elements on the properties of kesterite compounds for solar cell applications: a status review. *Sustainable Energy & Fuels*, **3**(6), 1365–1383.
- Di Valentin, C. and G. Pacchioni** (2013). Trends in non-metal doping of anatase TiO₂: B, C, N and F. *Catalysis today*, **206**, 12–18.
- Dou, J., Y. Li, F. Xie, X. Ding, and M. Wei** (2016). Metal–organic framework derived hierarchical porous anatase TiO₂ as a photoanode for dye-sensitized solar cell. *Crystal Growth & Design*, **16**(1), 121–125.

- Du, X., Z. Chen, F. Liu, Q. Zeng, G. Jin, F. Li, D. Yao, and B. Yang** (2016). Improvement in open-circuit voltage of thin film solar cells from aqueous nanocrystals by interface engineering. *ACS applied materials & interfaces*, **8**(1), 900–907.
- Dunnill, C. W., Z. A. Aiken, A. Kafizas, J. Pratten, M. Wilson, D. J. Morgan, and I. P. Parkin** (2009). White light induced photocatalytic activity of sulfur-doped TiO₂ thin films and their potential for antibacterial application. *Journal of Materials Chemistry*, **19**(46), 8747–8754.
- Ellis, B. and T. S. Moss** (1970). Calculated efficiencies of practical GaAs and Si solar cells including the effect of built-in electric fields. *Solid-State Electronics*, **13**(1), 1–24.
- Elumalai, N. K. and A. Uddin** (2016). Open circuit voltage of organic solar cells: an in-depth review. *Energy & Environmental Science*, **9**(2), 391–410.
- Etghani, S. A., E. Ansari, and S. Mohajezadeh** (2019). Evolution of large area TiS₂-TiO₂ heterostructures and S-doped TiO₂ nano-sheets on titanium foils. *Scientific reports*, **9**(1), 1–14.
- Fan, K., W. Zhang, T. Peng, J. Chen, and F. Yang** (2011). Application of TiO₂ fusiform nanorods for dye-sensitized solar cells with significantly improved efficiency. *The Journal of Physical Chemistry C*, **115**(34), 17213–17219.
- Fang, Z., X. C. Wang, H. C. Wu, and C. Z. Zhao** (2011). Achievements and challenges of CdS/CdTe solar cells. *International Journal of Photoenergy*, **2011**.
- Feng, X., K. Shankar, O. K. Varghese, M. Paulose, T. J. Latempa, and C. A. Grimes** (2008). Vertically aligned single crystal TiO₂ nanowire arrays grown directly on transparent conducting oxide coated glass: synthesis details and applications. *Nano letters*, **8**(11), 3781–3786.
- Feng, Z., K. Komvopoulos, I. Brown, and D. Bogy** (1993). Effect of graphitic carbon films on diamond nucleation by microwave-plasma-enhanced chemical-vapor deposition. *Journal of applied physics*, **74**(4), 2841–2849.
- Ferekides, C. S., D. Marinskiy, V. Viswanathan, B. Tetali, V. Palekis, P. Selvaraj, and D. Morel** (2000). High efficiency CSS CdTe solar cells. *Thin Solid Films*, **361**, 520–526.

Fraas, L. M., History of solar cell development. *In Low-Cost Solar Electric Power*. Springer, 2014, 1–12.

Frank, O., M. Zukalova, B. Laskova, J. Kürti, J. Koltai, and L. Kavan (2012). Raman spectra of titanium dioxide (anatase, rutile) with identified oxygen isotopes (16, 17, 18). *Physical Chemistry Chemical Physics*, **14**(42), 14567–14572.

Gao, T. and T. Wang (2005). Synthesis and properties of multipod-shaped ZnO nanorods for gas-sensor applications. *Applied Physics A*, **80**(7), 1451–1454.

Ge, J., J. Chu, J. Jiang, Y. Yan, and P. Yang (2014). Characteristics of In- substituted CZTS thin film and bifacial solar cell. *ACS applied materials & interfaces*, **6**(23), 21118–21130.

Gielen, D., F. Boshell, D. Saygin, M. D. Bazilian, N. Wagner, and R. Gorini (2019). The role of renewable energy in the global energy transformation. *Energy Strategy Reviews*, **24**, 38–50.

Goetzberger, A., C. Hebling, and H.-W. Schock (2003). Photovoltaic materials, history, status and outlook. *Materials Science and Engineering: R: Reports*, **40**(1), 1–46.

Gorji, N. E. and M. Houshmand (2013). Carbon nanotubes application as buffer layer in Cu (In, Ga)Se₂ based thin film solar cells. *Physica E: Low-dimensional Systems and Nanostructures*, **50**, 122–125.

Grätzel, M. and B. O'Regan (1991). A low-cost, high-efficiency solar cell based on dye-sensitized colloidal TiO₂ films. *Nature*, **353**(6346), 737–740.

Green, M. A. (2017). Corrigendum to ‘solar cell efficiency tables (version 49)’ [prog. photovolt: Res. appl. 2017; 25: 3–13]. *Progress in Photovoltaics: Research and Applications*, **25**(4), 333–334.

Guo, Q., G. M. Ford, W.-C. Yang, B. C. Walker, E. A. Stach, H. W. Hill-house, and R. Agrawal (2010). Fabrication of 7.2% efficient CZTSSe solar cells using CZTS nanocrystals. *Journal of the American Chemical Society*, **132**(49), 17384–17386.

- Gür, T. M.** (2018). Review of electrical energy storage technologies, materials and systems: challenges and prospects for large-scale grid storage. *Energy & Environmental Science*, **11**(10), 2696–2767.
- Gustafsson, A.** and **E. Kapon** (1998). Cathodoluminescence in the scanning electron microscope: application to low-dimensional semiconductor structures. *Scanning Microscopy*, **12**(2), 285–299.
- Guzzinati, G., T. Altantzis, M. Batuk, A. De Backer, G. Lumbeeck, V. Samaee, D. Batuk, H. Idrissi, J. Hadermann, S. Van Aert, et al.** (2018). Recent advances in transmission electron microscopy for materials science at the emat lab of the university of antwerp. *Materials*, **11**(8), 1304.
- Haass, S. G., M. Diethelm, M. Werner, B. Bissig, Y. E. Romanyuk, and A. N. Tiwari** (2015). 11.2% efficient solution processed kesterite solar cell with a low voltadeficit. *Advanced Energy Materials*, **5**(18), 1500712.
- Hagfeldt, A., G. Boschloo, L. Sun, L. Kloo, and H. Pettersson** (2010). Dye-sensitized solar cells. *Chemical Reviews*, **110**(11), 6595–6663.
- Hanaor, D. A. and C. C. Sorrell** (2011). Review of the anatase to rutile phase transformation. *Journal of Materials science*, **46**(4), 855–874.
- He, Y., Z. Zhang, and Y. Zhao** (2008). Optical and photocatalytic properties of oblique angle deposited TiO₂ nanorod array. *Journal of Vacuum Science & Technology B: Microelectronics and Nanometer Structures Processing, Measurement, and Phenomena*, **26**(4), 1350–1358.
- Heering, P. and D. Höttecke**, Historical-gative approaches in science teaching. In *International handbook of research in history, philosophy and science teaching*. Springer, 2014, 1473–1502.
- Hendry, E., M. Koe, B. O’regan, and M. Bonn** (2006). Local field effects on electron transport in nanostructured TiO₂ revealed by terahertz spectroscopy. *Nano letters*, **6**(4), 755–759.
- Hernández-Rodríguez, E., V. Rejón, R. Mis-Fernández, and J. Peña** (2016). Application of sputtered TiO₂ thin films as HRT buffer layer for high efficiency CdS/CdTe solar cells. *Solar Energy*, **132**, 64–72.

- Himmrich, M.** and **H. Haeseler** (1991). Far infrared studies on stannite and wurtzstannite type compounds. *Spectrochimica Acta Part A: Molecular Spectroscopy*, **47**(7), 933–942.
- Howell, J.** and **R. Sutton** (1998). Ultraviolet and absorption light spectrometry. *Analytical Chemistry*, **70**(12), 107–118.
- Hussein, H.** and **A. Yazdani** (2019). Spin-coated $\text{Cu}_2\text{CrSnS}_4$ thin film: A potential candidate for thin film solar cells. *Materials Science in Semiconductor Processing*, **91**, 58–65.
- İpeksaç, T., F. Kaya,** and **C. Kaya** (2013). Hydrothermal synthesis of Zinc oxide (ZnO) nanotubes and its electrophoretic deposition on nickel filter. *Materials Letters*, **100**, 11–14.
- Ito, K.** and **T. Nakazawa** (1988). Electrical and optical properties of stannite type quaternary semiconductor thin films. *Japanese Journal of Applied Physics*, **27**(11R), 2094.
- Janotti, A., J. Varley, P. Rinke, N. Umezawa, G. Kresse,** and **C. G. Van de Walle** (2010). Hybrid functional studies of the oxygen vacancy in TiO_2 . *Physical Review B*, **81**(8), 085212.
- Jarkov, A., S. Bereznev, K. Laes, O. Volobujeva, R. Traksmaa, A. Öpik,** and **E. Mellikov** (2011). Conductive polymer PEDOT:PSS back contact for CdTe solar cell. *Thin Solid Films*, **519**(21), 7449–7452.
- Jhuma, F. A., M. Z. Shaily,** and **M. J. Rashid** (2019). Towards high-efficiency CZTS solar cell through buffer layer optimization. *Materials for Renewable and Sustainable Energy*, **8**(1), 6.
- Ji, F., R. Zhou, H. Niu, L. Wan, H. Guo, X. Mao, W. Gan,** and **J. Xu** (2016). Oriented rutile TiO_2 nanorod arrays for efficient quantum dot-sensitized solar cells with extremely high open-circuit voltage. *Ceramics International*, **42**(10), 12194–12201.
- Jun-Feng, H., X. Liu, C. Li-Mei, J. Hamon,** and **M. Besland** (2015). Investigation of oxide layer on CdTe film surface and its effect on the device performance. *Materials Science in Semiconductor Processing*, **40**, 402–406.

- Karaagac, H., M. Parlak, L. Aygun, M. Ghaffari, N. Biyikli, and A. Okyay** (2013). A baseball-bat-like CdTe/TiO₂ nanorods-based heterojunction core-shell solar cell. *Scripta Materialia*, **69**(4), 323–326.
- Katagiri, H., N. Ishigaki, T. Ishida, and K. Saito** (2001). Characterization of Cu₂ZnSnS₄ thin films prepared by vapor phase sulfurization. *Japanese Journal of Applied Physics*, **40**(2R), 500.
- Katagiri, H., K. Jimbo, S. Yamada, T. Kamimura, W. S. Maw, T. Fukano, T. Ito, and T. Motohiro** (2008). Enhanced conversion efficiencies of Cu₂ZnSnS₄ based thin film solar cells by using preferential etching technique. *Applied physics express*, **1**(4), 041201.
- Kaur, K., N. Kumar, and M. Kumar** (2017). Strategic review of interface carrier recombination in earth abundant Cu-Zn-Sn-S-Se solar cells: current challenges and future prospects. *Journal of Materials Chemistry A*, **5**(7), 3069–3090.
- Kayes, B. M., H. A. Atwater, and N. S. Lewis** (2005). Comparison of the device physics principles of planar and radial p-n junction nanorod solar cells. *Journal of applied physics*, **97**(11), 114302.
- Khrypunov, G., S. Bereznev, A. Meriuts, G. Kopach, N. Kovtun, and N. Deyneko** (2010). Development Organic Back Contact for Thin-Film CdS/CdTe Solar Cell. *Physics and Chemistry of Solid State*, **11**(1), 248–251.
- Khrypunov, M., D. Kudii, N. Kovtun, M. Kharchenko, and I. Khrypunova** (2019). Development of back and front contacts for cdte layer in tandem flexible photoelectric converters on basis of CdTe/CuInSe₂. *International Journal of Photoenergy*, **2019**.
- Khurram, A., M. Imran, N. A. Khan, and M. N. Mehmood** (2017). ZnSe/ITO thin films: candidate for CdTe solar cell window layer. *Journal of Semiconductors*, **38**(9), 093001.
- Kim, H.-S., C.-R. Lee, J.-H. Im, K.-B. Lee, T. Moehl, A. Marchioro, S.-J. Moon, R. Humphry-Baker, J.-H. Yum, J. E. Moser, et al.** (2012). Lead iodide perovskite sensitized all-solid-state submicron thin film mesoscopic solar cell with efficiency exceeding 9%. *Scientific reports*, **2**(1), 1–7.

- Kim, H.-S. and N.-G. Park** (2014). Parameters affecting, I–V hysteresis of $\text{CH}_3\text{NH}_3\text{PbI}_3$ perovskite solar cells: effects of perovskite crystal size and mesoporous TiO_2 layer. *The journal of physical chemistry letters*, **5**(17), 2927–2934.
- Kim, J., H. Hiroi, T. K. Todorov, O. Gunawan, M. Kuwahara, T. Gokmen, D. Nair, M. Hopstaken, B. Shin, Y. S. Lee, et al.** (2014). High efficiency $\text{Cu}_2\text{ZnSn}(\text{S},\text{Se})_4$ solar cells by applying a double $\text{In}_2\text{S}_3/\text{CdS}$ emitter. *Advanced Materials*, **26**(44), 7427–7431.
- Köhnen, E., M. Jošt, A. B. Morales-Vilches, P. Tockhorn, A. Al-Ashouri, B. Macco, L. Kegelmann, L. Korte, B. Rech, R. Schlattmann, et al.** (2019). Highly efficient monolithic perovskite silicon tandem solar cells: analyzing the influence of current mismatch on device performance. *Sustainable Energy & Fuels*, **3**(8), 1995–2005.
- Kojima, A., K. Teshima, Y. Shirai, and T. Miyasaka** (2009). Organometal halide perovskites as visible-light sensitizers for photovoltaic cells. *Journal of the American Chemical Society*, **131**(17), 6050–6051.
- Korin, E., N. Froumin, and S. Cohen** (2017). Surface analysis of nanocomplexes by X-ray photoelectron spectroscopy (XPS). *Acs Biomaterials Science & Engineering*, **3**(6), 882–889.
- Kumar, A., K.-t. Li, A. R. Madaria, and C. Zhou** (2011). Sensitization of hydrothermally grown single crystalline TiO_2 nanowire array with cdes nanocrystals for photovoltaic applications. *Nano Research*, **4**(12), 1181–1190.
- Kumar, M., A. Dubey, N. Adhikari, S. Venkatesan, and Q. Qiao** (2015). Strategic review of secondary phases, defects and defect-complexes in kesterite CZTS–Se solar cells. *Energy & Environmental Science*, **8**(11), 3134–3159.
- Kurokawa, M., K. Tanaka, K. Moriya, and H. Uchiki** (2012). Fabrication of three-dimensional-structure solar cell with $\text{Cu}_2\text{ZnSnS}_4$. *Japanese Journal of Applied Physics*, **51**(10S), 10NC33.
- Lattante, S.** (2014). Electron and hole transport layers: their use in inverted bulk heterojunction polymer solar cells. *Electronics*, **3**(1), 132–164.

- Lee, Y. S., T. Gershon, O. Gunawan, T. K. Todorov, T. Gokmen, Y. Virgus, and S. Guha** (2015). $\text{Cu}_2\text{ZnSnSe}_4$ thin-film solar cells by thermal co-evaporation with 11.6% efficiency and improved minority carrier diffusion length. *Advanced Energy Materials*, **5**(7), 1401372.
- Lei, Y., L.-D. Zhang, G.-W. Meng, G.-H. Li, X. Y. Zhang, C. Liang, W. Chen, and S. Wang** (2001). Preparation and photoluminescence of highly ordered TiO_2 nanowire arrays. *Applied physics letters*, **78**(8), 1125–1127.
- Leung, S.-F., Q. Zhang, F. Xiu, D. Yu, J. C. Ho, D. Li, and Z. Fan** (2014). Light management with nanostructures for optoelectronic devices. *The journal of physical chemistry letters*, **5**(8), 1479–1495.
- Li, G., X. Zhao, and J. Ji** (2016). Conceptual development of a novel photovoltaic-thermoelectric system and preliminary economic analysis. *Energy conversion and management*, **126**, 935–943.
- Li, L., S. Pan, X. Dou, Y. Zhu, X. Huang, Y. Yang, G. Li, and L. Zhang** (2007). Direct electrodeposition of zno nanotube arrays in anodic alumina membranes. *The Journal of Physical Chemistry C*, **111**(20), 7288–7291.
- Li, L., J. Yan, T. Wang, Z.-J. Zhao, J. Zhang, J. Gong, and N. Guan** (2015). Sub-10 nm rutile titanium dioxide nanoparticles for efficient visible-light-driven photocatalytic hydrogen production. *Nature communications*, **6**(1), 1–10.
- Li, N., X. Zhang, W. Zhou, Z. Liu, G. Xie, Y. Wang, and Y. Du** (2014a). High quality sulfur-doped titanium dioxide nanocatalysts with visible light photocatalytic activity from non-hydrolytic thermolysis synthesis. *Inorganic Chemistry Frontiers*, **1**(7), 521–525.
- Li, Y., S. Witharana, H. Cao, M. Lasfargues, Y. Huang, and Y. Ding** (2014b). Wide spectrum solar energy harvesting through an integrated photovoltaic and thermoelectric system. *Particuology*, **15**, 39–44.
- Li, Z., J. Shi, Q. Liu, Y. Chen, Z. Sun, Z. Yang, and S. Huang** (2011). Large-scale growth of $\text{Cu}_2\text{ZnSnSe}_4$ and $\text{Cu}_2\text{ZnSnSe}_4/\text{Cu}_2\text{ZnSnS}_4$ core/shell nanowires. *Nanotechnology*, **22**(26), 265615.

- Liu, B.** and **E. S. Aydil** (2009). Growth of oriented single-crystalline rutile TiO₂ nanorods on transparent conducting substrates for dye-sensitized solar cells. *Journal of the American Chemical Society*, **131**(11), 3985–3990.
- Liu, B., R. Luo, Q. Liang, Y. Zheng, B. Li, J. Zhang, W. Li, L. Wu,** and **L. Feng** (2015). Preparation of novel CdS/ZnS composite window layer for CdTe thin film solar cell. *Journal of Materials Science: Materials in Electronics*, **26**(12), 9985–9990.
- Liu, R.** (2014). Hybrid organic/inorganic nanocomposites for photovoltaic cells. *Materials*, **7**(4), 2747–2771.
- Liu, X., Y. Feng, H. Cui, F. Liu, X. Hao, G. Conibeer, D. B. Mitzi,** and **M. Green** (2016). The current status and future prospects of kesterite solar cells: a brief review. *Progress in Photovoltaics: Research and Applications*, **24**(6), 879–898.
- Lü, X., F. Huang, X. Mou, Y. Wang,** and **F. Xu** (2010). A general preparation strategy for hybrid TiO₂ hierarchical spheres and their enhanced solar energy utilization efficiency. *Advanced Materials*, **22**(33), 3719–3722.
- Luo, L., G. Lv, B. Li, X. Hu, L. Jin, J. Wang,** and **Y. Tang** (2010). Formation of aligned ZnO nanotube arrays by chemical etching and coupling with CdSe for photovoltaic application. *Thin Solid Films*, **518**(18), 5146–5152.
- Ma, L., Z. Wei, F. Zhang,** and **X. Wu** (2015). Synthesis and characterization of high-ordered CdTe nanorods. *Superlattices and Microstructures*, **88**, 536–540.
- Maes, J., R. Dierick, B. Capon, C. Detavernier,** and **Z. Hens** (2016). Se-containing inks for the formation of CuInSe₂ films without gas-phase selenization. *Solar Energy Materials and Solar Cells*, **145**, 126–133.
- Mahato, S.** (2017). Composition analysis of two different PEDOT:PSS commercial products used as an interface layer in Au/n-Si Schottky diode. *RSC advances*, **7**(74), 47125–47131.
- Major, J., L. Phillips, M. Al Turkestani, L. Bowen, T. Whittles, V. Dhanak,** and **K. Durose** (2017). P3HT as a pinhole blocking back contact for CdTe thin film solar cells. *Solar Energy Materials and Solar Cells*, **172**, 1–10.

- Mali, S. S., C. A. Betty, P. N. Bhosale, R. S. Devan, Y.-R. Ma, S. S. Kolekar, and P. S. Patil** (2012). Hydrothermal synthesis of rutile TiO₂ nanoflowers using Brønsted Acidic Ionic Liquid [BAIL]: Synthesis, characterization and growth mechanism. *CrystEngComm*, **14**(6), 1920–1924.
- Mali, S. S., C. S. Shim, H. Kim, and C. K. Hong** (2016). Single step synthesized 1D TiO₂ vertically aligned nanorod arrays for CdS sensitized quantum dot sensitized solar cells. *Ceramics International*, **42**(1), 1973–1981.
- Manthina, V. and A. G. Agrios** (2016). Single-pot zno nanostructure synthesis by chemical bath deposition and their applications. *Nano-Structures & Nano-Objects*, **7**, 1–11.
- Marschall, R. and L. Wang** (2014). Non-metal doping of transition metal oxides for visible-light photocatalysis. *Catalysis Today*, **225**, 111–135.
- Martinson, A. B., J. W. Elam, J. T. Hupp, and M. J. Pellin** (2007). ZnO nanotube based dye-sensitized solar cells. *Nano letters*, **7**(8), 2183–2187.
- Matos, J., A. Borodzinski, A. M. Zychora, P. Kedzierzawski, B. Mierzwa, K. Juchniewicz, M. Mazurkiewicz, and J. C. Hernández-Garrido** (2015). Direct formic acid fuel cells on Pd catalysts supported on hybrid TiO₂-C materials. *Applied Catalysis B: Environmental*, **163**, 167–178.
- Mattox, D. M.**, *Handbook of physical vapor deposition (PVD) processing*, William Andrew, 2010.
- McCandless, B. E. and R. W. Birkmire**, Influence of window and absorber layer processing on device operation in superstrate thin film CdTe solar cells. *In Conference Record of the Twenty-Eighth IEEE Photovoltaic Specialists Conference-2000 (Cat. No. 00CH37036)*. IEEE, 2000.
- McCandless, B. E. and J. R. Sites** (2011). Cadmium telluride solar cells. *Handbook of Photovoltaic Science and Engineering*, 600–641.
- Milanova, M. and V. Khvostikov** (2000). Growth and doping of GaAs and AlGaAs layers by low-temperature liquid-phase epitaxy. *Journal of Crystal Growth*, **219**, 193–198.

- Minnaert, B. and P. Veelaert** (2014). A proposal for typical artificial light sources for the characterization of indoor photovoltaic applications. *Energies*, **7**(3), 1500–1516.
- Mitchell, K., A. L. Fahrenbruch, and R. H. Bube** (1977). Photovoltaic determination of optical-absorption coefficient in cdte. *Journal of Applied Physics*, **48**(2), 829–830.
- Mitzi, D. B., O. Gunawan, T. K. Todorov, K. Wang, and S. Guha** (2011). The path towards a high-performance solution-processed kesterite solar cell. *Solar Energy Materials and Solar Cells*, **95**(6), 1421–1436.
- Murakoshi, K., R. Kogure, Y. Wada, and S. Yanagida** (1998). Fabrication of solid-state dye-sensitized TiO₂ solar cells combined with polypyrrole. *Solar Energy Materials and Solar Cells*, **55**(1-2), 113–125.
- Muska, K., M. Kauk-Kuusik, M. Grossberg, M. Altosaar, M. Pilvet, T. Varema, K. Timmo, O. Volobujeva, and A. Mere** (2013). Impact of Cu₂ZnSn(Se_xS_{1-x})₄ (x= 0.3) compositional ratios on the monograin powder properties and solar cells. *Thin Solid Films*, **535**, 35–38.
- Mutalikdesai, A. and S. K. Ramasesha** (2017). Solution process for fabrication of thin film CdS/CdTe photovoltaic cell for building integration. *Thin Solid Films*, **632**, 73–78.
- Niu, Y., M. Xing, J. Zhang, and B. Tian** (2013). Visible light activated sulfur and iron co-doped TiO₂ photocatalyst for the photocatalytic degradation of phenol. *Catalysis Today*, **201**, 159–166.
- Nomoto, J., H. Makino, T. Nakajima, T. Tsuchiya, and T. Yamamoto** (2019). Improvement of the properties of direct-current magnetron-sputtered Al-doped ZnO polycrystalline films containing retained Ar atoms using 10-nm-thick buffer layers. *ACS omega*, **4**(11), 14526–14536.
- Ohno, T., M. Akiyoshi, T. Umebayashi, K. Asai, T. Mitsui, and M. Matsumura** (2004). Preparation of S-doped TiO₂ photocatalysts and their photocatalytic activities under visible light. *Applied Catalysis A: General*, **265**(1), 115–121.

- Okuyama, K., D. Huang, J. H. Seinfeld, N. Tani, and Y. Kousaka** (1991). Aerosol formation by rapid nucleation during the preparation of SiO₂ thin films from SiCl₄ and O₂ gases by CVD process. *Chemical Engineering Science*, **46**(7), 1545–1560.
- Pechkova, E. and C. Nicolini** (2002). From art to science in protein crystallization by means of thin-film nanotechnology. *Nanotechnology*, **13**(4), 460.
- Pellegrin, Y., L. Le Pleux, E. Blart, A. Renaud, B. Chavillon, N. Szuwarski, M. Boujtita, L. Cario, S. Jobic, D. Jacquemin, et al.** (2011). Ruthenium polypyridine complexes as sensitizers in NiO based p-type dye-sensitized solar cells: Effects of the anchoring groups. *Journal of Photochemistry and Photobiology A: Chemistry*, **219**(2-3), 235–242.
- Periyat, P. and S. Ullattil** (2015). Sol–gel derived nanocrystalline ZnO photoanode film for dye sensitized solar cells. *Materials Science in Semiconductor Processing*, **31**, 139–146.
- Polman, A., M. Knight, E. C. Garnett, B. Ehrler, and W. C. Sinke** (2016). Photovoltaic materials: Present efficiencies and future challenges. *Science*, **352**(6283), aad4424.
- Potlog, T., N. Spalatu, V. Fedorov, N. Maticiuc, C. Antoniu, V. Botnariuc, J. Hiie, T. Raadik, and V. Valdna** (2011). The performance of thin film solar cells employing photovoltaic ZnSe/CdTe, CdS/CdTe and ZnTe/CdTe heterojunctions. *In 2011 37th IEEE Photovoltaic Specialists Conference*. IEEE, 2011.
- Pradhan, S. K., P.J. Reucroft, F. Yang, and A. Dozier** (2003). Growth of TiO₂ nanorods by metalorganic chemical vapor deposition. *Journal of Crystal Growth*, **256**(1-2), 83–88.
- Promros, N. and B. Paosawatyanong**, Silver thin films deposited by compact magnetron sputtering system. *In Advanced Materials Research*, volume 93. Trans Tech Publ, 2010.
- Qin, D.-D., Q.-H. Wang, J. Chen, C.-H. He, Y. Li, C.-H. Wang, J.-J. Quan, C.-L. Tao, and X.-Q. Lu** (2017). Phosphorus-doped TiO₂ nanotube arrays for

- visible-light-driven photoelectrochemical water oxidation. *Sustainable Energy & Fuels*, **1**(2), 248–253.
- Ramasamy, K., M. A. Malik, and P. O'Brien** (2012). Routes to copper zinc tin sulfide $\text{Cu}_2\text{ZnSnS}_4$ a potential material for solar cells. *Chemical communications*, **48**(46), 5703–5714.
- Razykov, T., N. Amin, M. Alghoul, B. Ergashev, C. Ferekides, Y. Goswami, M. Hakkulov, K. Kouchkarov, K. Sopian, M. Sulaiman, et al.** (2012). Effect of the composition on physical properties of CdTe absorber layer fabricated by chemical molecular beam deposition for use in thin film solar cells. *Journal of Applied Physics*, **112**(2), 023517.
- Repins, I., C. Beall, N. Vora, C. DeHart, D. Kuciauskas, P. Dippo, B. To, J. Mann, W.-C. Hsu, A. Goodrich, et al.** (2012). Co-evaporated $\text{Cu}_2\text{ZnSnSe}_4$ films and devices. *Solar Energy Materials and Solar Cells*, **101**, 154–159.
- Riordan, C. and R. Hulstron** (1990). What is an air mass 1.5 spectrum? (solar cell performance calculations). In *IEEE Conference on Photovoltaic Specialists*. IEEE, 1990.
- Robel, I., V. Subramanian, M. Kuno, and P. V. Kamat** (2006). Quantum dot solar cells. harvesting light energy with CdSe nanocrystals molecularly linked to mesoscopic TiO_2 films. *Journal of the American Chemical Society*, **128**(7), 2385–2393.
- Romeo, N., A. Bosio, D. Menossi, A. Romeo, and M. Aramini** (2014). Last progress in CdTe/CdS thin film solar cell fabrication process. *Energy Procedia*, **57**, 65–72.
- Rosnagel, S.** (2003). Thin film deposition with physical vapor deposition and related technologies. *Journal of Vacuum Science & Technology A: Vacuum, Surfaces, and Films*, **21**(5), S74–S87.
- Roy, P., D. Kim, K. Lee, E. Spiecker, and P. Schmuki** (2010). TiO_2 nanotubes and their application in dye-sensitized solar cells. *Nanoscale*, **2**(1), 45–59.
- Sadegh-cheri, M.** (2019). Design, fabrication, and optical characterization of a low- cost and open-source spin coater. *Journal of Chemical Education*, **96**(6), 1268–1272.

- Samsudin, E. M. and S. B. Abd Hamid** (2017). Effect of band gap engineering in anionic-doped TiO₂ photocatalyst. *Applied Surface Science*, **391**, 326–336.
- Schlur, L., J. R. Calado, and D. Spitzer** (2018). Synthesis of zinc oxide nanorods or nanotubes on one side of a microcantilever. *Royal Society open science*, **5**(8), 180510.
- Senthil, K., D. Mangalaraj, and S. K. Narayandass** (2001). Structural and optical properties of CdS thin films. *Applied surface science*, **169**, 476–479.
- Sequeda, F.** (1986). Thin film deposition techniques in microelectronics. *JOM*, **38**(2), 55–65.
- Shafarman, W. N., S. Siebentritt, and L. Stolt** (2011). Cu(InGa)Se₂ Solar Cells. *Handbook of photovoltaic science and engineering*, **2**, 546–599.
- Shaikh, J. S., N. S. Shaikh, S. S. Mali, J. V. Patil, K. K. Pawar, P. Kan- janaboos, C. K. Hong, J. H. Kim, and P. S. Patil** (2018). Nanoarchitectures in dye-sensitized solar cells: metal oxides, oxide perovskites and carbon-based materials. *Nanoscale*, **10**(11), 4987–5034.
- Shavel, A., D. Cadavid, M. Ibanez, A. Carrete, and A. Cabot** (2012). Continuous production of Cu₂ZnSnS₄ nanocrystals in a flow reactor. *Journal of the American Chemical Society*, **134**(3), 1438–1441.
- Shenouda, A. Y. and M. El Sayed** (2015). Electrodeposition, characterization and photo electrochemical properties of CdSe and CdTe. *Ain Shams Engineering Journal*, **6**(1), 341–346.
- Shin, E., S. Jin, J. Kim, S.-J. Chang, B.-H. Jun, K.-W. Park, and J. Hong** (2016). Preparation of K-doped TiO₂ nanostructures by wet corrosion and their sunlight driven photocatalytic performance. *Applied Surface Science*, **379**, 33–38.
- Singh, E., K. S. Kim, G. Y. Yeom, and H. S. Nalwa** (2017). Atomically thin-layered molybdenum disulfide (MoS₂) for bulk-heterojunction solar cells. *ACS applied materials & interfaces*, **9**(4), 3223–3245.
- Smestad, G. P., S. Spiekermann, J. Kowalik, C. D. Grant, A. M. Schwartzberg, J. Zhang, L. M. Tolbert, and E. Moons** (2003). A technique to

compare polythiophene solid-state dye sensitized TiO₂ solar cells to liquid junction devices. *Solar Energy Materials and Solar Cells*, **76**(1), 85–105.

Son, D.-H., S.-H. Kim, S.-Y. Kim, Y.-I. Kim, J.-H. Sim, S.-N. Park, D.-H.

Jeon, D.-K. Hwang, S.-J. Sung, J.-K. Kang, et al. (2019). Effect of solid-H₂S gas reactions on CZTSSe thin film growth and photovoltaic properties of a 12.62% efficiency device. *Journal of Materials Chemistry A*, **7**(44), 25279–25289.

Soomro, M., I. Hussain, N. Bano, J. Lu, L. Hultman, O. Nur, and M. Willander (2012). Growth, structural and optical characterization of ZnO nanotubes on disposable-flexible paper substrates by low-temperature chemical method. *Journal of nanotechnology*, **2012**.

Sripan, C., R. Ganesan, E. Vinod, and A. K. Viswanath (2016). The effect of sulfur on the phase formation of Cu₂ZnSnS₄ solar cell material. *Materials Letters*, **180**, 295–297.

Sripan, C., V. E. Madhavan, R. Ganesan, and A. K. Viswanath (2017a). Influence of annealing temperature on the properties of non-stoichiometric Cu_{1.66}Zn_{1.25}GeSe₄ thin films. *Surfaces and Interfaces*, **7**, 134–138.

Sripan, C., V. E. Madhavan, A. K. Viswanath, and R. Ganesan (2017b). Sulfurization and annealing effects on thermally evaporated CZTS films. *Materials Letters*, **189**, 110–113.

Staffell, I., D. Scamman, A. V. Abad, P. Balcombe, P. E. Dodds, P. Ekins,

N. Shah, and K. R. Ward (2019). The role of hydrogen and fuel cells in the global energy system. *Energy & Environmental Science*, **12**(2), 463–491.

Star, A., J.-C. P. Gabriel, K. Bradley, and G. Grüner (2003). Electronic detection of specific protein binding using nanotube FET devices. *Nano letters*, **3**(4), 459–463.

Stark, C., J. Pless, J. Logan, E. Zhou, and D. J. Arent (2015). Renewable electricity: Insights for the coming decade. Technical report, National Renewable Energy Lab.(NREL), Golden, CO (United States).

- Stolarczyk, J. K., S. Bhattacharyya, L. Polavarapu, and J. Feldmann** (2018). Challenges and prospects in solar water splitting and CO₂ reduction with inorganic and hybrid nanostructures. *ACS Catalysis*, **8**(4), 3602–3635.
- Strano, V., R. G. Urso, M. Scuderi, K. O. Iwu, F. Simone, E. Ciliberto, C. Spinella, and S. Mirabella** (2014). Double role of HMTA in ZnO nanorods grown by chemical bath deposition. *The Journal of Physical Chemistry C*, **118**(48), 28189–28195.
- Su, Z., J. M. R. Tan, X. Li, X. Zeng, S. K. Batabyal, and L. H. Wong** (2015). Cation substitution of solution-processed Cu₂ZnSnS₄ thin film solar cell with over 9% efficiency. *Advanced Energy Materials*, **5**(19), 1500682.
- Sun, Y., D. J. Riley, and M. N. Ashfold** (2006). Mechanism of ZnO nanotube growth by hydrothermal methods on ZnO film-coated Si substrates. *The Journal of Physical Chemistry B*, **110**(31), 15186–15192.
- Sutiono, H., A. M. Tripathi, H.-M. Chen, C.-H. Chen, W.-N. Su, L.-Y. Chen, H. Dai, and B.-J. Hwang** (2016). Facile synthesis of [101]-oriented rutile TiO₂ nanorod array on FTO substrate with a tunable anatase–rutile heterojunction for efficient solar water splitting. *ACS Sustainable Chemistry & Engineering*, **4**(11), 5963–5971.
- Szkoda, M., K. Siuzdak, A. Lisowska-Oleksiak, J. Karczewski, and J. Ryl** (2015). Facile preparation of extremely photoactive boron-doped TiO₂ nanotubes arrays. *Electrochemistry Communications*, **60**, 212–215.
- Tajima, S., M. Umehara, M. Hasegawa, T. Mise, and T. Itoh** (2017). Cu₂ZnSnS₄ photovoltaic cell with improved efficiency fabricated by high-temperature annealing after CdS buffer-layer deposition. *Progress in Photovoltaics: Research and Applications*, **25**(1), 14–22.
- Taya, S. A., T. M. El-Agez, H. S. El-Ghamri, and M. S. Abdel-Latif** (2013). Dye-sensitized solar cells using fresh and dried natural dyes. *International Journal of Materials Science and Applications*, **2**(2), 37–42.
- Tobias, I., C. del Canizo, and J. Alonso** (2011). Crystalline silicon solar cells and modules. *Handbook of Photovoltaic Science and Engineering, John Wiley & Sons, Ltd*, 265–313.

- Todorov, T. and D. B. Mitzi** (2010). Direct liquid coating of chalcopyrite light- absorbing layers for photovoltaic devices. *European Journal of Inorganic Chemistry*, **2010**(1), 17–28.
- Todorov, T. K., K. B. Reuter, and D. B. Mitzi** (2010). High-efficiency solar cell with earth-abundant liquid-processed absorber. *Advanced materials*, **22**(20), E156–E159.
- Tong, Y., Y. Liu, C. Shao, Y. Liu, C. Xu, J. Zhang, Y. Lu, D. Shen, and X. Fan** (2006). Growth and optical properties of faceted hexagonal ZnO nanotubes. *The Journal of Physical Chemistry B*, **110**(30), 14714–14718.
- Tosun, B. S., B. D. Chernomordik, A. A. Gunawan, B. Williams, K. A. Mkhoyan, L. F. Francis, and E. S. Aydil** (2013). Cu₂ZnSnS₄ nanocrystal dispersions in polar liquids. *Chemical Communications*, **49**(34), 3549–3551.
- Tumbul, A., F. Aslan, A. Göktaş, and I. Mutlu** (2019). All solution processed superstrate type Cu₂ZnSnS₄ (CZTS) thin film solar cell: effect of absorber layer thickness. *Journal of Alloys and Compounds*, **781**, 280–288.
- Turkten, N., Z. Cinar, A. Tomruk, and M. Bekbolet** (2019). Copper-doped TiO₂ photocatalysts: application to drinking water by humic matter degradation. *Environmental Science and Pollution Research*, **26**(36), 36096–36106.
- Varadharajaperumal, S., D. Alagarasan, R. Ganesan, M. Satyanarayan, and G. Hegde** (2020). Controlled growth of 1D-ZnO nanotubes using one-step hot plate technique for CZTS heterojunction solar cells. *Materials Science in Semiconductor Processing*, **106**, 104763.
- Varadharajaperumal, S., M. S. Ilango, G. Hegde, and M. Satyanarayan** (2019). Effect of CuPc and PEDOT:PSS as hole transport layers in planar heterojunction CdS/CdTe solar cell. *Materials Research Express*, **6**(9), 095009.
- Varadharajaperumal, S., C. Sripan, R. Ganesan, G. Hegde, and M. Satyanarayana** (2017). Morphology controlled n-type TiO₂ and stoichiometry adjusted p-type Cu₂ZnSnS₄ thin films for photovoltaic applications. *Crystal Growth & Design*, **17**(10), 5154–5162.

- Vasireddi, R., B. Javvaji, H. Vardhan, D. Mahapatra, and G. Hegde** (2017). Growth of zinc oxide nanorod structures: pressure controlled hydrothermal process and growth mechanism. *Journal of Materials Science*, **52**(4), 2007–2020.
- Vayssieres, L., K. Keis, A. Hagfeldt, and S.-E. Lindquist** (2001). Three dimensional array of highly oriented crystalline ZnO microtubes. *Chemistry of Materials*, **13**(12), 4395–4398.
- Wang, L., X. Huang, J. Xia, D. Zhu, X. Li, and X. Meng** (2016a). Three dimensional ZnO nanotube arrays and their optical tuning through formation of type-II heterostructures. *CrystEngComm*, **18**(14), 2517–2523.
- Wang, Q., J.-E. Moser, and M. Grätzel** (2005). Electrochemical impedance spectroscopic analysis of dye-sensitized solar cells. *The Journal of Physical Chemistry B*, **109**(31), 14945–14953.
- Wang, W., N. R. Paudel, Y. Yan, F. Duarte, and M. Mount** (2016b). PEDOT:PSS as back contact for CdTe solar cells and the effect of PEDOT:PSS conductivity on device performance. *Journal of Materials Science: Materials in Electronics*, **27**(2), 1057–1061.
- Wang, W., M. T. Winkler, O. Gunawan, T. Gokmen, T. K. Todorov, Y. Zhu, and D. B. Mitzi** (2014). Device characteristics of CZTSSe thin-film solar cells with 12.6% efficiency. *Advanced Energy Materials*, **4**(7), 1301465.
- Wang, Y., C. Li, X. Yin, H. Wang, and H. Gong** (2013). Cu₂ZnSnS₄ (CZTS) application in TiO₂ solar cell as dye. *ECS Journal of Solid State Science and Technology*, **2**(7), Q95.
- Wang, Z. and G. P. Demopoulos** (2015). Growth of Cu₂ZnSnS₄ nanocrystallites on TiO₂ nanorod arrays as novel extremely thin absorber solar cell structure via the successive-ion-layer-adsorption-reaction method. *ACS Applied Materials & Interfaces*, **7**(41), 22888–22897.
- Wang, Z. L. and W. Wu** (2012). Nanotechnology-enabled energy harvesting for self-powered micro-/nanosystems. *Angewandte Chemie International Edition*, **51**(47), 11700–11721.

- Wong, W.-Y. and C.-L. Ho** (2010). Organometallic photovoltaics: a new and versatile approach for harvesting solar energy using conjugated polymetallaynes. *Accounts of chemical research*, **43**(9), 1246–1256.
- Wu, G., T. Nishikawa, B. Ohtani, and A. Chen** (2007). Synthesis and characterization of carbon-doped TiO₂ nanostructures with enhanced visible light response. *Chemistry of Materials*, **19**(18), 4530–4537.
- Wu, W.-Q., H.-L. Feng, H.-Y. Chen, D.-B. Kuang, and C.-Y. Su** (2017). Recent advances in hierarchical three-dimensional titanium dioxide nanotree arrays for high-performance solar cells. *Journal of Materials Chemistry A*, **5**(25), 12699–12717.
- Xing, Y., Z. Xi, Z. Xue, X. Zhang, J. Song, R. Wang, J. Xu, Y. Song, S.-L. Zhang, and D. Yu** (2003). Optical properties of the ZnO nanotubes synthesized via vapor phase growth. *Applied Physics Letters*, **83**(9), 1689–1691.
- Xu, L., Q. Liao, J. Zhang, X. Ai, and D. Xu** (2007). Single-crystalline ZnO nanotube arrays on conductive glass substrates by selective dissolution of electrodeposited ZnO nanorods. *The Journal of Physical Chemistry C*, **111**(12), 4549–4552.
- Yan, C., J. Huang, K. Sun, S. Johnston, Y. Zhang, H. Sun, A. Pu, M. He, F. Liu, K. Eder, et al.** (2018a). Cu₂ZnSnS₄ solar cells with over 10% power conversion efficiency enabled by heterojunction heat treatment. *Nature Energy*, **3**(9), 764–772.
- Yan, R., L. Kang, Y. Sun, and J. Zhang** (2018b). Solution-processed Cu₂ZnSnS₄ thin film with mixed solvent and its application in superstrate structure solar cells. *RSC advances*, **8**(21), 11469–11477.
- Yang, G. and S.-J. Park** (2019). Conventional and microwave hydrothermal synthesis and application of functional materials: A review. *Materials*, **12**(7), 1177.
- Yang, W., H.-S. Duan, B. Bob, H. Zhou, B. Lei, C.-H. Chung, S.-H. Li, W. W. Hou, and Y. Yang** (2012). Novel solution processing of high-efficiency earth-abundant Cu₂ZnSn (S, Se)₄ solar cells. *Advanced Materials*, **24**(47), 6323–6329.

- Ye, S., C. Shen, H. Pang, J. Wang, and Y. Lu** (2011). CdTe/PEDOT:PSS hybrid microspheres: Facile fabrication and multiple-color pH-sensing. *Polymer*, **52**(12), 2542–2549.
- Yoshikawa, K., H. Kawasaki, W. Yoshida, T. Irie, K. Konishi, K. Nakano, T. Uto, D. Adachi, M. Kanematsu, H. Uzu, et al.** (2017). Silicon heterojunction solar cell with interdigitated back contacts for a photoconversion efficiency over 26%. *Nature energy*, **2**(5), 17032.
- Youssef, S., P. Combette, J. Podlecki, R. A. Asmar, and A. Foucaran** (2009). Structural and optical characterization of ZnO thin films deposited by reactive rf magnetron sputtering. *Crystal Growth and Design*, **9**(2), 1088–1094.
- Yun, S., Y. Qin, A. R. Uhl, N. Vlachopoulos, M. Yin, D. Li, X. Han, and A. Hagfeldt** (2018). New-generation integrated devices based on dye-sensitized and perovskite solar cells. *Energy & Environmental Science*, **11**(3), 476–526.
- Zhang, Q., Y. Li, E. A. Ackerman, M. Gajdardziska-Josifovska, and H. Li** (2011). Visible light responsive iodine-doped TiO₂ for photocatalytic reduction of CO₂ to fuels. *Applied Catalysis A: General*, **400**(1-2), 195–202.
- Zhang, W., Y. He, M. Zhang, Z. Yin, and Q. Chen** (2000). Raman scattering study on anatase TiO₂ nanocrystals. *Journal of Physics D: Applied Physics*, **33**(8), 912.
- Zhao, K., Z. Pan, and X. Zhong** (2016). Charge recombination control for high efficiency quantum dot sensitized solar cells. *The journal of physical chemistry letters*, **7**(3), 406–417.
- Zhou, Y.-L., W.-H. Zhou, M. Li, Y.-F. Du, and S.-X. Wu** (2011). Hierarchical Cu₂ZnSnS₄ particles for a low-cost solar cell: morphology control and growth mechanism. *The Journal of Physical Chemistry C*, **115**(40), 19632–19639.
- Zhu, F., D. Wu, Q. Li, H. Dong, J. Li, K. Jiang, and D. Xu** (2012). Hierarchical TiO₂ microspheres: synthesis, structural control and their applications in dye-sensitized solar cells. *Rsc Advances*, **2**(31), 11629–11637.
- Zhu, L., Q. Lu, L. Lv, Y. Wang, Y. Hu, Z. Deng, Z. Lou, Y. Hou, and F. Teng** (2017). Ligand-free rutile and anatase TiO₂ nanocrystals as electron

extraction layers for high performance inverted polymer solar cells. *RSC advances*, **7**(33), 20084–20092.

Zhu, M., G. Niu, and J. Tang (2019). Elemental Se: fundamentals and its optoelectronic applications. *Journal of Materials Chemistry C*, **7**(8), 2199–2206.

Zhu, M., C. Zhai, L. Qiu, C. Lu, A. S. Paton, Y. Du, and M. C. Goh (2015). New method to synthesize S-doped TiO₂ with stable and highly efficient photocatalytic performance under indoor sunlight irradiation. *ACS Sustainable Chemistry & Engineering*, **3**(12), 3123–3129.

Zweibel, K., H. Ullal, and R. Mitchell (1990). Polycrystalline thin film photovoltaics. In IEEE Conference on Photovoltaic Specialists. *IEEE*, 1990.

Publications based on the thesis

International Journals

1. **S. Varadharajaperumal**, C. Sripan, R. Ganesan, Gopalkrishna Hegde, M.N. Satyanarayan (2017), “Morphology controlled n-type TiO₂ and stoichiometry adjusted p-type Cu₂ZnSnS₄ thin films for photovoltaic applications”, *Cryst. Growth Des* 17(10), 5154-5162.
2. **S. Varadharajaperumal**, Murugaiya Sridar Ilango, Gopalkrishna Hegde, M.N. Satyanarayan (2019), “Effect of CuPc and PEDOT:PSS as hole transport layers in planar heterojunction CdS/CdTe solar cell”, *Materials Research Express* 6(9), 095009.
3. **S. Varadharajaperumal**, D. Alagarasan, R. Ganesan, Gopalkrishna Hegde, M.N. Satyanarayana (2020), “Controlled growth of 1D-ZnO nanotubes using one-step hot plate technique for CZTS heterojunction solar cell”, *Materials Science in Semiconductor Processing* 106, 104763.
4. **S. Varadharajaperumal**, D. Alagarasan, C. Sripan, R. Ganesan, M.N. Satyanarayan, Gopalkrishna Hegde, “Toxic-free surface level sulphur doped 1D Ti-Ox- Sy nanorods for superstrate heterojunction CZTS thin film solar cells”, (*Under review*).

International Conferences

1. **S. Varadharajaperumal**, B.L. Prahada, M.N. Satyanarayan, Gopalkrishna Hegde (2016). “Combined Structures of Rutile TiO₂ Nano rods with Microspheres on FTO Substrates for Solid State Dye-Sensitized Solar Cells”, Conference on Emerging Materials (CEMAT). (**Poster presentation**).

2. **S. Varadharajaperumal**, C. Sripan, Amit Kumar, R. Ganesan, Gopalkrishna Hegde, M.N. Satyanarayan (2017). “Fabrication and characterization of n-Si/p-CZTSe inorganic heterojunction thinfilm solar cells”, Materials, Structures & Systems (ISSS). (**Oral presentation**).
3. **S. Varadharajaperumal**, D. Alagarasan, M.L. Pradeep Kumar, R. Ganesan, Gopalkrishna Hegde, M.N. Satyanarayan (2019). “Cd free Sulphurated 1D-TiO₂ nanorods for heterojunction solar cells”, International conference on Recent Trends in Metallurgy, Materials Science and Manufacturing (IMME). (**Oral presentation**). (**Best Oral presentation award**).

Student Details

Name : S. Varadharajaperumal
Date of Birth : 31/07/1986
Address : 913/A, 2nd floor, 2nd main, 10th cross, Divanarapalaya,
Mathikere, Bengaluru - 560054.
Contact : 7204231900
Email : varadhu31@gmail.com & varadhu@iisc.ac.in
Qualification : • Doctor of Philosophy (**Ph.D.**) (2020) (**CGPA: 8.67/10**)
National Institute of Technology Karnataka (NITK)
Surathkal, Mangalore, Karnataka.
• **M.Tech.**, in Nanoelectronics (2008-2010) (**CGPA: 8.9/10**)
SASTRA University, Tamilnadu, India.
• **M.Sc.**, in Physics (2006-2008) (**Percentage: 83**)
AVVM Sri Pushpam College, Bharathidasan University, Tamilnadu, India.

Research Experience:

April 2018-Till date : Tecnology Manager, CeNSE, IISc., Bengaluru, India.
April 2013-March 2018 : Senior Facility Technologist, CeNSE, IISc., Bengaluru, India.
August 2011-March 201 : Facility Technologist, CeNSE, IISc., Bengaluru, India.
July 2010-July 2011 : Project Associate, Dept. of ECE, IISc., Bengaluru, India.

No. of Internataional Publications: 11